NUCLEAR SCISSION

Ulrich BROSA, Siegfried GROSSMANN and Andreas MÜLLER

Fachbereich Physik der Philipps-Universität Marburg, Renthof 6, W-3550 Marburg, Fed. Rep. Germany

NORTH-HOLLAND

PHYSICS REPORTS (Review Section of Physics Letters) 197, No. 4 (1990) 167–262. North-Holland

NUCLEAR SCISSION

Ulrich BROSA*, Siegfried GROSSMANN and Andreas MÜLLER

Fachbereich Physik der Philipps-Universität Marburg, Renthof 6, W-3550 Marburg, Fed. Rep. Germany

Editor: B. Mühlschlegel Received February 1990

Contents:

* Now at HLRZ, c/o KFA, Postfach 1913, W-5170 Jülich, FRG.

0 370-1573/90/$33.60

Abstract:
Two models of nuclear exit channel reactions are examined: random neck rupture and multichannel fission. The foundations of both models are explained, and the algorithms for their usage are given. Ample experimental evidence for the validity of these models is presented. Especially fruitful is their synthesis. We now understand the properties of the fragments, which are produced in low-energy fission, much better than we did four years ago.

1. Introduction

1.1. Scission versus fission

During the past 50 years progress in understanding nuclear fission was slow. Now we have one of those small jolts of which the last happened when the fission isomers were discovered [1.1, 1.2]. And yet, the new jolt brought not only more understanding but also drastic effects. It is expected to have an impact on applications.

Formerly fission was pictured as a sequence of equilibrium states: the ground or compound state, of course, was deemed to be in equilibrium. The same property was attributed to the nucleus at its saddle point. And even at the moment of most violent disintegration, equilibrium was invoked. However, nuclear fission is rather an *evolution by instabilities* (ch. 3). The word "scission" expresses violent motion somewhat better than "fission", and so we call this report "nuclear scission".

The second reason for taking "scission" instead of "fission" is to include low-energy deep-inelastic reactions [1.3]. When one speaks of fission, one mostly has nuclei in mind with mass numbers between $A_{cn} = 200$ and 260. However, some processes in the exit channels of deep-inelastic reactions resemble those of ordinary fission, and the additional insight is in fact valuable (ch. 5). Namely, scissioning nuclei as heavy as $A_{cn} = 476$ were studied. Very light, extremely asymmetric and hot scissioning nuclei were also produced in this way. All this yielded a tremendous extrapolation beyond the data that could be obtained from ordinary fission. When these data were analyzed, it turned out that discrepancies between almost-equilibrium theories and measurements, which had often been only 100% in nuclear fission [1.4], boomed to 1000% in deep-inelastic reactions [1.5]. This made sure that manicuring equilibrium models would not help.

But this too is not the main reason for the title. Actually "scission" is intended to denote the instant of rupture. In this report more than this instant will be discussed though not the complete process of fission. We shall leave out fission cross-sections, compound formation and say little about how the saddle is reached [1.6]. In other words, we shall concentrate on the *exit channel* and hence be concerned with *fragment properties* as yield, total kinetic energy, neutron multiplicity (chs. 5, 7 and 8, section 6.4) and, to a lesser degree, gamma emission (section 8.5).

1.2. Multichannel fission

One of the new discoveries is that there are *several* exit channels in spontaneous fission or low-energy induced fission (chs. 7 and 8). Leaving the compound state, the nucleus may choose between various paths to disintegration. These paths are related to but not the same as the *Bohr fission channels* [1.7] (section 7.5). The Bohr fission channels are rather metastable *states* over the barrier. The term "channel", however, suggests a *guided evolution*, and this is exactly what the new channels are for.

Instead of one fission barrier – maybe doubly humped – we now see that every nuclide has a system of them. Also at rupture, instead of one nuclear shape several of them can be distinguished. Since there

is, in most cases, only one way out of the compound state, fluctuations disregarded, the fission channels must fork. The new objects in multichannel fission are thus *bifurcation points* (sections 7.1 and 8.1).

One may find these channels by computing the potential energy as a function of the shape parameters. In this, quantum shell corrections and advanced searching techniques are indispensable (sections 9.1, 9.2).

Potential energy computations alone are not sufficient, as the connection to the exit channel observables is still missing. *Random neck rupture* provides the link (section 9.3).

1.3. Random neck rupture

The main item in random neck rupture is the *prescission shape*. It looks like two heads connected by a thick neck. *Neck rupture* means the neck snaps *when* the nucleus stretches beyond the prescission shape. *Random* neck rupture means it is not decided *where* the neck breaks (ch. 3).

Knowing random neck rupture, one may compute the most important exit channel observables provided the prescission shape is given (ch. 4, section 9.3). However, random neck rupture does not itself deliver the prescission shape. Fortunately, with the fission channel calculations we can find the desired shape (in general several of them), see ch. 9. Hence multichannel calculations and random neck rupture supplement each other.

The union of multichannel calculations and random neck rupture has solved, among others, two long-standing problems with the mass distribution $Y(A)$: The average mass numbers now come out at the correct asymmetry, and the computed variances are no longer too small (sections 7.2 and 7.3). Both improvements were possible since the properties of the *scissioning nucleus* were considered and not those of the fragments (section 9.4). For example, the magic numbers of the fragments suggest that the average mass number should be 132, whereas nature insists on about 140 for most of the actinides.

1.4. Applications

In all, the *predictive* power of the theory has been increased by random neck rupture and multichannel fission. We can compute now the neutron multiplicity $\bar{\nu}(A)$, mean masses $\bar{A}_c$, mean total kinetic energies $\overline{\mathrm{TKE}}_c$, and the corresponding standard deviations $\sigma_{A,c}$ and $\sigma_{E,c}$ for each exit channel c separately (section 7.1, chs. 4, 6 and 9) where the accuracy of prediction decreases with the position in the list. We can even have relative estimates of the channel probabilities p_c (section 8.3).

Guided by the theoretical analysis experimenters know now how to decompose mass distributions $Y(A, \mathrm{TKE})$ as they depend not only on the fragment mass number A, but also on the total kinetic energy TKE of that particular partition (sections 6.1 and 8.5). This is valuable, of course, for comparisons. However, this approach is much more important for the *reduction of data bases*. Instead of searching through endless files one may now obtain the same or even more information from a small table. Similar progress has been made for the neutron multiplicities $\bar{\nu}(A, \mathrm{TKE})$ (section 8.5), and after some time suitable decompositions for all the other exit channel observables will be available.

Still another application might be feasible: nuclear fission has long been known as the most efficient creator of chemical elements. This fact is utilized for numerous purposes. Unfortunately, for a certain fissile nuclide the distribution $Y(A)$ of fragment masses was fixed. However, now it has been discovered that even tiny changes in the entrance channel are enough to *reshape the mass distribution* [1.8]. In other words, one may suppress certain isotopes and promote others instead (section 7.5).

1.5. Historical notes, past and future

Multichannel fission and random neck rupture are the main topics of this review. As always, some scrutiny reveals that the underlying ideas were announced long ago.

Turkevich and Niday [1.9] were probably the first who interpreted the mass distribution from thorium in terms of two fission channels. The first substantial analysis was made then by Britt and co-workers [1.10] who deciphered, in a way that is now recognized as being entirely correct, the yield $Y(A, \mathrm{TKE})$ of actinium. Despite this remarkable success, multichannel fission disappeared almost completely from public consciousness. It is probably the merit of Hulet and his colleagues [1.11] that multichannel fission has survived and prospered.

From theoretical considerations, Pashkevich discovered two fission channels in lead [1.12]. His work was exceptional at that time since he considered the shells of the scissioning nucleus while others still stuck to the shells of the fragments.

The first description of random neck rupture and the idea that it might be useful for the prediction of neutron multiplicities was given by Whetstone [1.13]. Later on, Karamyan et al. [1.14] could not explain large variances in induced fission with conventional theories. So they too proposed random neck rupture as a possible way out and developed the first quantitative elements of the theory. That a certain instability known from hydrodynamics, the *Rayleigh instability*, should be significant for nuclear scission, was recognized first by Griffin and Kan [1.15].

The disadvantage of the present theory is its patchwork character. What one would like to do is to solve the Schrödinger equation for the multifermion problem. Multichannel fission and random neck rupture should then be obtained as mere byproducts. Nevertheless, the physics behind multichannel fission and random neck rupture is elementary. It is hardly conceivable that better theories make it disappear. See, for example, in fig. 1.1 pictures from a TDHF calculation. The pictures illustrate

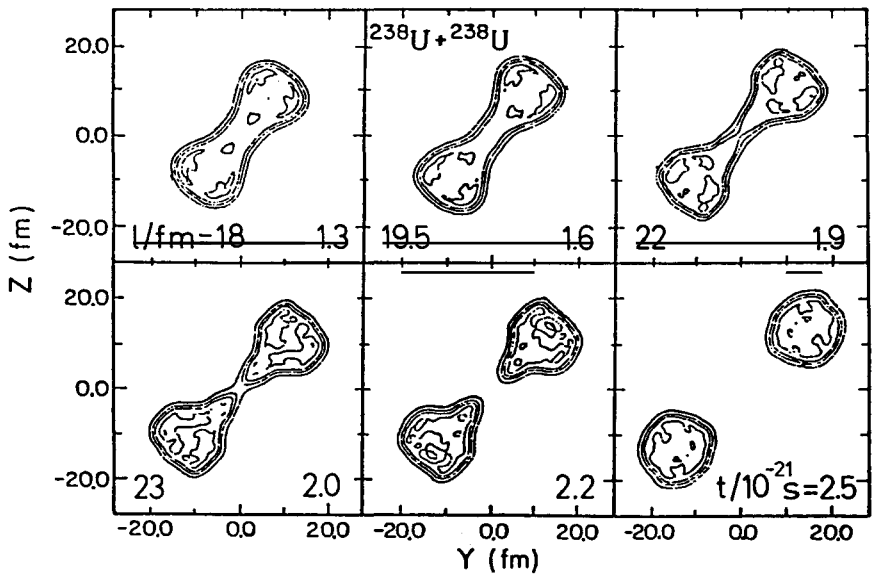

Fig. 1.1. Time evolution of nuclear scission according to TDHF [1.16]. Shown are contours of constant density in the Y–Z plane for a system consisting of $Z_{cn} = 184$ protons with $A_{cn} = 476$ nucleons in total. The times t are noted in the right lower corners of every instance. The semilengths l of the scissioning complex are given in the lower left corners. Suspicious readers may measure these lengths for themselves.

rupture in a multifermion system but do not exhibit the simplicity of the underlying physics. Instead, the fundamentals of rupture can be derived on a piece of paper (section 3.4). To recognize how close the results of extensive numerical calculations and of simple analytical arguments agree one can use eq. (5.1), which is a result of these simple considerations. The equation purports that a nucleus scissions as soon as its semilength l becomes larger than 2.4 times its (hypothetical) compound radius r_{cn}. The hypothetical compound radius is about 9 fm for $^{238}U + ^{238}U$. The critical semilength is hence 22 fm, and indeed fig. 1.1 exhibits rupture at a semilength of 22 fm.

Many important subjects of fission research will not be touched on in this report. The reader can obtain information on the present status of the subject from [1.17, 1.18].

1.6. Suggested reading

The paper contains three key sections, 3.1, 6.2 and 7.1, where the fundamental ideas are briefly explained. We put great emphasis on experimental verification, chs. 5, 7 and 8 and section 6.4. Theoretical recipes are specified in the chs. 2, 4 and 9 and section 6.3. The latter are boring, but had to be written to facilitate checking of the computed results.

2. What do scissioning nuclei look like?

2.1. Degrees of freedom

There is no shortage in representations of nuclear shapes, see for example Hasse's collection [2.1]. Such representations are suitable for fission if the following conditions are satisfied:

(i) A shape representation must have *three essential degrees of freedom*: stretching of the nucleus, thinning of the neck and deformation to asymmetry.

(ii) A *single sphere and two fragments* should be among the allowed configurations.

(iii) The *flatness of the neck* must be an independent variable.

The first two conditions are classics. Condition (iii) is more modern: without a flat neck, random neck rupture cannot take place.

Shape representations are written in cylindrical or spherical coordinates. Spherical coodinates are not considered because they cannot comply with condition (ii). One has to use cylindrical coordinates or an equivalent, a fact realized many years ago [2.2]. However, most popular representations of this type still disregard condition (iii). For example, in the representation [2.3] in which two spheroids are connected by a hyperbolic neck, a flat neck can be achieved only for large neck radii or elongated spheroids. Similar constraints exist for a representation based on Cassinian ovals [1.12] and also for the (h, c) representation made famous in the Funny Hills [1.2]. Thus, there was a need to generalize these descriptions. The shape representation to be introduced in section 2.4, for example, is an extension of the approach in which two spheroids are connected by a hyperbolic neck.

There is no doubt that all existing representations permit similar generalizations. However, comparison of the results obtained with different representations is cumbersome if these results are displayed as functions of technical parameters. The h and c mentioned above are such technical parameters; they have some relation to the shape but generally a complicated one, which is hard to translate to other representations. Such translations, however, are unavoidable not so much because special theoreticians favor special shape representations, but all the more because numerical or physical

reasons force the use of different representations for different tasks. The only way out of this dilemma is to use shape parameters with obvious geometric meanings. A suitable set is

$$l,\ r,\ z,\ c,\ s\,, \tag{2.1}$$

see fig. 2.1. The *semilength* l measures the elongation of the nucleus; we take the semilength instead of the total extension since we want l to coincide with the radius r_{cn} when the shape is a sphere. r is the radius of the neck. As long as there is no neck, r indicates the size of the shape's belly; again, for the spherical "compound nucleus" r agrees with r_{cn}. z gives the position on the neck where the neck is thinnest or where the shape is thickest if the neck does not yet exist. c is the curvature of the neck, with positive values if a constriction exists and negative ones in the opposite case. c can be visualized as the inverse of the curvature radius, cf. fig. 2.1. To be precise, we define c as r_{cn}^2/r_{cur}. This is not more than the multiplication with a constant and has the advantage of giving c the same dimension as all these parameters, namely length. Finally, s describes the position of the centroid. Hence z and s are both parameters of asymmetry, and they are both measured relative to the geometric center of the shape.

In addition to their obvious meaning, the parameters l, r, z, c and s have the advantage of being *defined for all shapes*. Another benefit of these parameters is their *limited range*: for all fission problems we are sure that they vary within a hypercube with edges between -30 fm to $+30$ fm.

The parameters (2.1) have no means of expressing axial asymmetry. In other words, the shape function has the form

$$\rho = \rho(\zeta) \equiv \rho_{\text{shape}}(\zeta; l, r, z, c, s)\,. \tag{2.2}$$

The angle φ known from cylindrical coordinates ρ, φ, ζ does not occur.

2.2. Generalized Lawrence shapes

Square eq. (2.2) and write the right-hand side as a power expansion of ζ. This produces the *generalized Lawrence shapes* [2.4]:

$$\rho^2(\zeta) = (l^2 - \zeta^2) \sum_{n=0}^{N} a_n (\zeta - z)^n\,, \tag{2.3}$$

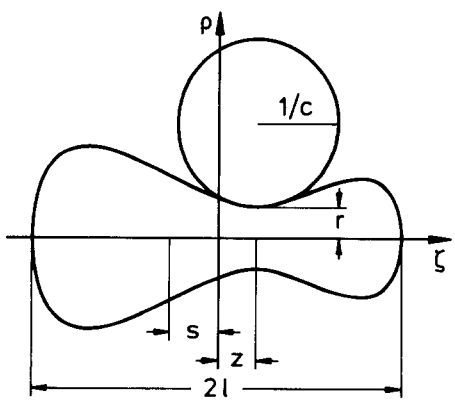

Fig. 2.1. Visualization of the degrees of freedom l, r, z, c and s. The surface depicted is a special Lawrencian shape of the class (2.3) displayed in the coordinates ρ and ζ. Non-dimensional units are used: lengths are measured as multiples of r_{cn}. Otherwise r_{cn}^2/c instead of $1/c$ would be the curvature radius of the neck. The picture is taken from the movie [2.5].

valid for $-l \le \zeta \le l$. The leading factor $l^2 - \zeta^2$ provides for rounded heads. The expression after the summation symbol serves to model the particulars of the shape.

The coefficients a_n are examples of technical parameters. We replace them by the geometrical ones (2.1). This is easy since the geometrical parameters are fixed by analytical expressions. l is already contained explicitly in (2.3). The neck radius r is defined by

$$\rho^2(\zeta = z) = r^2 , \tag{2.4}$$

but simultaneously we have to make sure that the shape is actually thinnest or thickest at $\zeta = z$:

$$\frac{\mathrm{d}\rho^2(\zeta = z)}{\mathrm{d}\zeta} = 0 . \tag{2.5}$$

The curvature c comes in via

$$\frac{\mathrm{d}^2\rho^2(\zeta = z)}{\mathrm{d}\zeta^2} = \frac{2cr}{r_{\mathrm{cn}}^2} , \tag{2.6}$$

and for the center of mass s we have

$$\int_{-l}^{l} \zeta\rho^2(\zeta)\,\mathrm{d}\zeta = s\int_{-l}^{l} \rho^2(\zeta)\,\mathrm{d}\zeta \tag{2.7}$$

by definition. Its right-hand side can be simplified if volume conservation

$$\int_{-l}^{l} \rho^2(\zeta)\,\mathrm{d}\zeta = \tfrac{4}{3}r_{\mathrm{cn}}^3 \tag{2.8}$$

is kept in mind.

Equations (2.4–2.8) impose five conditions on the Lawrence shape (2.3). To have them satisfied takes five coefficients a_n or, expressed differently, $N = 4$ is the upper limit of the sum in (2.3). Due to the somewhat sophisticated arrangement of ζ in (2.3), conditions (2.4–2.8) can be evaluated successively:

$$a_0 = \frac{r^2}{l^2 - z^2} , \tag{2.9}$$

$$a_1 = \frac{2a_0 z}{l^2 - z^2} , \tag{2.10}$$

$$a_2 = \frac{cr/r_{\mathrm{cn}}^2 + a_0 + 2a_1 z}{l^2 - z^2} , \tag{2.11}$$

$$\begin{aligned} a_3 = {} & [sr_{\mathrm{cn}}^3(15l^4 + 210l^2z^2 + 175z^4) + (r_{\mathrm{cn}}^3 - a_0 l^3)(60l^4 z + 140l^2 z^3) - a_1(3l^9 - 18l^7 z^2 - 105l^5 z^4) \\ & - a_2(6l^9 z + 4l^7 z^3 + 70l^5 z^5)]/(9l^{11}/7 - 9l^9 z^2 - 3l^7 z^4 - 35l^5 z^6) , \end{aligned} \tag{2.12}$$

$$a_4 = \frac{-35sr_{cn}^3 + 7a_1l^5 - 14a_2l^5z + a_3(3l^7 + 21l^5z^2)}{12l^7z + 28l^5z^3} . \tag{2.13}$$

Clumsiness in the relations between the geometrical and technical parameters is typical and often much worse than here. To keep it aloof from discussions on physics is almost mandatory.

Looking for changes depending on the five shape parameters (2.1) means roaming through a five-dimensional space. Without any idea what the landscape looks like, one goes astray. So for a first orientation, rambling through a subspace is useful. One of our favorite subspaces was

$$l, r, z . \tag{2.14}$$

Equation (2.3) was kept, but N reduced to two. In this case equations (2.9) and (2.10) remain valid, but (2.11) must be replaced by

$$a_2 = \frac{r_{cn}^3 - a_0l^3 + a_1l^3z}{l^5/5 + l^3z^2} , \tag{2.15}$$

and equations (2.12–2.13) are cancelled. Moreover, the subspace

$$l, r, s \tag{2.16}$$

was frequented. For these strolls, the representation (2.3–2.13) was not changed at all; the missing parameters z and c were determined by minimizations of the liquid-drop energy (see section 9.1 below).

Both restrictions (2.16) and (2.14) satisfy the conditions (i) and (ii) of section 2.1 but violate (iii): a strongly curved neck is obtained for almost all the shapes near scission.

2.3. *The fragment mass number A*

A look at (2.2), (2.14) and (2.16) shows that the many ways by which asymmetry can be expressed become a problem for comparisons. The mass number of the "left-hand-side fragment"

$$A(z_r) = \frac{3A_{cn}}{4r_{cn}^3} \int_{-l}^{z_r} \rho^2(\zeta)\, d\zeta \tag{2.17}$$

unifies the asymmetries, and moreover we get hold of a variable that can, if $\rho(\zeta)$ models two nascent fragments, be measured directly. Formula (2.17) is usually applied to such configurations. The rupture position z_r can vary all over the neck.

2.4. *A real flat-neck representation*

The Lawrence shapes (2.3) are still somewhat disadvantageous because the curvature of the neck as defined in eq. (2.6) is a local property: small c entails a small second derivative of $\rho(\zeta)$ only at $\zeta = z$; the neck may be quite curvy at neighbor positions. A representation which guarantees a *globally flat*

neck, is

$$\rho(\zeta)=\begin{cases}(r_1^2-\zeta^2)^{1/2} & -r_1\le\zeta\le\zeta_1\,,\\ r+a^2c\left(\cosh\dfrac{\zeta-z+l-r_1}{a}-1\right) & \zeta_1\le\zeta\le\zeta_2\,,\\ [r_2^2-(2l-r_1-r_2-\zeta)^2]^{1/2} & \zeta_2\le\zeta\le 2l-r_1\,.\end{cases} \tag{2.18}$$

This class of shapes is defined for $-r_1\le\zeta\le 2l-r_1$. An example is depicted in fig. 2.2. Several of the parameters met in (2.18) are familiar: the semilength l, the neck radius r, the position z of the "dent" on the neck, and the neck curvature c. A new parameter is, for example, *the extension a* of the neck. In fact, with a large a one may keep all higher derivatives small and hence provide for a globally flat neck. The radii r_1 and r_2 of the spherical heads are also new, as are the transitional points ζ_1 and ζ_2 where the three parts of (2.18) join.

Altogether we have nine parameters at our disposal. Five of them can be eliminated by trivial requirements from geometry: at the transitional points, the shape has to be continuous and continuously differentiable:

$$\rho(\zeta=\zeta_1)\,, \tag{2.19}$$

$$\rho(\zeta=\zeta_2)\,, \tag{2.20}$$

$$\frac{\partial\rho(\zeta=\zeta_1)}{\partial\zeta}\,, \tag{2.21}$$

$$\frac{\partial\rho(\zeta=\zeta_2)}{\partial\zeta} \tag{2.22}$$

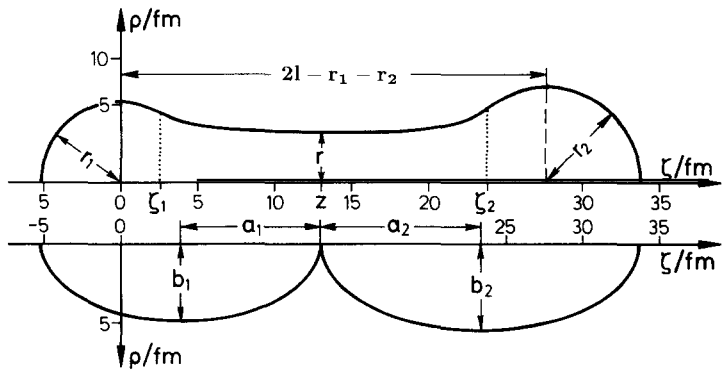

Fig. 2.2. The flat-neck representation (2.18), upper part, and the embedded spheroids (2.26, 2.27), lower part. Note the different origin of the coordinates ρ and ζ as compared to that in fig. 2.1. This entails an offset for the position z by $l-r_1$. The shape shown here is a *prescission shape* constructed for a deep-inelastic heavy-ion reaction where xenon was fired at bismuth [2.6]. Lengths are measured in femtometers and should be realistic with an accuracy of 10%.

are all continuous. And, of course, volume conservation must be guaranteed:

$$\int_{-r_1}^{2l-r_1} \rho^2(\zeta)\,\mathrm{d}\zeta = \tfrac{4}{3}r_{\mathrm{cn}}^3 . \tag{2.23}$$

For a really flat neck we stipulate

$$c \rightarrow \text{minimum} . \tag{2.24}$$

As can be seen from eq. (2.18), $c = 0$ is generally not possible. One may now consider

$$l,\ r,\ z \tag{2.25}$$

as independent variables. They are the same as in (2.14) although the shape is different.

The price one has to pay for the real flat neck are the transcendental equations (2.19)–(2.23). To solve them is time consuming. Moreover, the second and higher derivatives of $\rho(\zeta)$ are discontinuous at ζ_1 and ζ_2. This induces a lot of precautions to keep the numerical processes convergent.

2.5. The embedded spheroids

As we have fig. 2.2 directly in view, it seems sensible to discuss another geometrical construction, namely, the *embedded spheroids*. When a nucleus scissions, it decays into fragments on which the strong surface tension quickly smoothes all the corners and edges. Therefore we model the newborn fragments as two spheroids in contact.

Their major axes a_1 and a_2 [not to be confused with the coefficients a_n of (2.3)] are fixed by the total length $2l$ and the actual rupture point z_r [z_r is the variable introduced in eq. (2.17)],

$$a_1 = \tfrac{1}{2}(r_1 + z_r) , \qquad a_2 = l - \tfrac{1}{2}(r_1 + z_r) . \tag{2.26}$$

The minor axes b_1 and b_2 follow from volume conservation:

$$b_1^2 = \frac{3}{4a_1}\int_{-r_1}^{z_r} \rho^2\,\mathrm{d}\zeta , \qquad b_2^2 = \frac{3}{4a_2}\int_{z_r}^{2l-r_1} \rho^2\,\mathrm{d}\zeta . \tag{2.27}$$

These formulas are valid if the coordinate origin is as shown in fig. 2.2. They thus hold for the shape parametrization (2.18). Slight modifications are required to make them suitable for the Lawrencian shapes (2.3).

The embedded spheroids are used to estimate the repulsion between the fragments and the energies of deformation that the fragments have immediately after formation.

2.6. Areas of application

What can one do with the shape classes defined in the previous sections? For potential energy calculations based on the liquid-drop model the most primitive class of Lawrencian shapes (2.14) is

sufficient. For us it was even a major disappointment [2.7] to see how inessential the dependence on the neck curvature c is. In addition, in potential energy calculations with shell effects many valid results can be obtained with (2.14) or (2.16). However, the barriers become more realistic with the five parameters (2.1), and certain details of the fission channels also change if more than three degrees of freedom are taken into account. However, the relative insensitivity of the potential energies with respect to neck curvature is the reason for the success of the primitive shape representations.

One area where the primitive shape representations fail completely is dynamics. To see the instabilities underlying random neck rupture, the inclusion of the curvature c is indispensable. In this context the representation (2.18) was so useful that numerical discomforts were set aside wherever it seemed possible. Up to the present we use (2.18)–(2.24) to calculate measurable quantities from theory.

3. Fundamentals of random neck rupture

3.1. What you must know to become a random neck rupturer

Quantities such as the mass yield $Y(A)$, the neutron multiplicity $\bar{\nu}(A)$ and the total kinetic energy $\overline{\mathrm{TKE}}(A)$ are *slaves of the prescission shape*. You look at the data and know the originating prescission shape, without any computation.

It is especially simple with the *total kinetic energy* $\overline{\mathrm{TKE}}$. This quantity is an inverse measure of the prescission shape's length. High kinetic energies indicate a short prescission shape, low $\overline{\mathrm{TKE}}$s a long one. The idea behind this is that the nucleus stretches slowly until rupture. The prescission shape is the "last halt". Then the rupture takes place, and Coulomb repulsion accelerates the fragments without any hindrance.

Almost as simple is the relation of the prescission shape to the *variance* σ_A^2 *of the mass distribution* $Y(A)$. It too measures the prescission shape's length, see figs. 3.1a and 3.1b. More precisely one should say: it measures the length of the neck. Namely, random neck rupture produces different fragments by chopping the neck at different positions. The longer the neck, the more possibilities to chop it and the larger the variety of fragments.

The *average mass number* $\bar{A}$ *of* $Y(A)$ expresses the asymmetry of the prescission shape. We expect the most frequent rupture at the place where the neck is thinnest. When the prescission shape is asymmetric, this place is shifted away from the center. Consequently, mostly one light and one heavy fragment are produced, and a double-humped yield $Y(A)$ is obtained, as shown in fig. 3.1d. For decreasing asymmetry the two humps merge until a single bump remains, compare the series of figs. 3.1d, c and b.

It takes more intuition to understand the neutron multiplicities $\bar{\nu}(A)$. To start easy, let us first state the relations as rules:

(1) A large average neutron multiplicity $\bar{\nu}$ is caused by a long prescission shape (cf. figs. 3.1a and b).

(2) A symmetric prescission shape gives rise to a multiplicity $\bar{\nu}(A)$, which increases steadily with the fragment mass number A, see fig. 3.1b, whereas an asymmetric prescission shape causes a sawtooth, fig. 3.1d.

These rules are based on the embedded spheroids introduced in section 2.5 to model the newborn fragments. Their deformations turn into an excitation, and this excitation is finally released by evaporation of neutrons (that also other particles can be emitted will be neglected for the moment).

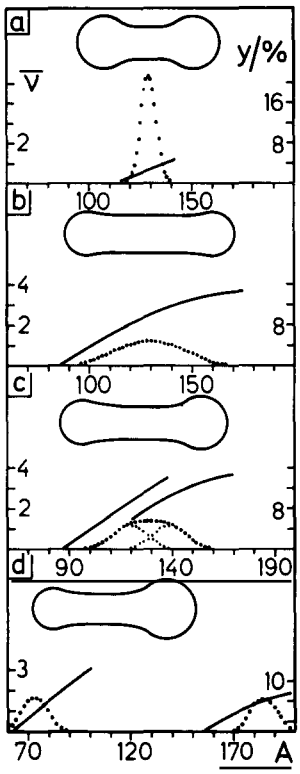

Fig. 3.1. Some important correlations that a prescission shape mediates. Shown are mass yields Y (dotted lines, right-hand-side scales) and neutron multiplicities $\bar{\nu}$ (solid lines, left-hand-side scales) as functions of fragment mass number A. Although the pictures were made for general illustration, they display the components that should be relevant for the fission of ^{258}Fm. In terms to be explained in sections 7.1 and 8.5: part (a) shows a supershort prescission shape and its products, part (c) the standard and part (d) the superasymmetrical prescission shape. The figure appeared first in ref. [3.1].

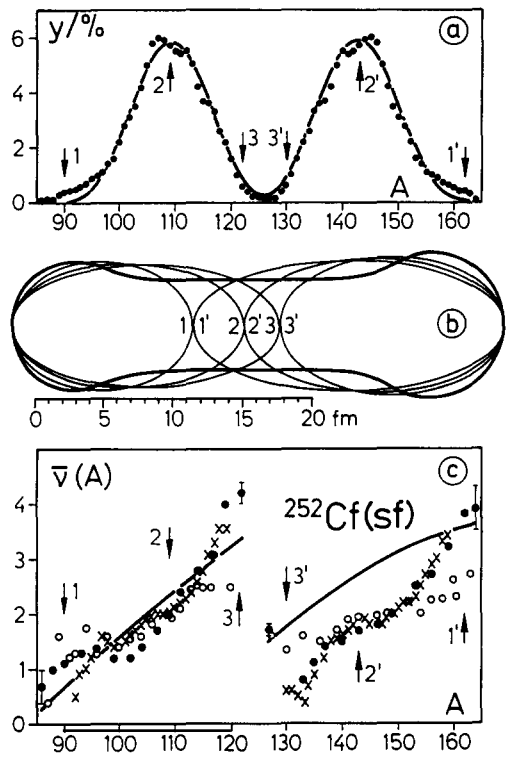

Fig. 3.2. Random neck rupture and the sawtooth shape of the neutron multiplicity $\bar{\nu}(A)$. In the central part, (b), the prescission shape valid for the spontaneous fission of ^{252}Cf is depicted. More precisely, it is approximately the *standard* prescission shape. Some embedded spheroids are inserted. They are marked by numbers, 2 and 2′, for example. The 2 and 2′ fragments are produced with a large probability because the neck of the prescission shape is thinnest at the 2–2′ position. Therefore, in part (a), arrows 2 and 2′ point at the maxima of the yield $Y(A)$. Rupture at 3–3′, in contrast, rarely happens due to the increased thickness of the neck. It is now most important to notice that the split at 3–3′ gives rise to fragments that are about equal by mass but very different by deformation. As the neutron multiplicity $\bar{\nu}(A)$ increases with deformation, the data shown in part (c) become understandable. Lines represent the results of random neck rupture while experimental material is displayed by symbols. The figure stems from [3.2] where references to the early experimental papers can also be found.

Since long prescission shapes make fragments with large deformations, it is now clear that long prescission shapes give rise to more neutrons, see rule 1 above. The meaning of rule 2 is detailed in fig. 3.2: in an asymmetric prescission shape fragments are embedded with about equal masses but very different deformations. They generate the sawtooth.

The objection against this type of reasoning is that data are given, but prescission shapes may be constructed at will. However, since from *one* prescission shape at least *three* different observables can be derived, the prescission shape can be construed as a means to correlate observables. The two most important relations are:

(i) Kinetic energies $\overline{\mathrm{TKE}}$ are anticorrelated with the variances σ_A^2 of the mass distributions $Y(A)$.
(ii) The deviation of $\bar{A}$ from mass symmetry is correlated with the sawtooth of $\bar{\nu}(A)$.

There are many more relations emanating from the picture presented, but most of them are not specific for random neck rupture. For example, it follows from random neck rupture that high $\overline{\mathrm{TKE}}$'s come with low $\bar{\nu}$'s and vice versa. Every model that does not disregard energy conservation reproduces this type of dependence.

In low-energy fission, no exception from the relations (i) and (ii) is known. In heavy-ion-induced reactions, relation (ii) is still debated, see section 5.7. However, more convincing than qualitative relations are quantitative comparisons. To demonstrate how these can be made is the purpose of the next chapter. However, first the physical foundations of random neck rupture will be discussed.

3.2. Scission as a sequence of instabilities

Ordinary fission needs at least three instabilities for its evolution:
(i) passing the barriers,
(ii) the shift instability,
(iii) the capillarity instability.

Surmounting the barrier(s) is the element of fission, which was considered from 1939 on, see [3.3]. Even today it is sometimes considered as *the* explanation of fission, though it is only the first step of a complicated walk. Shortly behind the last barrier the neck starts to appear. At first it still has a bump in the middle. Under further stretching the neck becomes perfectly flat, and after this it will thin in its central part. The curvature thus develops from negative through zero to positive values. On a flat neck, strangulation may happen everywhere. One can state this in a different way: the position of future constriction, which is at this stage just a tiny dent, can *shift* on a flat neck as *in an unstable motion* [3.4, 2.5]. Finally the *capillarity* or *Rayleigh instability* ramps [3.5–3.7]. This is the time of constriction. The shift is stopped or, in other words, the asymmetry is frozen, and the nucleus disrupts.

Random neck rupture is a description that summarizes the effects from the shift and the Rayleigh instabilities. Neck rupture occurs because of the Rayleigh instability, while the shift provides for randomness. It takes some of Rayleigh's formulas to calculate a prescission shape and ideas from the shift instability to set up a suitable formula for the rupture probability.

Instabilities are by definition acts of dynamics. Nevertheless one may learn much about them from the potential energy alone. Refer to fig. 3.3. It is a contour plot of the potential energy of a fissioning nucleus. The unstable stretching behind the saddle and the onset of the capillarity instability can be inferred from this picture. One just has to look for those locations where the system starts to gain energy when it stretches or constricts.

Here it must be clear that the Rayleigh instability is by no means new in nuclear physics. Contour plots as in fig. 3.3 have been made for decades. For example, the onset of the Rayleigh instability is identical with Strutinsky's *critical point* [3.9]. But there were two problems with earlier approaches. First, the capillarity instability was not recognized in that characteristic twist of the potential energy. Therefore no one realized that this twist is just effected by surface tension, Coulomb repulsion playing only a subordinate part. As a consequence, a certain simple scaling relation [equation (3.3) below] could not be found and hence no prescission shape defined. The second shortcoming was related to the so-called *overstretching*: from the potential energy alone one reads only the *onset* of the capillarity instability. At the onset, the constricting force is close to zero. Because of inertia the nucleus continues stretching and ruptures only when the constricting force becomes strong enough.

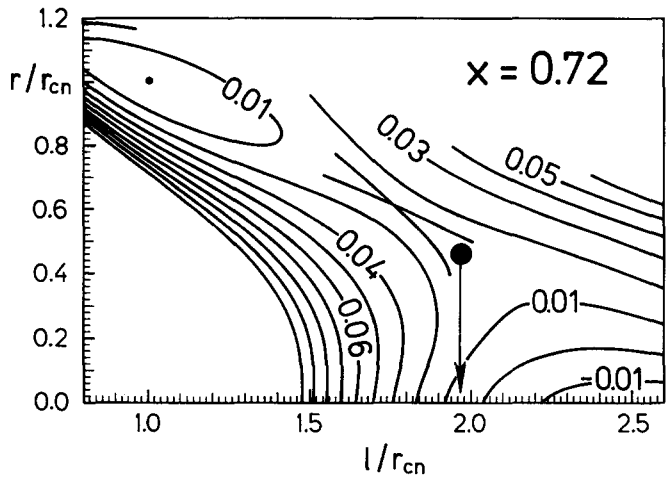

Fig. 3.3. Unstable stretching behind a saddle and onset of rupture visualized in a potential energy surface. The saddle point appears as a rotated × while the onset of rupture is marked by a full circle and arrow. This contour plot displays pure liquid-drop energies in the plane of semilength l and neck radius r for symmetrical shapes [3.8]. Lengths are given in units of the radius $r_{cn} = r_0 A_{cn}^{1/3}$ of the compound nucleus. Energies are measured as multiples of the surface energy $E_{sur}^{sph} = 4\pi\gamma_0 r_{cn}^2$ with the zero for the compound shape at $l = r = r_{cn}$. The fissility x is defined in equation (4.17). $x = 0.72$ belongs approximately to ^{213}At.

The shift instability is completely dominated by inertia and cannot be visualized by pictures such as fig. 3.3. But there are means to display it using the dynamical curvature tensor or, for simplification, by the Gaussian curvature of a dynamical system [3.4].

3.3. *The shift instability*

The shift instability is elucidated best by a movie [2.5]. For a first acquaintance look at fig. 3.4. Below one can see an idealized nucleus just after the shift instability. The nearly invisible dent on the neck, indicated by the triangles, went to the right. Prior to the shift the triangles sat exactly over the open square, which marks the geometrical center of the shape. The arrows inside display the velocity

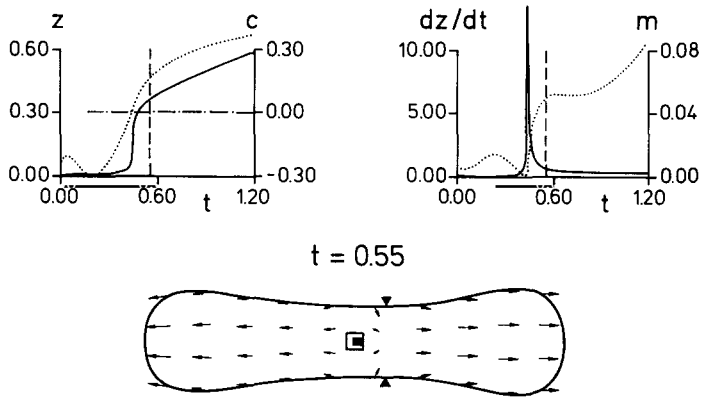

Fig. 3.4. The shift instability. This is a single shot from the movie [2.5]. The vertical lines in the upper inserts indicate the actual time, namely $t = 0.55$ at this instant. All units are dimensionless, based on the radius of the spherical drop, on its surface energy and its mass.

field. The point to be noticed is that almost all of the material needed for stretching comes from the heads, while there is nearly no motion at the center. Hence large shifts of the dent take place without sizeable physical mass motion.

In the left upper part of fig. 3.4 z (full line) and c (dotted) are shown as functions of time t. The shift instability is characterized by the steep rise of the full line. This is a large change of the dent's location z within a short time. We see this happens when the curvature c moves through zero. In other words, the shift instability takes place when the neck is perfectly flat. The later increase of z results only from stretching. It is the same as the motion of a spot on an elastic when the elastic is strained.

The curves on the upper right-hand side are graphs of velocity $\mathrm{d}z/\mathrm{d}t$ (full line) and of inertia m (dotted line) as functions of time. $\mathrm{d}z/\mathrm{d}t$ contains about the same information as z: the steep rise is replaced by a sharp spike. The spike marks the shift instability. At the front of the spike the inertia, shown by the dotted line, goes to zero. This is another way of stating that the shift instability can take place because it needs nearly no physical mass motion. Later on during fission, the dent deepens. Its shift now necessitates large physical mass motion. Hence the inertial parameter m also increases so that the dent is effectively frozen in.

Two additional pieces of information can be drawn from fig 3.4: first, the shift instability happens before squeezing and, second, the geometrical center and centroid (the two squares) stay close to each other. The first item is in contradiction with the *scission-point model* [1.4], in which it is assumed that the mass fluctuations take place after the squeezing. The second point illustrates an inadequacy of an often used *dynamical model* [2.3]. In this model mass fluctuations are effected by transport through a comparatively thin neck. But such a redistribution of masses separates the geometrical center from the center of mass. Figure 3.4 demonstrates that such a mechanism does not prevail.

The computations that gave rise to fig. 3.4 were based on Eulerian hydrodynamics with five degrees of freedom: the semilength l, the neck radius r, the position z of the dent, the curvature c and the center of mass s, as defined in fig. 2.1. Underlying this was the shape representation (2.3). The essential novelty was the way in which the *curvature* c was considered. The inertial parameters $m_{kj}(l, r, z, c, s)$, $k, j = 1, \ldots, 5$ were computed using a procedure inspired by Hasse et al. [3.10] but with improved accuracy [3.11]. Only surface tension was included in the potential energy $U(l, r, z, c, s)$. Coulomb effects were disregarded as being inconsequential for the problem at hand.

The complete equations of motion, as used for the trajectories shown in fig. 3.4, are

$$\sum_{j=1}^{5} m_{kj}\ddot{z}_j = \sum_{i=1}^{5}\sum_{j=1}^{5}\left(\frac{1}{2}\frac{\partial m_{ij}}{\partial z_k} - \frac{\partial m_{jk}}{\partial z_i}\right)\dot{z}_i\dot{z}_j - \frac{\partial U}{\partial z_k}\,. \tag{3.1}$$

The dynamical variables $\{l, r, z, c, s\}$ are written here as $\{z_i | i = 1, \ldots, 5\}$. Dots indicate time derivatives. The inertial tensor is not diagonal and its elements depend on the dynamical variables. This is why the eqs. (3.1) look much more complicated than Newton's equation of motion for a mass point. Nevertheless one may understand the shift instability from an extremely reduced expression, namely

$$\ddot{z} = F/m(c)\,. \tag{3.2}$$

Here z again means the location of the dent on the neck, F comprises the forces described either by the potential energy or by the inertial terms on the right-hand side of eq. (3.1). $m(c)$ is the inertial parameter displayed in fig. 3.4; it is m_{33} in terms of eq. (3.1). The dependence on the curvature c is

stressed because it is by far the most drastic one. Equation (3.2) says: to produce a large acceleration in z, there is no need for large forces F. A small inertial parameter $m(c)$ does the same. This is also the message of fig. 3.4.

Summarizing one may say that the shift instability arises because for fission a nucleus has to change from a spheroidal to a necked-in configuration. Trivially, on this transition the neck must become flat or, in equivalent terms, its curvature goes to zero. If the curvature is zero, no inertia stops the shift of the nascent dent. This effectively amplifies small fluctuations and generates the large mass fluctuations that previous theories failed to explain.

3.4. The capillarity or Rayleigh instability

The capillarity instability accomplishes what the shift instability prepares; it takes the dent where it is and deepens it until two fragments appear. A characteristic of the Rayleigh instability is

$$2l = 11r\,, \tag{3.3}$$

which relates the total length $2l$ of the prescission shape with its neck radius r [3.2, 3.8, 3.12, 3.13]. The relation is so important that it became the trademark of random neck rupture. In principle, equation (3.3) is nothing other than a slightly modified relation first derived by Rayleigh. It takes three steps to find the coefficient 11:

(i) look for the *onset* of the capillarity instability,
(ii) take *overstretching* into account,
(iii) consider the *finiteness* of the fissioning nucleus.

As will be seen from the derivation, one must not claim that the magic 11 is more accurate than by 11%. But within such limits it is a quite universally usable constant. In particular, it does not depend significantly on the Coulomb repulsion [3.8, 3.9]. Moreover, it is not perceptibly changed by rotation [3.14], and also neither viscosity nor compressibility nor surface diffuseness seem to play a great role, see section 3.5. Only nuclear shell effects can modify eq. (3.3) significantly [3.2, 3.15], see section 9.3.

Now to the discussion of step (i). Rayleigh studied an infinite cylinder on which a sinusoidal wave is imposed [3.7]. Hence the radius ρ of the cylinder can be written as

$$\rho(\zeta) = r(\varepsilon) - \varepsilon \cos(\pi\zeta/l)\,. \tag{3.4}$$

ζ represents, as in chapter 2, the coordinate along the axis of the cylinder. Equation (3.4) may be interpreted as the representation of a shape similar to those discussed in chapter 2. ε is the degree of freedom here; increasing ε indicates rupture. We expect a dependence on time like

$$\varepsilon = \varepsilon_0\, \mathrm{e}^{t/\tau}\,. \tag{3.5}$$

Instability takes place if the growth time τ is real and positive. The other symbols in (3.4) were chosen to conform with other sections of this report: r, in particular, will be identified with the radius of the neck and l with the semilength of the scissioning shape. An infinite jet has, of course, no length. Therefore Rayleigh's papers only contain the wavelength λ. However, the replacement $\lambda = 2l$ is obvious.

In eq. (3.4) one must keep in mind that r depends on ε. This is unavoidable since the volume

$$\pi \int_{-l}^{l} \rho^2(\zeta)\,\mathrm{d}\zeta = 2\pi l\, r^2(\varepsilon = 0) \tag{3.6}$$

must be conserved. Although this remark seems trivial, it is important for understanding the mechanism of the capillarity instability: every instability needs two forces that balance each other at its onset. For passing the barrier, see (i) in section 3.2, this is Coulomb repulsion acting against surface tension. But in the capillarity instability both forces come from surface tension alone. When one disregards eq. (3.6), one of these forces is lost.

The two forces that constitute the capillarity instability are these: a sinusoidal deformation of the surface enlarges its area and therefore costs energy. The increase of energy is all the larger, the smaller the wavelength; more precisely it is proportional to l^{-2}. On the other hand, the surface deformation is necessarily accompanied by a reduction of the mean radius since otherwise volume cannot be conserved. This reduction is equivalent to saving surface energy and is independent of the wavelength. Therefore, for short wavelengths the increase of surface energy by deformation will dominate, leading to stability, while for large lengths the decrease due to volume conservation dominates, leading to instability. Since both effects are proportional to the surface tension, the surface tension coefficient cancels so that the border of stability is determined purely by geometry.

Let us make this argument quantitative. First calculate the potential energy

$$U(\varepsilon) = 2\pi\gamma_0 \int_{-l}^{l} \rho[1 + (\mathrm{d}\rho/\mathrm{d}\zeta)^2]^{1/2}\,\mathrm{d}\zeta\,, \tag{3.7}$$

where $\gamma_0 \approx 0.9\ \mathrm{MeV\ fm}^{-2}$ is the nuclear surface tension. Neglecting all terms of third and higher order in ε produces

$$U(\varepsilon) \approx 4\pi\gamma_0 r\, l + \frac{\varepsilon^2}{2}\, 2\pi\gamma_0\, \frac{l}{r}\left[\left(\frac{\pi r}{l}\right)^2 - 1\right]. \tag{3.8}$$

The factor after $\varepsilon^2/2$ is the one that matters. It is customary to denote it as the *stiffness*

$$C = 2\pi\gamma_0\, \frac{l}{r}\left[\left(\frac{\pi r}{l}\right)^2 - 1\right]. \tag{3.9}$$

The stiffness takes a negative sign if $\pi r < l$. With this condition the jet gains energy when a constriction starts to develop.

$$2l = 2\pi r \tag{3.10}$$

thus marks the *onset* of instability.

Just behind the onset, the instability-creating force is still very small. So it takes much too long until a sizeable squeezing is reached. In step (ii), therefore, the dynamics must be regarded. The simplest

equation of motion is

$$M\ddot{\varepsilon} = -C\varepsilon \,. \tag{3.11}$$

The stiffness C is given by (3.9). Finding the inertial parameter M requires the solution of a hydrodynamical boundary value problem.

To this end one determines the velocity potential $\Phi(\rho, \zeta)$ from Laplace's equation as a product of a modified Bessel function $I_0(\pi\rho/l)$ [3.16] with a cosine $\cos(\pi\zeta/l)$, calculates from it the velocity field $\boldsymbol{v} = -\boldsymbol{\nabla}\Phi$, fixes the still unknown multiplicative constant so that the motion at the surface conforms with eq. (3.4), namely

$$\frac{\partial\Phi}{\partial\rho} = -v_\rho = \dot{\varepsilon}\cos\frac{\pi\zeta}{l}\,, \tag{3.12}$$

and evaluates the kinetic energy according to

$$\frac{\rho_0}{2}\int\limits_{\text{(piece of jet)}} |\boldsymbol{v}|^2\,\mathrm{d}V = -\frac{\rho_0}{2}\int\limits_{\text{(surface)}} \Phi\boldsymbol{v}\cdot\mathrm{d}\boldsymbol{A} \approx -\pi\rho_0 r\int_{-l}^{l}\Phi v_\rho\,\mathrm{d}\zeta\,. \tag{3.13}$$

Here ρ_0 denotes the mass density of nuclear matter; in combination with the nuclear unit radius r_0 we have

$$\rho_0 r_0^3 \approx 25\times 10^{-46}\,\mathrm{MeV\,fm^{-2}\,s^2}\,.$$

The inertial parameter is obtained from the kinetic energy by splitting off the factor of $\dot{\varepsilon}^2/2$:

$$M = 2\pi\rho_0 r^2 l\,\frac{I_0(\pi r/l)}{(\pi r/l)I_0'(\pi r/l)}\,, \tag{3.14}$$

where the prime indicates differentiation with respect to the argument.

The growth time of the instability follows from eq. (3.11) in the most elementary manner

$$\tau = (-M/C)^{1/2}\,. \tag{3.15}$$

Consider this expression as a function of l: beyond the onset of instability, the stiffness (3.9) becomes negative and absolutely larger. Therefore, to reduce the growth time, it might seem favorable to increase l over all bounds. But at the same time the inertia (3.14) decreases. In other words, waves that are too long are also not favorable since more and more mass has to move. A simple discussion of the function (3.15) reveals that it has a *minimum* at

$$2l = 1.435\times 2\pi r \approx 9r\,. \tag{3.16}$$

Hence overstretching makes the droplet 1.435 times longer than what one got for the onset.

After the minimum is fixed, one may use eq. (3.15) and the constants given above to estimate the

rupture time:

$$\tau/10^{-22}\,\mathrm{s} \approx [1.5(r/\mathrm{fm})^3]^{1/2}\,. \tag{3.17}$$

Generally times shorter than 10^{-21} s are found.

Finally, in step (iii), finiteness corrections have to be established. In the simplest way one can do this by adding two lids at $\zeta = -l$ and $\zeta = l$ to the surface defined in (3.4). The potential energy (3.7) now reads

$$U(\varepsilon) = 2\pi\gamma_0 \int_{-l}^{l} \rho[1 + (\mathrm{d}\rho/\mathrm{d}\zeta)^2]^{1/2}\,\mathrm{d}\zeta + 2\pi\gamma_0[r(\varepsilon) + \varepsilon]^2\,. \tag{3.18}$$

The stiffness (3.9) is modified accordingly,

$$C = 2\pi\gamma_0 \frac{l}{r}\left[\left(\frac{\pi r}{l}\right)^2 + \frac{r}{l} - 1\right]. \tag{3.19}$$

The onset is obtained by equating the expression in brackets to zero. This yields

$$2l = 1.172 \times 2\pi r \approx 7.4r\,, \tag{3.20}$$

which is to be compared with eq. (3.10).

The inertial parameter (3.14) suffers no modification from finiteness, as can be seen from the middle expression in eq. (3.13): at the lids, the velocity $\boldsymbol{v}$ is perpendicular to the vectorial surface element $\mathrm{d}\boldsymbol{A}$.

Neither overstretching nor finiteness changes the value of $2l/r$ valid for the infinite jet at the onset much. Therefore one may multiply the factors in (3.16) and (3.20) to obtain the change due to both perturbations together. It amounts to $1.435 \times 1.172 \times 2\pi \approx 11$, the number we proclaimed in eq. (3.3).

3.5. The Rayleigh instability under more general circumstances

Rayleigh's criterion experiences only slight modifications if more complexity is taken into account.

For instance, if non-axisymmetric constrictions are admitted [multiply the last term in (3.4) by $\cos m\varphi$], the stiffness (3.9) becomes

$$C = (1 + \delta_{0m})\pi\gamma_0 \frac{l}{r}\left[\left(\frac{\pi r}{l}\right)^2 + m^2 - 1\right]. \tag{3.21}$$

It can change sign only if $m = 0$. Thus we conclude that there is no capillarity instability for non-axisymmetric modes.

Friction expressed by the kinematic viscosity ν_0 in the Navier–Stokes equation leaves the range of instability unchanged. Its main effect is to slacken the growth and to shift the most unstable mode towards smaller values of $\pi r/l$. The lowest order corrections in ν_0 read [3.17]

$$\tau(\nu_0) = \tau + \frac{\nu_0\tau^2}{r^2}\left[2[m^2 + (\pi r/l)^2] - \frac{m^2 I_m(\pi r/l)}{(\pi r/l)I'_m(\pi r/l)} - \frac{(\pi r/l)I'_m(\pi r/l)}{I_m(\pi r/l)}\right] \tag{3.22}$$

and

$$\frac{\pi r}{l}(\nu_0) = \frac{\pi r}{l} - 0.811\nu_0\left(\frac{\rho_0}{\gamma_0 r}\right)^{1/2}; \tag{3.23}$$

$\pi r/l$ and τ have the values given in eqs. (3.16) and (3.17), respectively. When we take a tradable value for viscosity $\eta_0 \approx 6\times 10^{-23}$ MeV fm^{-3} s [3.18], the kinematic viscosity is about $\eta_0/\rho_0 = \nu_0 \approx 10^{21}$ fm^2 s^{-1} so that we end up with a reduction of $\pi r/l$ of about -15%. This is not small, but we shall see that it is partly compensated by surface diffuseness.

The compressibility κ_0 alters the region of instability much less. The smaller inertia hurries the growth, and the most unstable mode is shifted to smaller values of $\pi r/l$. The lowest order corrections in powers of κ_0 are [3.19]

$$\tau(\kappa_0) = \tau + \frac{\kappa_0\rho_0 r^2}{4\tau}\left(\frac{I_m(\pi r/l)}{(\pi r/l)I_m'(\pi r/l)}\right)'\frac{I_m'(\pi r/l)}{I_m(\pi r/l)} \tag{3.24}$$

and

$$\frac{\pi r}{l}(\kappa_0) = \frac{\pi r}{l} - 0.052\,\frac{\kappa_0\gamma_0}{r}\,. \tag{3.25}$$

With $r = 3$ fm and Blaizot's value for κ_0 [3.20], $\kappa_0\gamma_0/r$ is about 0.1 and the shift of $\pi r/l$ is less than 1%. Even smaller is the change of the growth time.

The effect of a finite surface diffuseness (size a), was studied using the Krappe–Nix potential [3.21]

$$U = -2\gamma_0\frac{\partial\psi(a)}{\partial a}\,,\quad \psi(a) = \frac{1}{4\pi a^2}\int \mathrm{d}^3\boldsymbol{r}\,\mathrm{d}^3\boldsymbol{r}'\,\frac{\exp(-|\boldsymbol{r}-\boldsymbol{r}'|/a)}{|\boldsymbol{r}-\boldsymbol{r}'|}\,, \tag{3.26}$$

where the integrations extend over a piece of the cylinder with length $2l$. In the limit $a\to 0$ the conventional surface energy $U = \gamma_0 \times$ surface is recovered. The stiffness is found to be

$$C = (1+\delta_{0m})\pi\gamma_0\frac{l}{r}\left[\left(\frac{\pi r}{l}\right)^2 + m^2 - 1 - \frac{9}{4}\left(\frac{a}{r}\right)^2\left\{\left(\frac{\pi r}{l}\right)^4 + \frac{4m^2-1}{2}\left[\left(\frac{\pi r}{l}\right)^2 + \frac{4m^2-9}{8}\right] + \frac{15}{16}\right\}\right] + \mathrm{O}\left(\left(\frac{a}{r}\right)^4\right). \tag{3.27}$$

For the onset we find

$$\frac{\pi r}{l}(a) = \frac{\pi r}{l} + \left(\frac{3a}{2r}\right)^2 + \mathrm{O}\left(\left(\frac{a}{r}\right)^4\right), \tag{3.28}$$

hence in contrast to (3.23) a shift to larger values of $\pi r/l$. With a realistic value for the surface diffuseness we have $a/r = 0.65/3 \approx 0.22$. This increases $\pi r/l$ at the onset [cf. eq. (3.10)] by $+11\%$.

Résumé: For the Rayleigh instability in nuclear matter we can forget about non-axisymmetric disturbances and compressibility. The viscosity and diffuseness are at the limit of being significant, but their effects on the length scales almost cancel each other.

4. Formulas from random neck rupture for applications

4.1. Unit radius and surface tension

We have to profess now how the prescission shape is actually calculated, and how one may obtain from the prescission shape mass distributions, the total kinetic energies and neutron multiplicities.

For these calculations, two nuclear constants will be necessary, namely the radius unit

$$r_0 = 1.15\ \text{fm} \tag{4.1}$$

and the surface tension coefficient

$$\gamma_0 = 0.9517\left[1 - 1.7828\left(\frac{N_{cn} - Z_{cn}}{A_{cn}}\right)^2\right]\ \text{MeV fm}^{-2}\,. \tag{4.2}$$

N_{cn}, Z_{cn} and A_{cn} are the neutron, charge and mass numbers of the compound nucleus.

The unit radius (4.1) is a charge radius, rather a small value. It was taken to facilitate accurate computation of the Coulomb repulsion between the newborn fragments (section 4.4 below). The formula (4.2) for the surface tension was chosen because it is one of the most familiar expressions [4.1, 4.2]. It will be used for the rupture probability (section 4.3) for which we have in any case only an approximate formula. For the precise calculation of binding energies (4.1) and (4.2) do not fit together. We shall be concerned about this in sections 4.5, 9.1 and 9.3.

4.2. The prescission shape

Let us return to the flat-neck representation introduced in section 2.4. From the free shape parameters l, r and z (2.25) we can eliminate the neck radius r with Rayleigh's relation (3.3). Next we replace the location z of the dent by the fragment mass number A as explained in section 2.3.

To fix the remaining degrees of freedom A and l, two strategies exist. Either we find them from experimental data, associating with A the measured average mass number $\bar{A}$ and with l the average total kinetic energy $\overline{\text{TKE}}$, cf. sections 4.3 and 4.4. Then we obtain the variance σ_A^2 of the mass distribution and the neutron multiplicity $\overline{\nu(A)}$ as results. In some cases to be discussed in sections 5.3 to 5.7 it is sensible to put σ_A^2 in and to extract $\overline{\text{TKE}}$ from random neck rupture.

Otherwise, we find A and l by microscopic calculations as described in ch. 9. Details relevant for the present context are intimated in section 9.3.

The equations (2.19–2.24) defining the flat-neck shape (2.18) are maliciously non-linear. Especially bad is the dependence on the curvature c. An initial value for c can be estimated from a parabola through the points $(\zeta_1, \rho(\zeta_1))$, $(z + l - r_1, r)$ and $(\zeta_2, \rho(\zeta_2))$, see fig. 2.2. But ζ_1 and ζ_2 are a priori not known. Therefore we substitute these points by the approximations $(0, R_1)$, (z, r) and $(2l - R_1 - R_2, R_2)$. R_1 and R_2 are replacements for r_1 and r_2, which are defined by

$$R_1 = r_0 A^{1/3}\,, \qquad R_2 = r_0 (A_{cn} - A)^{1/3}\,, \tag{4.3}$$

with A and $A_{cn} - A$ as the expected mass numbers of the fragments. There is a left-hand side parabola with vertex at (z, r), through $(0, R_1)$ and with curvature c'. Its equation is $R_1 - r = (c'/2)z^2$. The

right-hand side parabola gives rise to the equation

$$R_2 - r = (c''/2)(2l - R_1 - R_2 - z)^2 .$$

Taking the roots of these equations, adding them and estimating $c \approx c' \approx c''$ gives

$$c = 2c_{\mathrm{rel}} \frac{R_1 + R_2 - 2r + 2[(R_1 - r)(R_2 - r)]^{1/2}}{(2l - R_1 - R_2)^2} \tag{4.4}$$

if $c_{\mathrm{rel}} = 1$. Of course, a parabola does not represent a flat neck. Hence $c_{\mathrm{rel}} < 1$ is necessary. We found that c_{rel} values from a broad range

$$0.03 \leq c_{\mathrm{rel}} \leq 0.3 \tag{4.5}$$

give suitable starting values [3.12].

Another difficulty arises in applications to heavy-ion reactions. Here the radii R_{P} and R_{T} of projectile and target are known. One wants to find the prescission shape as a function of these entrance-channel variables. To explore this, the "neck contribution policies"

$$\frac{R_{\mathrm{P}}^3 - r_1^3}{R_{\mathrm{T}}^3 - r_2^3} = \left(\frac{R_{\mathrm{P}}}{R_{\mathrm{T}}}\right)^{\mu} \tag{4.6}$$

with

$$\mu = 1, 2, 3 \tag{4.7}$$

are useful. They mean that the share of mass from the neck, which a fragment receives, is proportional to the projectile's radius ($\mu = 1$), to its surface ($\mu = 2$) or to its volume ($\mu = 3$). Fortunately, the results do not depend significantly on the choice [3.13]. See section 5.3 for a discussion of the physics.

One fixes now $c_{\mathrm{rel}} = 0.1$, say, enters l and A as specific for the physical problem and solves the non-linear system of eqs. (2.19–2.24) and (3.3), replacing A by $z_{\mathrm{r}} = z$ using (2.17). If A has not the meaning of the average mass number of the fragments but rather of the mass number of the projectile, one disposes of (2.17) and takes (4.6) instead. This defines the prescission shape (2.18).

4.3. The yield $Y(A)$

Without fluctuations, the neck would always rupture at the same position, namely at z. With fluctuations, amplified by the shift instability as explained in section 3.3, a slightly different shape is generated so that the neck can break elsewhere. We need the probability that the neck ruptures at an arbitrary position z_{r}. For this one should compute the potential energy $E(z_{\mathrm{r}})$ of the slightly modified shape and compare it with the potential energy $E(z)$ of the most probable shape [3.8]. To simplify this, we replace the difference $E(z_{\mathrm{r}}) - E(z)$ by $E_{\mathrm{cut}}(z_{\mathrm{r}}) - E_{\mathrm{cut}}(z)$ where $E_{\mathrm{cut}}(z_{\mathrm{r}}) := 2\pi\gamma_0\rho^2(z_{\mathrm{r}})$ denotes the energy to be spent for a cut of the most probable shape at the position z_{r}. Note that we do not have to cut; this is accomplished by the capillarity instability. E_{cut} was introduced only for computational convenience.

Hence our ansatz for the rupture probability is the Boltzmann factor

$$W(A) \propto \exp\{-2\pi\gamma_0[\rho^2(z_r) - \rho^2(z)]/T\} . \tag{4.8}$$

The fragment mass number A can be computed from the rupture position z_r according to (2.17). T is the temperature of the prescission shape. For applications in spontaneous fission we estimate T from the excitation energy E_s^* which the nucleus gains as it slides down to scission (see sections 6.2 and 8.2 for details). For applications to induced fission or deep-inelastic reactions energies brought in via the entrance channel are duly taken into account. The theoretical yield to be compared with the measured one finally follows from

$$Y(A) = W(A) + W(A_{cn} - A) . \tag{4.9}$$

4.4. *The total kinetic energy* $\overline{TKE}(A)$

The prescission shape decays into fragments, which are modelled by the *embedded spheroids* introduced in section 2.5. The energy $V_{Cou} + V_{nuc}$ of repulsion between the newborn fragments consists of a Coulomb and a nuclear part.

The Coulomb part is calculated according to

$$V_{Cou} = \frac{e_0^2 Z(Z_{cn} - Z)}{l} S(x_1, x_2) , \tag{4.10}$$

where $e_0^2 \approx 1.44$ MeV fm is the square of the elementary charge. The charge numbers Z and $Z_{cn} - Z$ of the fragments are calculated from the mass numbers A and $A_{cn} - A$ by a search for the minimum potential energy of the postscission configuration. They can also be obtained, with sufficient accuracy, from the assumption that the charge density is constant everywhere in the scissioning nucleus. The factor $S(x_1, x_2)$ contains the correction due to the spheroidal deformations. It is calculated according to [4.3],

$$S(x_1, x_2) = \sum_{m=0}^{\infty} \sum_{n=0}^{\infty} \frac{3}{(2m+1)(2m+3)} \frac{3}{(2n+1)(2n+3)} \frac{(2m+2n)!}{2m!2n!} x_1^{2m} x_2^{2n} . \tag{4.11}$$

The quantities x_i are related to the eccentricities ε_i of the fragments by

$$x_i = \frac{a_i \varepsilon_i}{l} , \quad \varepsilon_i = \left[1 - \left(\frac{b_i}{a_i}\right)^2\right]^{1/2} . \tag{4.12}$$

The semiaxes a_i and b_i are defined in (2.26) and (2.27), respectively. The expansion (4.11) is numerically more convenient than the closed form [4.4].

The nuclear interaction energy V_{nuc} between the nascent fragments is evaluated using a proximity formula

$$V_{nuc} = 4\pi\gamma_0 \phi(0) \frac{b_1^2 b_2^2}{a_1 b_2^2 + a_2 b_1^2} . \tag{4.13}$$

The b_i^2/a_i are the curvature radii at the tips of the spheroids, and $\phi(0) = -1.7817$ fm is the value of the proximity potential function [4.5] for zero distance between the surfaces.

To obtain, at last, a measurable average total kinetic energy, one uses

$$\overline{\mathrm{TKE}}(A) = V_{\mathrm{Cou}} + V_{\mathrm{nuc}} + K_{\mathrm{s}} . \tag{4.14}$$

Our results (see sections 5.2, 7.2 and 7.3) are consistent with the assumption that the prescission kinetic energy K_{s} is of the order of 10 MeV; it seems smaller in low-energy fission, but might be somewhat larger in cases where fission must be enforced by high excitation. Therefore, eqs. (4.10) and (4.13) suffice to find $\overline{\mathrm{TKE}}(A)$. Averages over mass numbers are obtained by summing with the weight (4.8).

4.5. The neutron multiplicity $\bar{\nu}(A)$

The available energy in the newborn fragments is

$$E^*(A) = E_{\mathrm{def}}(A) + E_{\mathrm{s}}^* A/A_{\mathrm{cn}} . \tag{4.15}$$

$E_{\mathrm{def}}(A)$ denotes the deformation energy of the fragment with mass number A, and the last term in eq. (4.15) is the share of the thermal energy that the fragment receives according to equipartition.

The prescission excitation energy E_{s}^* is the same that enters the prescission temperature T. See the remarks that follow eq. (4.8).

To establish the function $E_{\mathrm{def}}(A)$, one goes back to the *embedded spheroids* (section 2.5) and has hence to know the potential energy of a spheroidally deformed fragment:

$$E_{\mathrm{def}}(\varepsilon) = E_{\mathrm{sur}}^{\mathrm{sph}}(A)\left\{ \frac{\arcsin\varepsilon + \varepsilon(1-\varepsilon^2)^{1/2}}{2\varepsilon(1-\varepsilon^2)^{1/6}} - 1 + 2x\left[\frac{(1-\varepsilon^2)^{1/3}}{2\varepsilon} \ln\left(\frac{1+\varepsilon}{1-\varepsilon}\right) - 1 \right] \right\} . \tag{4.16}$$

The fissility x is defined by

$$x = E_{\mathrm{Cou}}^{\mathrm{sph}}(A)/2E_{\mathrm{sur}}^{\mathrm{sph}}(A) , \tag{4.17}$$

and the eccentricity ε was introduced in eq. (4.12). $E_{\mathrm{sur}}^{\mathrm{sph}}(A)$ and $E_{\mathrm{Cou}}^{\mathrm{sph}}(A)$ denote the surface and Coulomb energies of a spherical nucleus. For their calculation we have strictly adhered to the prescriptions given in [4.1, 4.2], in particular to the much too large radius constant $r_0 = 1.2249$ fm.

As we now know the excitation energy $E^*(A)$ of a newborn fragment, we can calculate the neutron multiplicities $\bar{\nu}(A)$ from the implicit equation

$$E^*(A) = \sum_{n=1}^{\bar{\nu}(A)} (S_n + \eta_n) + E_\gamma . \tag{4.18}$$

The separation energy S_n of the neutrons may be taken from some mass formula, for example [4.1, 4.2], or from atomic mass tables [4.6]. The average kinetic energy η_n of the neutrons is $\frac{3}{2}$ times the temperature of the fragment, which in turn can be calculated from the excitation energy (4.15). Finally, the residual energy E_γ that the γ-rays carry off is about half the separation energy $S_{\bar{\nu}(A)+1}$ of the first

non-evaporated neutron. For most purposes

$$\bar{\nu}(A) = \frac{E^*(A)/\mathrm{MeV}}{8} \tag{4.19}$$

is good enough.

It must be stressed that the last two equations are not valid in high energy fission where excitation is sufficient for the evaporation of charged particles. There one must use evaporation codes and compare the excitation energies (4.15) rather than neutron multiplicities.

5. Evidence for random neck rupture

5.1. Rupture and randomness

The instabilities mentioned in section 3.2 are all based on continuum mechanics. It is not clear from the beginning that these mechanisms also apply to quantum objects such as nuclei. But there is evidence for the shift and capillarity instabilities in nuclear fission. To recall, the capillarity instability creates rupture, while randomness is activated by the shift instability. Though it is not possible to isolate the effects from these two mechanisms perfectly, one may group certain experimental results as pertaining more to one instability than to the other. Thus the data presented in sections 5.2 and 5.3 mainly reflect the mere rupture, whereas those in the sections 5.4, 5.5, 5.6 and 5.7 correspond rather to randomness.

5.2. The extended systematics of the total kinetic energy

Averaging over the mass numbers A makes from the function $\overline{\mathrm{TKE}}(A)$ a number, the average total kinetic energy $\overline{\mathrm{TKE}}$. One of the great achievements of nuclear fission research is Viola's systematics [5.1], namely $\overline{\mathrm{TKE}} \propto Z_{\mathrm{cn}}^2/A_{\mathrm{cn}}^{1/3}$ for nearly all the known compound nuclei. At first this scaling seems to be trivial, but at a second view it turns out to be surprising.

Namely the only serious contributor to $\overline{\mathrm{TKE}}$ is the Coulomb energy (4.10), and in V_{Cou} only the factor $Z(Z_{\mathrm{cn}} - Z)/l$ varies significantly. $Z(Z_{\mathrm{cn}} - Z)$ averaged, on the other hand, is proportional to Z_{cn}^2. Yet it is odd that the distance l goes just as $A_{\mathrm{cn}}^{1/3}$ and does not depend on Z_{cn}. Barriers, for example, depend crucially on the charge, and therefore one should expect that the scissioning shapes just before acceleration also look different for different total charges.

Equation (3.3), that is the Rayleigh instability, solves this problem. In geometrical terms, eq. (3.3) conveys that all the linear dimensions of the prescission shape scale with $A_{\mathrm{cn}}^{1/3}$. Approximate the prescission shape by a cylinder. We then have by volume conservation $2\pi r^2 l \propto A_{\mathrm{cn}}$ and because of (3.3) $l \propto A_{\mathrm{cn}}^{1/3}$ and $r \propto A_{\mathrm{cn}}^{1/3}$. The reason for the simple scaling is, of course, that the capillarity instability is conditioned exclusively by surface tension, as pointed out in section 3.4.

One may derive more than proportionality. The argument discussed in the previous paragraph for the finite cylinder yields $l/r_{\mathrm{cn}} = 2.7$. Realistic shapes can store a part of their mass in the heads. Therefore both neck radius and length are somewhat smaller than for the cylindrical case. From fig. 2.2 one can see that

$$l = 2.4 r_{\mathrm{cn}} . \tag{5.1}$$

If symmetric scission is presumed, we may compute the semiaxes of the embedded spheroids by (2.26) and (2.27), find the x_i and ε_i by (4.12), and have then from (4.10)

$$V_{\mathrm{Cou}}/\mathrm{MeV} = \frac{1.44 Z_{\mathrm{cn}}^2 S(0.42, 0.42)}{4 \times 2.4 r_0 A_{\mathrm{cn}}^{1/3}} \tag{5.2}$$

for the Coulomb repulsion and from (4.13)

$$V_{\mathrm{nuc}}/\mathrm{MeV} = 4\pi\gamma_0\phi(0) \times 2.4^{-2} r_0 A_{\mathrm{cn}}^{1/3} \tag{5.3}$$

for the nuclear attraction. With r_0 from (4.1), γ_0 from (4.2), $S(0.42, 0.42)$ from (4.11) and $\phi(0)$ after (4.13) we can add (5.2) and (5.3) according to (4.14) and find

$$\overline{\mathrm{TKE}}/\mathrm{MeV} = 0.14 Z_{\mathrm{cn}}^2/A_{\mathrm{cn}}^{1/3} - 4A_{\mathrm{cn}}^{1/3} . \tag{5.4}$$

Since, crudely, $Z_{\mathrm{cn}} \propto A_{\mathrm{cn}}$, the dependence of the second term on mass is weak in comparison with that of the first. Therefore, we used

$$\overline{\mathrm{TKE}}/\mathrm{MeV} = 0.14 Z_{\mathrm{cn}}^2/A_{\mathrm{cn}}^{1/3} - 30 , \tag{5.5}$$

which is accurate for heavy nuclei ($250 < A_{\mathrm{cn}} \leq 476$) [3.13]. For lighter nuclei, deviations show up, see fig. 5.1. There it is perceptible that the nuclear attraction decreases with decreasing mass, as predicted by eq. (5.4). However, the important feature in (5.4) and (5.5) is the minus sign for the last term. This

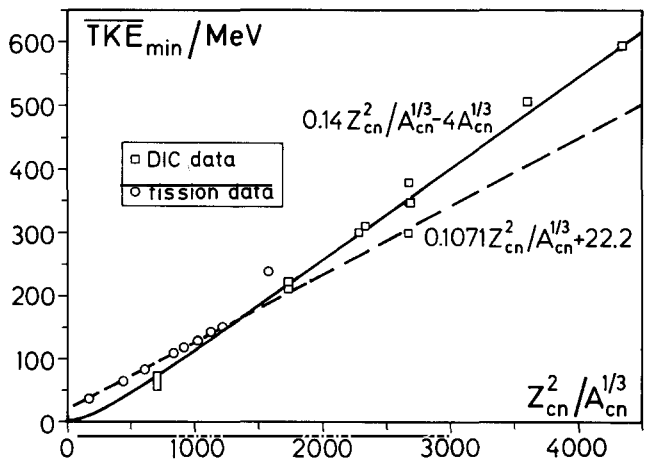

Fig. 5.1. Generalized systematics of total kinetic energy. A similar graph was presented first in [3.13]. The thick line displays the theoretical result (5.4), which is not a pure function of $Z_{\mathrm{cn}}^2/A_{\mathrm{cn}}^{1/3}$. The missing dependence in the last term was taken from the valley of β-stability. The term $-4A_{\mathrm{cn}}^{1/3}$ differs from -30 sizeably only for $Z_{\mathrm{cn}}^2/A_{\mathrm{cn}}^{1/3} < 1000$. Therefore eq. (5.5) is also well represented by the thick line. The broken line is from Viola's pioneering work [5.1]. Total kinetic energies are denoted here by $\overline{\mathrm{TKE}}_{\mathrm{min}}$ to comply with the requirements from *deep inelastic collisions* (DIC). $\overline{\mathrm{TKE}}_{\mathrm{min}}$ is the smallest total kinetic energy measured in deep-inelastic reactions, while it coincides with the usual $\overline{\mathrm{TKE}}$ in fission. In DIC, very asymmetric fragment pairs can be produced. One has to multiply the measured value of $\overline{\mathrm{TKE}}_{\mathrm{min}}$ by $Z_{\mathrm{cn}}^2/[4\bar{Z}(Z_{\mathrm{cn}} - \bar{Z})]$, if $\bar{Z}$ denotes the average charge number of the lighter fragments, before it is entered into this graph. This is to correct for the different Coulomb repulsion of the two unequal charges instead of the symmetric scission presumed in the derivation of eq. (5.4).

means that nuclear forces cause an *attraction*. The sign is therefore not free for disposition. In fact, recent evaluations [5.2] of fission data show that Viola's original positive constant +22.2 is too large.

Evidence for scaling laws is usually considered valid only if the scaling parameters vary over at least one order of magnitude. Even today this cannot be attained from fission data alone. But when deep-inelastic data are included, the range is exploded by a factor of three, see fig. 5.1. The evidence for the random neck rupture result (5.4) is all the more convincing as it reproduces not only the exponents but also the absolute values.

In eqs. (5.4) and (5.5) mass fluctuations are not taken into account. But one can do this with the random-neck-rupture program described in ch. 4. To this end one takes the average mass $\bar{A}$ from experiment and enters according to eq. (5.1) $l/\mathrm{fm} = 2.4 r_0 A_{\mathrm{cn}}^{1/3}$ and $A = \bar{A}$ as first estimates. The program then yields a prediction $\sigma_A^{2\prime}$ which is usually close to the experimental value σ_A^2. To increase perfection, l is modified until the primed quantity coincides with the bare one. Such "individual" predictions of $\overline{\mathrm{TKE}}$ are presented in tables 5.1 and 5.2.

Table 5.1

Total kinetic energies from theory ($\overline{\mathrm{TKE}}^{\mathrm{t}}$) and experiment ($\overline{\mathrm{TKE}}^{\mathrm{e}}$) for common fission. The first column describes the reaction by which fission was induced. Consider, for example, the first reaction: protons with 1000 MeV kinetic energy in the laboratory were a nickel target; then, on the average, three protons and six neutrons escaped before an iron nucleus fissioned. The variances σ_A^2 of the mass distributions come from the measurements. They were reproduced by random neck rupture and served as a basis for the computation of ($\overline{\mathrm{TKE}}^{\mathrm{t}}$), as explained in section 5.2. The question marks in the fourth and fifth lines indicate that these values had to be estimated. However, even a mistake by 50% would not change the ($\overline{\mathrm{TKE}}^{\mathrm{t}}$) by more than 10 MeV. For ^{258}Fm(sf) only the so-called high energy or supershort component was taken into account, cf. section 7.2. Some error estimates of the experimental data, which are given with the customary ± symbols, should convey an idea of the accuracy of such measurements. Due to the simplifications and inaccuracies discussed in sections 3.5, 4.2 and 4.4, predictions made by random neck rupture cannot be better than 5 MeV

Reaction	$\overline{\mathrm{TKE}}^{\mathrm{t}}$ (MeV)	$\overline{\mathrm{TKE}}^{\mathrm{e}}$ (MeV)	σ_A^2	References
p(1000 MeV) + ^{58}Ni→ 3p + 6n + ^{50}Fe	9	34 ± 4	100	[5.3]
p(600 MeV) + ^{107}Ag→ 3p + 6n + ^{99}Rh	40	65.2 ± 2.5	200	[5.4]
p(600 MeV) + ^{139}La→ 3p + 8n + ^{129}Cs	54	88.6 ± 4.9	550	[5.4]
^{16}O(166 MeV) + ^{141}Pr→ ^{157}Ho	92	115	130(?)	[5.1, 3.12]
^{12}C(125 MeV) + ^{159}Tb→ ^{171}Lu	103	121	130(?)	[5.1, 3.12]
^{12}C(120 MeV) + ^{174}Yb→ ^{186}Os	115	124	199	[5.5, 3.12]
^{12}C(136 MeV) + ^{174}Yb→ ^{186}Os	115	124	211	
^{12}C(151 MeV) + ^{174}Yb→ ^{186}Os	115	128	215	
^{12}C(165 MeV) + ^{174}Yb→ ^{186}Os	114	127 ± 5	235 ± 14	
^{36}Ar(205 MeV) + ^{169}Tm→ n + ^{204}Fr	144	151 ± 8	350	[5.6]
^{16}O(93 MeV) + ^{192}Os→ ^{208}Po	141.4	147.1	135	[5.7, 3.12]
^{16}O(105 MeV) + ^{192}Os→ ^{208}Po	140.9	147.0	154	
^{16}O(106 MeV) + ^{192}Os→ ^{208}Po	140.6	144.4	161	
^{16}O(119 MeV) + ^{192}Os→ ^{208}Po	140.2	146.8	180	
α(40 MeV) + ^{209}Bi→ ^{213}At	144	146	94	[5.5, 3.12]
α(60 MeV) + ^{209}Bi→ ^{213}At	144	147	135	
α(65 MeV) + ^{209}Bi→ ^{213}At	144	150	131	
α(80 MeV) + ^{209}Bi→ ^{213}At	144	148	152	
α(100 MeV) + ^{209}Bi→ ^{213}At	144	150	159	
α(120 MeV) + ^{209}Bi→ ^{213}At	145	152 ± 4	153 ± 7	
^{252}Cf (sf)	186	186 ± 1	43	[5.8, 3.2]
^{258}Fm (sf)	236	232	14	[1.11, 5.9]

Table 5.2
Total kinetic energies from theory ($\overline{\text{TKE}}^{\text{t}}$) and experiment ($\overline{\text{TKE}}^{\text{e}}$) for deep-inelastic reactions. The table is organized as table 5.1. Special features are as follows: the superscripts Z in the fourth column indicate that only charge variances σ_Z^2 were measured. They were converted into mass variances according to eq. (5.6). Another peculiarity is marked by the asterisks. Namely, the experimentalists who measured the reaction ^{92}Mo + ^{92}Mo introduced a novel TKE* quantity [1.5]. It arises from ordinary TKE by removing the $Z(Z_{cn} - Z)$ dependence that occurs in the Coulomb repulsion (4.10). The theoretical quantity was computed with the corresponding modifications

Reaction	$\overline{\text{TKE}}^{\text{t}}$ (MeV)	$\overline{\text{TKE}}^{\text{e}}$ (MeV)	σ_A^2	References
^{36}Ar(270 MeV) + ^{92}Mo	61	61 ± 9	190 ± 40	[5.10, 3.13]
^{40}Ar(270 MeV) + ^{100}Mo	61	54 ± 14	140 ± 40	[5.10, 3.13]
^{92}Mo(1680 MeV) + ^{92}Mo	137*	180 ± 30*	2400	[1.5]
^{86}Kr(515 MeV) + ^{166}Er	193	194	300^Z	[5.11, 5.12, 3.13]
^{86}Kr(703.5 MeV) + ^{166}Er	182	198	675^Z	[5.11, 5.12, 3.13]
^{144}Sm(1000 MeV) + ^{144}Sm	299	313	283 ± 30	[5.13, 5.14, 3.13]
^{154}Sm(970 MeV) + ^{154}Sm	279	298	357 ± 36	[5.13, 5.14, 3.13]
^{136}Xe(940 MeV) + ^{209}Bi	349	326	250 ± 100^Z	[5.15, 3.13]
^{136}Xe(1130 MeV) + ^{209}Bi	335	363	510 ± 50^Z	[5.16, 3.13]
^{136}Xe(1420 MeV) + ^{209}Bi	322	286	960 ± 100^Z	[5.17, 3.13]
^{208}Pb(1575 MeV) + ^{208}Pb	508	503	230^Z	[5.18, 3.13]
^{238}U(1766 MeV) + ^{238}U	592	593	550^Z	[5.19, 3.13]

Evidently, random neck rupture gives accurate predictions for ordinary fission (see ^{252}Cf in table 5.1), reasonable ones for the heavy systems (table 5.2), but only moderate results for the fission of very light nuclei (table 5.1). However, relative to the range of about 600 MeV the deviations are not larger than 5%.

Concerning the dependence of $\overline{\text{TKE}}$ on the energy of the incident particle, one can only say that it is very weak both in experiment and theory, cf. Table 5.1.

Most reactions cited in the tables import a great deal of excitation energy into the scissioning nuclei. Just because of that they were selected. Namely, in such reactions quantum shells are smeared out so that random neck rupture with its concepts from continuum mechanics should be valid. Two exceptions are the spontaneous fissions of californium and fermium. These examples suggest that random neck rupture might also be useful when quantum effects are present. This will be exploited widely in chs. 7 to 9.

For fission of astatine and similar nuclei excellent data have become available recently [5.20]. They confirm the conclusions that can be drawn from the materials presented here.

5.3. The neck recollects asymmetry

One of the central problems of deep-inelastic heavy-ion reactions was the *invariability of the average mass*. If, for example, a ^{132}Xe projectile was fired at ^{209}Bi, then, *on the average*, a fragment with mass number of about 132 came out, in spite of giant mass fluctuations. This invariability was a miracle until it was shown by eqs. (4.6), (4.7) that it is a property of neck rupture: *the nucleons that projectile and target contribute to the common neck are on the average returned to the fragments*. At present no one knows the true contribution policy, but the independence of the results on the parameter μ shows that this does not matter. For instance, if the projectile contributes many nucleons it pushes the smallest

diameter of the neck far away. Therefore, at rupture a large part of the neck goes back to the former projectile. If the projectile contributes less, it also receives less at scission. In this way the neck acts as a memory.

One of the few discriminators between deep-inelastic collisions (DIC) and fission is hence the average mass number of the fragments. For fission, the reaction goes through a true compound state. Memory of initial asymmetry is lost there so that the average mass number of the fragments appears at mass symmetry, provided shell effects do not interfere. For DIC, a compound state is never reached. Target and projectile just touch to make a neck, although a massive one. The initial asymmetry is thus preserved on the average.

Discrimination between DIC and fission becomes uncertain for $A_{cn} \approx 260$. In such systems compound nuclei are very unstable, in particular if they are excited. Therefore, a smooth transition from DIC to fission is observed. The phenomenon was investigated with much care (see, e.g., [5.11] and [6.22]), but it is not typical for DIC. If $A_{cn} < 230$ and the projectile mass differs from that of the target, fission fragments can be separated from DIC products. For $A_{cn} > 300$ fission fragments do not exist since Coulomb forces prohibit a compound state.

These relations are illustrated in fig. 5.2. In three of the four cases it demonstrates the invariability of the averages in spite of increasing variances, according to measurements and according to random neck rupture. The Ar + Mo and Kr + La systems are below $A_{cn} = 230$, Xe + Bi is above $A_{cn} = 300$ and only Kr + Er is in the mixing zone. Therefore, it is understandable that the random-neck-rupture calculations that were made for pure DIC gave fair results in all cases except for Ke + Er.

To judge the quality of the predictions due to random neck rupture, one has to look for the achievements of the most successful competitor. This competitor is the *diffusion or transport model*, several versions of which have been developed in the past, see, e.g., [5.22] and [5.23]. Diffusion models describe the approach to that equilibrium to which scission point models such as [1.4] are limited. Diffusion models are hence extrapolations of equilibrium theories, without a qualitative change of the physical ingredients. Typical results of diffusion calculations are shown in fig. 5.2 by the dotted lines. The crux with the diffusion models is that they cannot attain the large measured variances even when they are tuned to do so. But most striking is the invincible drift to symmetry at the larger variances. Even for the mixed Kr + Er system the random-neck-rupture prediction is better than that of the diffusion model. Details can be found in [3.13, 3.14].

The merits of random neck rupture are limited here to reproduce the correct *correlation* between variance and average. The variances were not determined independently. In order to learn how the bold lines in fig. 5.2 were computed, you might wish to reread section 4.2, in particular the final part. There it was stated that the prescission shape has only two degrees of freedom: its semilength l and its asymmetry, expressed by the mass number A_P of the projectile. While A_P was given immediately, we had to derive the length l from the mass variance σ_A^2 or, when this was not available, from the charge variance σ_Z^2 via

$$\sigma_A^2 \approx (A_{cn}/Z_{cn})^2 \sigma_Z^2 . \tag{5.6}$$

The mass distribution and hence also *the average mass number of the fragments* were then obtained from the rupture probability (4.8). If you want the average charge number $\bar{Z}$ of the fragments, this can be obtained from

$$\bar{Z} = (Z_{cn}/A_{cn})\bar{A} \tag{5.7}$$

or from the minimum-potential-energy approach described in section 4.4.

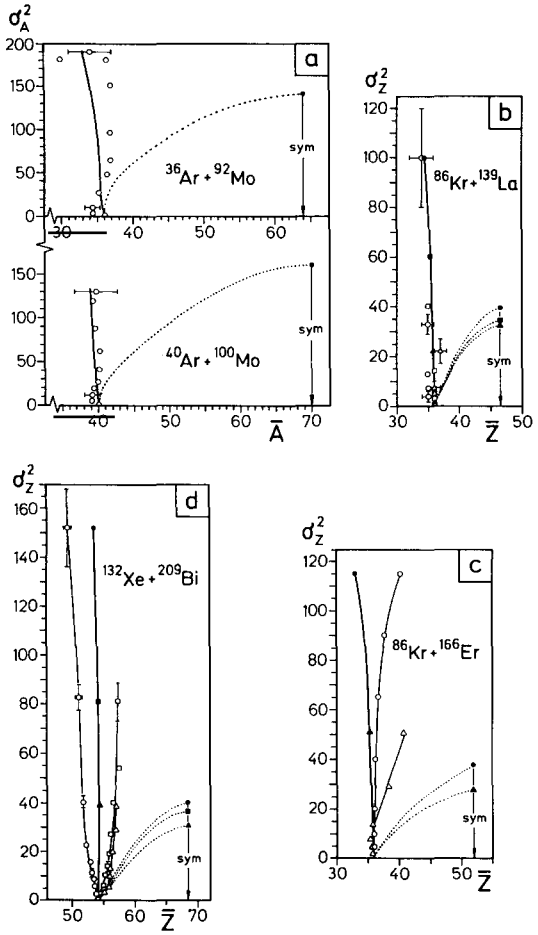

Fig. 5.2. Correlations between averages and variances of the fragment mass distributions in several heavy-ion reactions. In all the parts, the experimental data are distinguished by open symbols and partly by error bars. Thick or dotted lines depict the theoretical results. The thick lines are predictions of random neck rupture calculations, the dotted lines are output of a diffusion code. The thin lines in parts (c) and (d) connect the experimental data to make the trends more obvious. Mass symmetry is pointed out by the arrows. Actually in parts (b)–(d) the mass quantities are replaced by charge observables, but because of equations (5.6)–(5.7) conversion is so straightforward that all the graphs convey essentially the same information. Part (b) contains data from three experiments, namely lanthanum bombarded by krypton at 505 MeV (triangles), 610 keV (squares), and 710 MeV laboratory energy (circles). Part (c) displays two sets, krypton at incident energies of 515 MeV (triangles) and 703.5 MeV (circles). Part (d) again shelters three experiments, xenon at 970 MeV (triangles), 1130 MeV (squares), and 1420 MeV (circles). The theoretical curves are terminated with corresponding symbols to indicate to which experiment they belong. The experimental data were taken from [5.10], [5.21], [5.11, 5.12] and [5.15–5.17], respectively. The theoretical data were shown first in [3.13] and [3.14].

Hence the neck can make large mass variances without changing the average mass. For DIC this is a physically important discovery.

5.4. The neck generates mass fluctuations

The huge discrepancy between measured mass variances and those calculated using diffusion models was the reason for us to develop random neck rupture. In fission, the same discrepancies were known long ago, but since they were factor-2 errors, they were disregarded. For example, in table 5.1 the value

of σ_A^2 observed in the fission of ^{204}Fr is about 1.5 times too large for an equilibrium theory [5.6]. More or less the same is true for the σ_A^2 of ^{252}Cf(sf) [1.4]. In addition, a dynamical model [2.3] that includes more than equilibrium fluctuations had problems when it was compared with the α + Bi data shown in table 5.1. However, these two were only factor-2 errors so that one could hope to cure the disease by quantitative improvements. But some deep–inelastic reactions exhibited fluctuations that were an order of magnitude beyond the predictions of diffusion theories. Among these are the reactions Xe(1420 MeV) + Bi and Mo(1680 MeV) + Mo, see table 5.2. Also figs. 5.2b, c, d visualize the discrepancies between the observed variances and the values calculated with diffusion theory even if the drift to mass symmetry is disregarded.

The reason for the mass fluctuations being too small is discussed at length in [5.23]. The arguments developed there can be summarized as follows: if two nascent fragments are bridged by a thin neck, it costs much binding energy to create an asymmetric configuration. Thermal or quantal fluctuations cannot spread against this confinement. What actually happens is described in section 3.3: asymmetry is generated when the neck is still thick and the shift of the dent takes essentially no energy; later on, when the potential energy would like to restore symmetry, it is blocked by inertia. This latter fact establishes the invariability of the average mass, as discussed in the previous section.

For the theoretical $\overline{\text{TKE}}$s presented in the tables 5.1 and 5.2, the experimental σ_A^2 were used. Hence agreement between measured and theoretical variances cannot be celebrated as a success. Nevertheless it must be stressed that *random neck rupture can account for the largest variances ever measured*, see the σ_A^2 of the Mo + Mo reaction in table 5.2. In fact, the largest variance random neck rupture can give is about $A_{\text{cn}}^2/12$.

5.5. *Narrow mass distributions imply high $\overline{TKE}$ and vice versa*

One of the significant correlations which random neck rupture gives is that large total kinetic energies $\overline{\text{TKE}}$ must come with small mass variances σ_A^2. This anticorrelation was already announced in item (i) of section 3.1 and is made comprehensible by figs. 3.1a, b. Ample evidence exists for it.

For example, consider the two outliers in the total kinetic energy systematics (see fig. 5.1). One of them sits at $Z_{\text{cn}}^2/A_{\text{cn}}^{1/3} = 1571$ and belongs to ^{258}Fm(sf). The other at $Z_{\text{cn}}^2/A_{\text{cn}}^{1/3} = 3603$ stems from the deep-inelastic collision ^{208}Pb(1575 MeV) + ^{208}Pb and deviates not that much from the full line. When these reactions with their unusually high $\overline{\text{TKE}}$s are looked up in the tables 5.1 and 5.2, one finds for them unusually small values of σ_A^2. Reactions for comparison are ^{252}Cf(sf) and ^{238}U(1766 MeV) + ^{238}U.

Even more striking are recent data on the heaviest actinides shown in fig. 5.3. These nuclei fission through two different fission channels, as will be discussed in detail in sections 7.2 and 8.3. What only matters here is that the relative yields change abruptly. For example, spontaneous fission of ^{259}Md preferentially produces fragments with low $\overline{\text{TKE}}$, and the corresponding mass distribution is broad. ^{260}Md, on the other hand, is rather active at high $\overline{\text{TKE}}$, and thus the mass distribution is narrow.

All the data presented by Hulet and co-workers [1.11] exhibits the same anticorrelation. Similar evidence can be found in sections 7.2 and 8.4, where the meaning of the superlong fission channels and of the standard I/II splitting will be discussed. At present no exception from the rule expressed by the title of this section is known.

Narrow mass distributions indicate a short neck. Random neck rupture cannot clarify why short necks are formed in just ^{258}Fm(sf) and ^{208}Pb(1575 MeV) + ^{208}Pb. This is the aim of the fission channel calculations to be discussed in the chs. 7, 8 and 9. Anticipating these, we remark here that the short

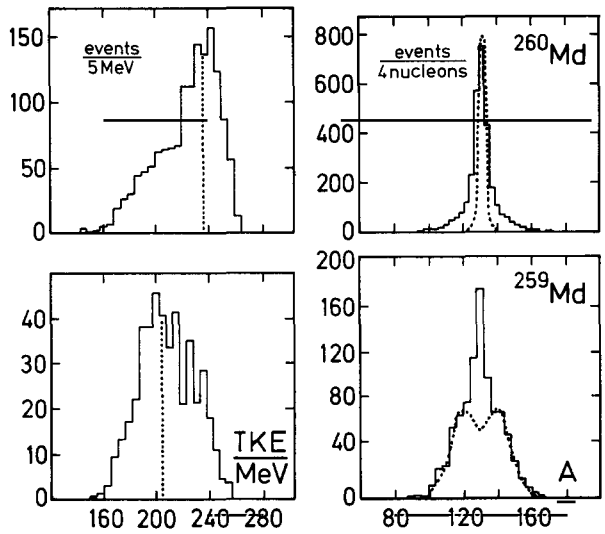

Fig. 5.3. Mass distributions (right-hand side) and total kinetic energy distributions (left-hand side) from the spontaneous fission of ^{259}Md (lower parts) and ^{260}Md (upper parts). The histograms display the experimental results by Hulet et al. [1.11]. Also the normalization was taken from the experimental work, namely in terms of fission events collected in 5 MeV bins for TKE and in four-nucleon bins for mass number A. The dotted lines are predictions of random neck rupture and multichannel-fission calculations, which will be discussed in more detail in chs. 7 to 9. Only those components are shown that are dominant in the respective fissioning system. In ^{259}Md this is the "standard" channel with low kinetic energy and a broad, slightly asymmetrical mass distribution. The "supershort" channel prevails in ^{260}Md with a high average kinetic energy and a narrow mass distribution. The superposition of both components would accurately reproduce the experimental results.

necks have something to do with the closed shells near $Z = 50$, $N = 82$ and $Z = 82$, $N = 126$, respectively, that arise in the stretched compound nucleus prior to scission.

5.6. The slopes of neutron multiplicities

There are three large sets of scission data, namely total kinetic energies, mass yields and neutron multiplicities. In the previous sections we examined the correlations that random neck rupture establishes between the first two sets. Now we shall report what experiments tell us about the interplay between the mass yields and the neutron multiplicities.

According to random neck rupture, neutron multiplicities contain information on the *variability of the rupture position* and hence on the shift instability. In stating this it is assumed that neutron multiplicities reflect the excitation energies of the fragments as described in the most primitive way by eq. (4.19). Excitation energies, on the other hand, depend on the deformations of the newborn fragments as expressed by eq. (4.15). The first term on the right-hand side of (4.15), $E_{\mathrm{def}}(A)$, which is caused by a non-equilibrium process, generates a much steeper dependence on the mass number A than the second term $E_{\mathrm{s}}^{*}A/A_{\mathrm{cn}}$, which is due to statistical equilibrium. This is a prediction that can be checked by experiments.

Figure 5.4 displays such a check. In these data, the experimentalists themselves replaced the neutron multiplicities by excitation energies. One can see that only random neck rupture explains the enormous slopes of $E^{*}(A)$. For more experiments, comparison is summarized in table 5.3.

Data as shown in fig. 5.4 were criticized by other experimentalists as not being reliable. Namely, those data were taken from the kinematics of the fragments; no neutrons were registered. Direct

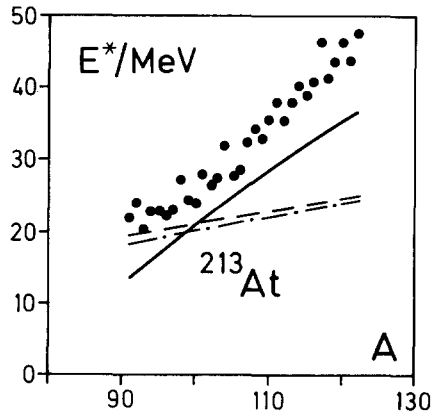

Fig. 5.4. Excitation energy E^* as a function of the fragment mass number A from fission of ^{213}At [3.12]. The dots are the experimental data obtained by Plasil and his colleagues [5.24]. The full line depicts what random neck rupture gives. The dash-dotted line is according to statistical equilibrium, and the dashed one stems froms Nix's dynamical model [2.3].

Table 5.3

Slopes $d\bar{\nu}/dA$ for several fissioning systems. In these systems, the neutron multiplicities $\bar{\nu}(A)$ look like straight lines, at least in a broad neighborhood of mass symmetry, so that the specification of a uniform slope makes sense. The results are given according to statistical equilibrium, that is that the excitation energy is shared by the fragments in proportion to their mass numbers, according to the dynamical model [2.3], according to random neck rupture, and according to meaasurements. The last column contains references to the experimental works. The measurements with astatine and actinium were similar but not identical, the main difference being that the first measurements, respectively, were done using the kinematical method, while the second ones were performed by direct neutron counting

Nucleus	Equilibrium	Dynamical model	Rupture	Experiment	References
^{203}Po	0.02	0.02	0.06	0.06	[5.25]
^{213}At	0.02	0.02	0.08	0.09	[5.24]
	0.02	0.02	0.08	0.04	[5.26]
^{227}Ac	0.01	0.02	0.09	0.09	[5.27]
	0.01	0.02	0.08	0.05	[5.26]

measurements of the neutrons gave smaller slopes, but slopes still too large to be explained by thermal equilibrium, see table 5.3 for documentation. The last point is comforting for a disciple of random neck rupture.

Both experimental methods have disadvantages: the kinematical method derives a small quantity (the number of evaporated nucleons) from the difference of two large numbers (the mass numbers of a fragment prior to and after evaporation). The direct measurements must take the relation between neutron multiplicity and fragment mass from the angular distribution of the neutrons by deconvolution. A differential method usually steepens dependences while a deconvolution smoothens them out. One might therefore assume that the truth is enclosed by the two methods from above and below.

At the end of section 5.5 we already mentioned that the results derived from random neck rupture do not depend on the way in which a particular neck is created. Hence random neck rupture should also be applicable to deep-inelastic collisions and fusion–fission in heavy-ion reactions. In these reactions, the equilibrium term of (4.15) is much more important, since E^*_s is larger than in low-energy fission. Nevertheless, observable rises of the slopes $d\bar{\nu}/dA$ should still exist. For this there is evidence by

Benton et al. [5.28], see fig. 5.5b, but against this evaluation objections were raised [5.29]. Moreover, recent work by Hinde [5.30] and Rossner [5.6] and their co-workers indicates that neutron-multiplicity slopes should be as small as predicted by statistical equilibrium. Comprehensive studies are necessary.

5.7. The sawtooth of neutron multiplicity

According to random neck rupture, a double-humped mass yield $Y(A)$ is inevitably connected with a sawtooth-shaped neutron multiplicity $\bar{\nu}(A)$. This is a very specific relation, and therefore it was already stressed in item (ii) of section 3.1. A violation would either indicate evaporation of charged particles or gamma rays, or invalidate random neck rupture.

The way in which random neck rupture explains this effect is illustrated in fig. 3.2. One can see that the data are reproduced by the theory with an accuracy of about 1 neutron. Further verifications of this kind can be found in fig. 7.4. So one may claim that in nuclear fission no contradiction to random neck rupture seems to exist.

The double-humped mass distribution reflects an asymmetrical prescission shape. In nuclear fission such a shape is due to the quantal effects. In deep-inelastic collisions the prescission shape preserves the initial asymmetry because of the geometry of the neck, see section 5.3. All that is essential for the yield $Y(A)$ and the multiplicity $\bar{\nu}(A)$ is the mere existence of an asymmetrical prescission shape. Hence also in deep-inelastic collisions a neutron sawtooth should be observable if target and projectile have different mass numbers. This was predicted in [3.14]. Meanwhile two verifications can be presented, see fig. 5.5. More recent data measured by Hinde et al. [5.30] were interpreted as a refutation of that

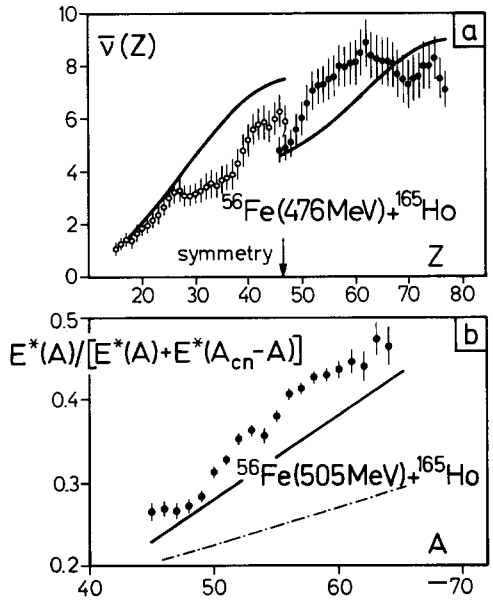

Fig. 5.5. The share of excitation energy that a fragment with mass number A receives when produced in a deep-inelastic reaction. In part (a), the share is expressed by the neutron multiplicity as a function of the fragment's charge number Z. Consult eqs. (4.19) and (5.7) to have these quantities converted into excitation energy and mass number. The measurements were done by Hilscher and co-workers [5.31], and the random-neck-rupture calculation by us [3.1]. Part (b) actually displays the above-mentioned share, but only that piece of the sawtooth shape was measured that is associated with the light fragments [5.28]. The thick line is again the result from random neck rupture while the dash-dotted line represents what one should see if statistical equilibrium prevailed. Note that, according to the data, only 30% of the nucleons get almost 50% of the excitation energy.

prediction, but this is debatable since these data seem to stem from fusion–fission processes (with a symmetrical prescission shape) and to contain very few deep-inelastic events (from an asymmetrical prescission shape).

The scission-point model also succeeded with the sawtooth curve of neutron multiplicity. See fig. 9 in ref. [1.14], where the deformations of the nascent fragments are related to a multiplicity curve. Kluge and Lajtai [5.32] even reached appealing quantitative agreement with uranium, plutonium and californium data. But all these calculations are based on statistical equilibrium. It therefore seems impossible that they can cope with the slopes presented in table 5.3.

6. Fluctuations in the elongation

6.1. A difficulty with the TKE distributions

In nuclear fission, fluctuations of the total kinetic energy are almost as impressive as those of the mass of the fragments. TKE fluctuations can be caused either by varying semilength l of the prescission shape or by changes in the prescission kinetic energy K_s. Furthermore, it is not obvious if these fluctuations are generated, say, on the saddle and are only propagated to scission or if they are built up all along fission by stochastic interactions. That such questions can be tackled by a Langevin equation or, equivalently, by the corresponding Fokker–Planck equation, has been exploited more than once [6.1–6.11].

Moreover, Fokker–Planck equations have also been used to compute the mass distribution of fission. Such approaches are not principally in contradiction to the ideas presented in the previous three chapters. Namely, when a criticism is raised against a certain statistical theory then it is rarely against the use of a Fokker–Planck equation but rather against the underlying physical picture that is modelled by the particular Fokker–Planck equation. A successful application of a Fokker–Planck equation to nuclear fission in a spirit similar to that described in ch. 3 was published by Adeev and Gonchar [6.12]. They mimicked the capillarity instability by stopping their calculations when the nucleus had reached its prescission shape and evaluated the observables from the prescission shape.

Fokker–Planck equations also seem well suited if mass and TKE fluctuations are to be studied in a unified way [6.10]. So this kind of theory is probably ideal to cope with all these complexities.

However, TKE fluctuations pose an especially tough problem. The problem is connected with the long-known *dissymmetry* or *skewness* of the TKE distributions, which is zero in most treatments but sizeable in nature.

The underlying difficulty is much more serious than the appearance of an unwanted third moment. Namely, a recent analysis [6.13] of the experimental data with very good statistics showed that the TKE distributions $Y(\mathrm{TKE})$ for fixed mass number A are well described by

$$Y(\mathrm{TKE}) = \left(\frac{200}{\mathrm{TKE}}\right)^2 h \exp\left(\frac{-(L - l_{\max})^2}{(L - l_{\min}) l_{\mathrm{dec}}}\right). \tag{6.1}$$

On the right-hand side

$$L := \frac{e_0^2 Z(Z_{\mathrm{cn}} - Z)}{\mathrm{TKE}} \tag{6.2}$$

is a replacement for TKE. If one drops all sophisticated details such as fragment deformation and nuclear interaction, one may interpret L as the semilength of the prescission shape; compare (6.2) with eqs. (4.10) and (4.14). The fit parameters

$$h,\ l_{\min},\ l_{\max},\ l_{\mathrm{dec}} \tag{6.3}$$

have intuitive meanings. h approximates the height of the distribution because 200 MeV is about the average $\overline{\mathrm{TKE}}$ of the fission of the actinides (see the factor $(200/\mathrm{TKE})^2$ in front of the right-hand side). The distribution is zero for all L smaller than $l_{\min}$. $l_{\min}$ hence denotes the smallest semilength possible. $l_{\max}$ is the length for which the exponential is largest and l_{dec} gives the scale for the decrease with increasing L. One of the excellent fits that were made possible by the function (6.1) can be admired in fig. 6.1. Similar agreement was reached for the neutron-induced fission of uranium ^{235}U(n, f) whenever there were enough counts and no dominant superposition from different fission channels. So there is not much doubt that (6.1) *is the representation of the TKE distributions.*

Alarming in (6.1) is the odd behavior at large and small TKE, which are outside the reach of all currently available Fokker–Planck theories.

It is therefore clear that the standard approaches miss an essential point in the mechanism generating the TKE distributions. Nevertheless, just for calibration it is useful to have some simple formulas in order to estimate what the conventional theory of stochastic processes would predict. These simple formulas will be derived in the next sections.

6.2. *Exposition: the Langevin process of stretching*

In section 4.4 we learned to obtain the total kinetic energy $\overline{\mathrm{TKE}}(A)$. Its average over A, $\overline{\mathrm{TKE}}$ without argument, contains almost the same information as the function $\overline{\mathrm{TKE}}(A)$ since the dependence

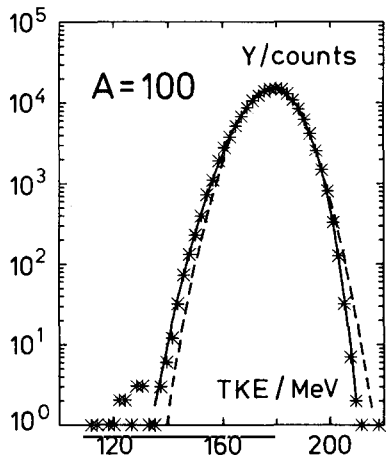

Fig. 6.1. Typical distribution of total kinetic energy Y(TKE) if the mass of a fragment is fixed ($A = 100$ in the present case). The data, displayed by asterisks, were taken from the spontaneous fission of ^{252}Cf [6.14]. The yield is not normalized but given directly by counts to make the quality of the statistics explicit. The line drawn is the best fit based on the function (6.1). It fits perfectly over four orders of magnitude. The dashed line shows the best adaption of the Gaussian $h \exp\{-0.5[(\mathrm{TKE} - \overline{\mathrm{TKE}})/\sigma_E]^2\}$ with h, $\overline{\mathrm{TKE}}$ and σ_E as adjustable parameters. Discrepancies show up when more than one order of magnitude is to be represented. For later reference we declare here that the mass number $A = 100$ was chosen because it is nearly a sheer product of the so-called standard II fission channel.

on A is generated by the trivial factor $Z(Z_{cn} - Z)$ in the Coulomb repulsion energy. This is why we could assign a single semilength to each prescission shape. Nevertheless, the semilength of the prescission shape must fluctuate due to the coupling with the microscopic degrees of freedom. Consequently the total kinetic energy fluctuates even if only a certain fragmentation with fixed mass number A is considered. The goal now is to calculate the *variance* σ_E^2 of the total kinetic energy.

Let us keep only the semilength l as the essential degree of freedom. Thus we restrict ourselves to a single equation of motion

$$m\ddot{l}(t) = -m\xi\dot{l}(t) + F + mR(t)\,, \tag{6.4}$$

the standard Langevin equation. To specify the quantities in this equation, we develop the following physical picture [6.11]:

(i) The inertial parameter m, being identical to m_{11} in (3.1), is taken as a constant. Its value is the reduced mass

$$m = m_{nuc}A_{cn}/4 \tag{6.5}$$

of the relative fragment motion. m_{nuc} represents the mass of a nucleon.

(ii) The constant damping ξ describes the energy transfer to microscopic as well as to other collective degrees of freedom. We shall see that only the product ξt_s matters, where t_s denotes the time that the nucleus spends on its way from the last barrier to scission. The product ξt_s can be obtained from the fraction $K_s/\Delta U$, see (vi) below.

(iii) The force F is also taken to be constant. We obtain it from calculated values of the potential energy by

$$F = \Delta U/\Delta l\,. \tag{6.6}$$

Δl gives the increase of semilength between the last barrier and scission. ΔU is, up to a sign, the potential energy that is freed on descent. For it, the following formula applies:

$$\Delta U = \begin{cases} E_{des} + E_{inp} & \text{if } E_{inp} < B\,, \\ E_{des} + B & \text{otherwise}\,, \end{cases} \tag{6.7}$$

with E_{des} being the difference of potential energy between the prescission shape and the ground state. B denotes the height of the barrier and the input energy E_{inp} is fixed by experimental conditions. Formula (6.7) has to be complicated since it must cope with low-energy fission, see section 8.2, and deep-inelastic collisions, see section 6.4. In spontaneous fission, for example, E_{inp} is zero, and then it is clear that the nucleus cannot gain more energy than $\Delta U = E_{des}$. In heavy-ion collisions E_{inp} is essentially identical with the energy loss E_{loss}, usually a large amount of energy. Nevertheless, ΔU can never become bigger than $E_{des} + B$.

(iv) The random Langevin force $R(t)$ has zero mean, is δ-correlated in time and of constant strength D:

$$\langle R(t)\rangle = 0\,, \tag{6.8}$$

$$\langle R(t)R(t')\rangle = D\delta(t - t')\,, \tag{6.9}$$

wherein the diffusivity D is related to the damping ξ and the temperature T through Einstein's relation

$$D = 2T\xi/m\,. \tag{6.10}$$

This means that the nucleus is permanently subjected to random forces. The origin of these forces is supposed to be thermal; specific quantum fluctuations are neglected because tunneling is not considered.

(v) The temperature T is related to the excitation energy E_s^* by the familiar formula

$$T/\mathrm{MeV} = [8(E_s^*/\mathrm{MeV})A_{cn}^{-1}]^{1/2}\,. \tag{6.11}$$

(vi) In reality, the excitation energy increases from saddle to scission. We take its value E_s^* at scission and fix it according to the following recipe: the gain in energy due to the descent from the last barrier is partly transformed to kinetic energy

$$K_s = \phi(x)\,\Delta U\,, \tag{6.12}$$

partly dissipated

$$E_s^* = \begin{cases} \phi(x)\,\Delta U & \text{if } E_{inp} < B \\ \phi(x)\,\Delta U + E_{inp} - B & \text{otherwise}\,. \end{cases} \tag{6.13}$$

The first contributions on the right-hand sides represent the excitation caused by friction on the way from barrier to scission. Only a fraction of ΔU is transformed to excitation. $\phi(x)$ allots this share. For the moment we just have to know that $\phi(x)$ takes only two values

$$\phi(x) = \begin{cases} \frac{3}{8} & \text{if } A_{cn} < 250 \\ \frac{1}{4} & \text{otherwise}\,. \end{cases} \tag{6.14}$$

The function $\phi(x)$ will be defined in (6.25), and the assignment (6.14) is related to the odd–even effects in fission [6.15, 6.16]. The contribution $E_{inp} - B$ in (6.13) is the residual excitation inherited from the compound state.

All the remainder of ΔU, which is not absorbed by K_s or E_s^*, has to go into collective degrees of freedom other than elongation.

One can develop the subsequent theory from the Langevin eq. (6.4) alone, and this is what we shall do. Just for reference we give the corresponding Fokker–Planck equation

$$\partial_t \rho(l, v, t) = [-v\partial_l - \partial_v(-\xi v + F/m) + (D/2)\partial_v^2]\rho(l, v, t)\,. \tag{6.15}$$

Semilength l and velocity v $(=\dot{l})$ are the independent variables, and $\rho(l, v, t)$ symbolizes the probability density one is seeking when one works with the Fokker–Planck equation, see the textbooks [6.17–6.19] or more specialized for applications in nuclear physics [6.20, 6.21] and, for the problem at hand, [6.11].

6.3. *Solution: formulas for the TKE variances*

The plan is first to extract the average dynamics from (6.4). The resulting formulas will enable us to

eliminate the vaguely known scission time t_s in favor of the scission length $l(t = t_s)$. With this we can process the variances.

Write the Langevin eq. (6.4) as a first-order system:

$$\begin{pmatrix} \dot{l} \\ \dot{v} \end{pmatrix} = -\boldsymbol{\Lambda}\begin{pmatrix} l \\ v \end{pmatrix} + \begin{pmatrix} 0 \\ F/m + R(t) \end{pmatrix}, \tag{6.16}$$

with the damping matrix

$$\boldsymbol{\Lambda} := \begin{pmatrix} 0 & -1 \\ 0 & \xi \end{pmatrix} \tag{6.17}$$

as an abbreviation. The elementary theory of ordinary differential equations gives the solution of (6.16) as

$$\begin{pmatrix} l(t) \\ v(t) \end{pmatrix} = \mathrm{e}^{-\boldsymbol{\Lambda} t}\begin{pmatrix} l(0) \\ v(0) \end{pmatrix} + \int_0^t \mathrm{e}^{-\boldsymbol{\Lambda}\tau}\begin{pmatrix} 0 \\ F/m + R(t-\tau) \end{pmatrix} \mathrm{d}\tau \,. \tag{6.18}$$

Averaging makes the Langevin force R disappear, cf. eq. (6.8). With

$$\mathrm{e}^{-\boldsymbol{\Lambda} t} = \mathbf{1} - \boldsymbol{\Lambda}\,\frac{1 - \mathrm{e}^{-\xi t}}{\xi}\,, \tag{6.19}$$

you can solve the integrals in (6.18). The mean values come out as

$$\langle l(t)\rangle = \langle l(0)\rangle + \frac{F}{m\xi}\,t + \left(\langle v(0)\rangle - \frac{F}{m\xi}\right)\frac{1 - \mathrm{e}^{-\xi t}}{\xi} \tag{6.20}$$

and

$$\langle v(t)\rangle = \langle v(0)\rangle - \left(\langle v(0)\rangle - \frac{F}{m\xi}\right)(1 - \mathrm{e}^{-\xi t})\,. \tag{6.21}$$

What we look for is the status at scission, hence $t = t_s$. Then we see, it is only the length difference $\Delta l := \langle l(t_s)\rangle - \langle l(0)\rangle$ between the last barrier and the scission point which plays a role. In addition, at least in fission, the velocities must be small on top of the barrier. Therefore, we put $\langle v(0)\rangle = 0$. Hence a condensed version of the eqs. (6.20) and (6.21) is

$$\Delta l = \frac{F}{m\xi^2}\,(x - 1 + \mathrm{e}^{-x})\,, \qquad v_s = \frac{F}{m\xi}\,(1 - \mathrm{e}^{-x})\,, \tag{6.22}$$

with $v_s := \langle v(t_s)\rangle$ and

$$x := \xi t_s\,. \tag{6.23}$$

The first equation in (6.22) shows indeed that one may eliminate the scission time t_s by the length of the descent Δl.

However, one can go one step further. The prescission kinetic energy must be of the order

$$K_s \approx \tfrac{1}{2} m v_s^2 . \tag{6.24}$$

Putting (6.22) with (6.6) into this leads to

$$K_s/\Delta U = \phi(x) , \quad \phi(x) := \frac{1}{2} \frac{(1-e^{-x})^2}{x - 1 + e^{-x}} . \tag{6.25}$$

In words: the fraction $K_s/\Delta U$ of potential energy that turns into kinetic energy fixes the friction parameter x and vice versa. The impellent for the assumption (vi) in the previous section should now be clear.

For the computation of the TKE variance we need the covariance matrix

$$\boldsymbol{\Gamma}(t) := \begin{pmatrix} \Gamma_{ll}(t) & \Gamma_{lv}(t) \\ \Gamma_{lv}(t) & \Gamma_{vv}(t) \end{pmatrix} , \tag{6.26}$$

with the elements

$$\begin{aligned} \Gamma_{ll}(t) &:= \langle (l(t) - \langle l(t) \rangle)^2 \rangle , \\ \Gamma_{lv}(t) &:= \langle (l(t) - \langle l(t) \rangle)(v(t) - \langle v(t) \rangle) \rangle , \\ \Gamma_{vv}(t) &:= \langle (v(t) - \langle v(t) \rangle)^2 \rangle . \end{aligned} \tag{6.27}$$

To find them, one has to subtract from (6.18) the mean value (this removes the term with the constant force F), to square the expression, and to take averages. The term with the square of the Langevin force does not drop out so that (6.9) must be applied. One obtains

$$\boldsymbol{\Gamma}(t) = e^{-\boldsymbol{\Lambda} t} \boldsymbol{\Gamma}(0) e^{-\boldsymbol{\Lambda}^{\mathrm{T}} t} + \int_0^t e^{-\boldsymbol{\Lambda} \tau} \boldsymbol{D} e^{-\boldsymbol{\Lambda}^{\mathrm{T}} \tau} \, d\tau . \tag{6.28}$$

For shorthand the diffusion matrix

$$\boldsymbol{D} := \begin{pmatrix} 0 & 0 \\ 0 & D \end{pmatrix} \tag{6.29}$$

was defined. The superscript T denotes the transpose of the matrix.

Equation (6.28) allows a quantitative discussion of a question that was raised at the outset of this chapter, namely on the origin of the observed fluctuations. The first contribution on the right-hand side is the covariance due to the fluctuations at the beginning of the process, also called the homogeneous part $\boldsymbol{\Gamma}^{\mathrm{hom}}$. The second contribution, the inhomogeneous part $\boldsymbol{\Gamma}^{\mathrm{inh}}$, reflects the influence of the permanent random interactions.

Because of (6.19), evaluation of (6.28) is easy. We do not give here the homogeneous part since it is less important. Namely, $\boldsymbol{\Gamma}^{\mathrm{hom}}$ becomes constant for large times while $\boldsymbol{\Gamma}^{\mathrm{inh}}$ increases. We made an a

posteriori estimate and found that less than 5% of the total variance can come from the homogeneous part.

The inhomogeneous part is evaluated as

$$\Gamma_{ll}^{\mathrm{inh}}(t_s) = \frac{T}{m\xi^2}\,[2x - (1-\mathrm{e}^{-x})(3-\mathrm{e}^{-x})]\,,$$
$$\Gamma_{lv}^{\mathrm{inh}}(t_s) = \frac{T}{m\xi}\,(1-\mathrm{e}^{-x})^2\,, \tag{6.30}$$
$$\Gamma_{vv}^{\mathrm{inh}}(t_s) = \frac{T}{m}\,(1-\mathrm{e}^{-2x})\,.$$

Einstein's relation (6.10) was used to eliminate the diffusivity.

We have $\mathrm{TKE} = V_{\mathrm{Cou}}(l) + V_{\mathrm{nuc}} + K_s(v_s)$ in analogy to (4.14). This allows us to find the ultimately searched for variances of the total kinetic energy as

$$\sigma_E^2 = \left[\left(\frac{\mathrm{d}V_{\mathrm{Cou}}}{\mathrm{d}l}\right)^2 \Gamma_{ll}(t_s) + \left(\frac{\mathrm{d}K_s}{\mathrm{d}v_s}\right)^2 \Gamma_{vv}(t_s) + 2\left(\frac{\mathrm{d}V_{\mathrm{Cou}}}{\mathrm{d}l}\right)\left(\frac{\mathrm{d}K_s}{\mathrm{d}v_s}\right)\Gamma_{lv}(t_s)\right]. \tag{6.31}$$

The derivatives are according to (4.10) and (6.24)

$$\frac{\mathrm{d}V_{\mathrm{Cou}}}{\mathrm{d}l} = \frac{-V_{\mathrm{Cou}}}{l}\,, \qquad \frac{\mathrm{d}K_s}{\mathrm{d}v_s} = m v_s\,. \tag{6.32}$$

The remainder of the work is only insertion: put (6.30) and (6.32) into (6.31), use (6.22) to replace v_s and ξ, and eliminate F with (6.6). Finally, one arrives at

$$\sigma_E^2 = \sigma_{E,c}^2 + \sigma_{E,v}^2 - 2\sigma_{E,m}^2 \tag{6.33}$$

with

$$\sigma_{E,c} = V_{\mathrm{Cou}}\,\frac{\Delta l}{l}\left(\frac{2T}{\Delta U}\right)^{1/2}\psi_l(x)\,, \quad \psi_l(x) := \left(\frac{2x-(1-\mathrm{e}^{-x})(3-\mathrm{e}^{-x})}{2(x-1+\mathrm{e}^{-x})}\right)^{1/2},$$
$$\sigma_{E,v} = (T\,\Delta U)^{1/2}\psi_v(x)\,, \qquad \psi_v(x) := \left(\frac{(1-\mathrm{e}^{-x})^3(1+\mathrm{e}^{-x})}{x-1+\mathrm{e}^{-x}}\right)^{1/2}, \tag{6.34}$$
$$\sigma_{E,m} = \left(V_{\mathrm{Cou}}\,\frac{\Delta l}{l}\,T\right)^{1/2}\psi_m(x)\,, \quad \psi_m(x) := \left(\frac{(1-\mathrm{e}^{-x})^3}{x-1+\mathrm{e}^{-x}}\right)^{1/2}.$$

For brevity we wrote here $l := l(t_s)$. $\sigma_{E,c}$ and $\sigma_{E,v}$ were the standard deviations of TKE if the fluctuations of length and velocity would exclude each other. The mixed term $\sigma_{E,m}$ embodies the correlation between length and velocity fluctuations. Note that these correlations diminish the total variance. The reason is the decrease of the Coulomb repulsion for increasing scission length.

The non-dimensional functions ψ_l, ψ_v and ψ_m are shown in fig. 6.2. You might wish to use this figure for quick estimates.

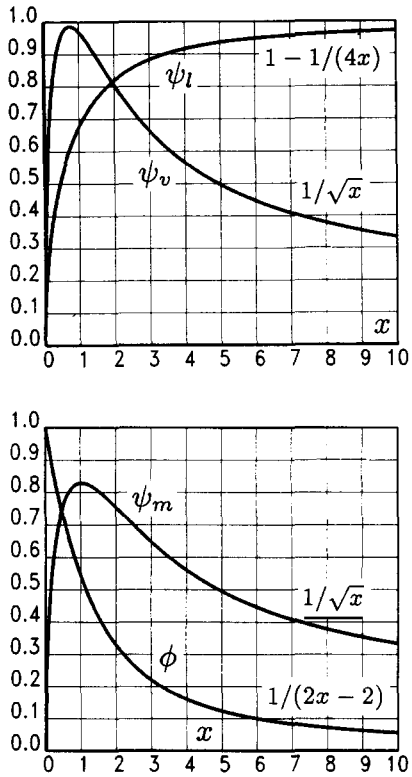

Fig. 6.2. The universal functions $\phi(x)$, $\psi_m(x)$, $\psi_v(x)$ and $\psi_l(x)$ [see eqs. (6.25) and (6.34)] as they depend on the friction parameter x [see eq. (6.23)]. For values of x larger than ten the asymptotics noted at the curves can be taken.

6.4. *Some worked examples*

We shall give a few examples for the application of eq. (6.33) to heavy-ion reactions. These are the simplest cases as shell effects do not play a role. Applications to low-energy fission will be presented in section 8.2.

The cases to be considered are listed in table 6.1. In these reactions it is not clear if deep-inelastic collisions or fusion–fission reactions prevail. For the reactions with uranium, the mass number of the

Table 6.1

TKE standard deviations σ_E, theoretical (t) and experimental (e) for some heavy-ion reactions. This table contains all quantities necessary for the computations explained in section 6.4. Reference to the experimentalists' papers can be found in the last column

Reaction	E_s^* (MeV)	V_{Cou} (MeV)	ΔU (MeV)	Δl (fm)	l (fm)	σ_E^t (MeV)	σ_E^e (MeV)	References
$^{238}U + ^{48}Ca$	100	270	74	11.2	19.2	26	27	[6.22, 6.23]
	200					31	35	
$^{238}U + ^{16}O$	100	224	38	7.0	18.3	20	22	[6.22, 6.23]
$^{98}Mo + ^{98}Mo$	300	173	12	5.0	16.9	28	32	[6.24]

compound system is between 230 and 300. That this is a problematic domain, was discussed in section 5.3. Although lack of discrimination frustrates the computation of mass yields, it does not defeat our access to TKE fluctuations.

Determine first from eq. (6.14) the friction parameter x [defined in (6.23)]. Namely, for the systems with uranium, (6.14) demands $\phi(x) = 0.25$. With the graph of this function in fig. 6.2 we find $x = 2.7$. The values of the universal functions can also be read from fig. 6.2: $\psi_l(x) = 0.87$, $\psi_v(x) = 0.71$ and $\psi_m(x) = 0.68$. For the system with molybdenum, (6.14) postulates $\phi(x) = 0.375$ so that $x = 1.7$ and so forth.

Next the prefactors in (6.34) have to be found. The temperature T follows, according to eq. (6.11), from the excitation energy E_s^* and the mass number A_{cn} of the stretching complex. In heavy-ion reactions, everything on the right-hand side of (6.13) is small compared to E_{inp}, and the input energy is about the same as the *energy loss* E_{loss} so that E_{loss} becomes virtually identical with E_s^*. E_{loss}, however, is an observable that varies widely in heavy-ion reactions, see the reaction $^{238}U + ^{48}Ca$ in table 6.1.

The length l at scission may be estimated from (5.1). More accurate values can be obtained if the mass distribution is available, see section 3.1 for the idea and chapter 4 for the detailed prescriptions. Likewise, a first estimate for the Coulomb repulsion V_{Cou} can be taken from the Coulomb term in the systematics (5.5), $0.14 Z_{cn}^2 / A_{cn}^{1/3}$, and a better value can be found by the methods of chapter 4.

The other numbers required in the prefactors (ΔU, Δl and l) are characteristics of the potential energy. For applications in heavy-ion reactions, where quantal shell effects are negligible, a liquid-drop code may be sufficient. You must determine the potential energy at the barrier, its location and the potential energy at scission.

One general trait of these quantities can be observed in table 6.1: with decreasing total mass number A_{cn} or, equivalently, decreasing fissility (4.17), the length difference Δl and even more the energy difference ΔU decrease sharply. This is the well known confluence of barrier and onset of Rayleigh instability at small fissilities [3.8].

We have entered some of our results into table 6.1. The agreement between calculated values σ_E^t and measured ones σ_E^e is impressive. Of course, the agreement relies on the assumption (vi) in section 6.2, in particular on (6.14). On the other hand, one can say that the simple formulas derived in this chapter establish a comprehensible relation between energy dissipation in nuclear scission and the width of the distribution of the total kinetic energy.

Another point on the physics must still be made. It was claimed in section 4.4 that the prescission kinetic energy should be small, $K_s < 10$ MeV. Evidence for this was presented in section 5.2. Despite this smallness it turned out (see the examples above) that the fluctuations of K_s are not negligible. On the contrary, they are of the same size as K_s itself. This means that a small percentage of all nuclei scission, as far as elongation is concerned, in a state of almost perfect rest. Other degrees of freedom may be quite active.

Summarizing: we now have a handy tool to estimate the fluctuations in total kinetic energy. The system characteristics are taken care of by very simple formulas, namely by (6.34). That these formulas are good enough for a first orientation, was checked by the examples in table 6.1, and more examples will be given in section 8.2. Neither this simple nor any other theory available at present can explain the odd asymptotic behavior of the TKE distribution for large and small total kinetic energies as represented by formula (6.1). Substantial improvements are therefore necessary. However, it is a recent insight that fluctuations in fission grow during a non-equilibrium evolution [6.1–6.12]. We think that this insight, being the central point of the work presented, will stay valid.

7. The systematics of low-energy fission

7.1. Standard, superlong and supershort

Chapter 3 started with an assertion: the most important exit-channel observables are slaves of the prescission shape. A closer look on the data reveals that this might not strictly be true. For example, a *single prescission shape* produces an average of the total kinetic energy $\overline{\mathrm{TKE}}(A)$ with a smooth maximum at mass symmetry $A = A_{\mathrm{cn}}/2$ even if this prescission shape is asymmetrical. Sizeable dips at symmetry, as observed in the fission of uranium, or peaks, as measured for fermium (have a look at fig. 7.3 if you have forgotten these results) seem to be incompatible with the slaving assertion.

The dilemma immediately disappears if one admits that *several prescission shapes* can be formed. Then the nearly equal fragments come from a prescission shape other than the unequal ones. The additional prescission shape must be symmetric (otherwise it would not predominantly produce almost equal fragments) and it must be longer than the usual prescission shape if a dip in $\overline{\mathrm{TKE}}(A)$ is to appear. In contrast, the additional prescission shape must be shorter if a peak in $\overline{\mathrm{TKE}}(A)$ shows up [3.2].

Nevertheless the original theory with only one prescission shape was not completely wrong: most fission is fission of uranium, thorium and californium, and these nuclei produce mostly fragments with some asymmetry and total kinetic energy according to the $\overline{\mathrm{TKE}}$ systematics (5.4). The events at symmetry are rare. One prescission shape, henceforth denoted as the *standard*, is sufficient to cope with more than 95% of all the fission events.

For more precision we need at least three prescission shapes: *standard, superlong and supershort*. Standard is slightly asymmetric and of "normal" length, as shown in fig. 3.2, while superlong and supershort are both almost symmetrical and appreciably longer or shorter than standard.

These differences, being differences in *mean* length, are usually somewhat larger than those caused by the *fluctuations* that were discussed in chapter 6. Hence we expect *separable components in the exit-channel observables* although overlap may occur. We shall notice this in the figs. 7.6, 7.7, 8.3, 8.4, 8.6 and 8.7.

Therefore, mere inspection of measurements induces one to consider several prescission shapes. However, one can also derive the standard, superlong and supershort prescission shapes from theory. They become apparent when single-particle quantum shells are considered as will be detailed in ch. 9. Shell effects dig ditches in potential energy surfaces as shown in fig. 3.3, so that the nucleus is *driven* to the standard, superlong and supershort prescission shapes. Hence there are not only three isolated *shapes*, there are *channels* leading to these prescission shapes, also called standard, superlong and so forth.

The channels traverse the *space of the deformations*. As coordinates in this space we may take the degrees of freedom introduced in ch. 2. The simplest set is (2.14) with semilength l, neck radius r and location z of the dent. Even this requires a three-dimensional space. Since a sheet of paper provides only two dimensions, we must resort to projections onto three planes. In fig. 7.1 these are shown: (l, r) top right, (r, z) top left and (z, l) bottom left.

Consider, for example, the (l, r) projection, top right. The standard channel is distinguished by the full line. It is rooted in the ground state *gs*. To initiate fission, the nucleus lengthens (l increases), and its radius r decreases. Shortly after the point denoted by *2nd min* it becomes energetically favorable to shorten somewhat, while the radius continues to decrease. We call this rebound "the big loop". After the big loop everything proceeds as expected: the nucleus stretches and thins its neck until, just behind the prescission shape at +, two fragments appear.

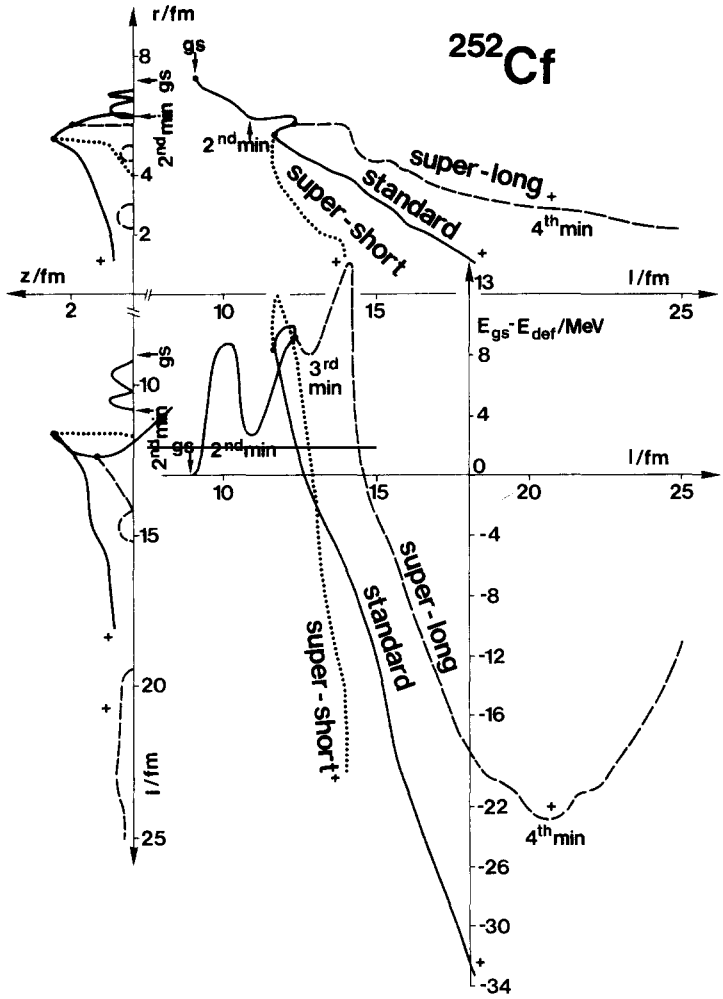

Fig. 7.1. Channel graph of ^{252}Cf. The figure is explained in the text. It was shown first in [3.15]. The poor accuracy of the barriers is caused by the use of the surface parametrization (2.14). Better values can be found in tables 8.2–8.4. Channel graphs of ^{236}U and ^{258}Fm were published in [5.9], [7.1], better ones in [7.2]. A channel graph of ^{232}Th appeared in [8.10].

To each point on the line there belongs a shape. Some shapes representative for the standard channel in californium are shown in fig. 7.2a, c.

What you see in fig. 7.2c are asymmetrical shapes. But one cannot identify asymmetry in the (l, r) projection of fig. 7.1. For this one must consult the (r, z) projection, top left. The full line depicts the same sequence of shapes as the full line in the (l, r) projection, namely the standard channel. We see that the ground state is nearly symmetric, and that, apart from minor deviations, the nucleus stays symmetric until the big loop is reached. Then asymmetry becomes sizeable, $z \approx 2.5$, but during approach to scission asymmetry decreases again.

Let us return to the top-right part of fig. 7.1: there are other lines, dashed and dotted ones. They represent other channels, namely superlong and supershort, which branch from the standard channel at the *bifurcation points*, marked by full circles. All channels finish at various prescission shapes, indicated

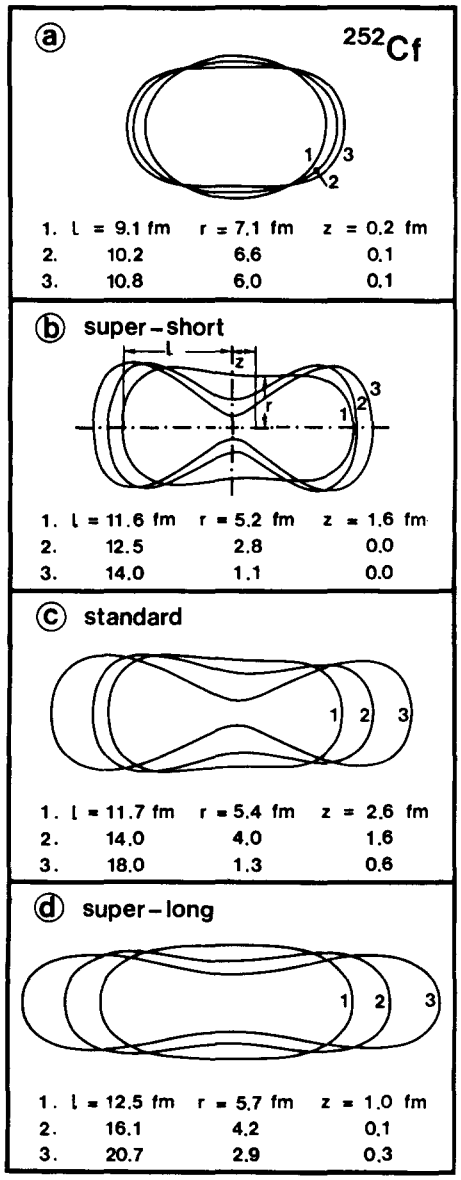

Fig. 7.2. Visualization of the fission channels shown in fig. 7.1 by sequences of shapes. Part (a) depicts the evolution from the ground state to the second minimum. Part (b) illustrates deformation in the supershort fission channel, starting from the bifurcation and ending at prescission (+ in fig. 7.1). Part (c) shows a similar change along the standard channel, but the first outline in the series displays the shape of largest asymmetry. Finally part (d) is like part (b) but is for the superlong case. The formulas relating these shapes with the coordinates (l, r, z) are (2.3), (2.9, 2.10) and (2.15). The figure is taken from [3.15].

by pluses. In principle, the trails of the supershort and superlong channels can also be seen in the other projections (r, z) and (z, l). But since these channels deviate little from symmetry, $z = 0$, their lines almost coincide with the axes, so that only some bulges appear. Pictures of typical shapes on supershort and superlong channels can be found in fig. 7.2b, d.

The fourth part of fig. 7.1, right bottom, shows the potential energy contained in the nucleus as it

floats through one of the channels. For example, the nucleus starts at the ground state *gs* with energy 0 (so is the normalization), climbs the first barrier at $l \approx 10$ fm, falls into the second minimum *2nd min* and rises to the second barrier at $l \approx 12$ fm, after which it descends to scission. The full line describes this travel for the standard channel. The other lines do the same for the other fission channels.

The double-humped barrier and the second minimum in the standard channel have been known since 1972 [1.2] or even since 1964 [1.1], but the system of barriers related to the new fission channels is new. Thus the superlong channel has its own barrier at $l \approx 14$ fm that is higher than any of the standard barriers, and the same is true for the supershort channel at $l \approx 12$ fm.

What are diagrams like fig. 7.1 useful for? First, we can take from them the semilengths l and asymmetries z of the various prescission shapes. With these data we can enter section 4.2, construct the prescission shapes with flat necks, and find, according to sections 4.3 to 4.5, for each prescission shape the yield $Y(A)$ and the other exit-channel variables; see section 9.3 for details. Superposition of the various contributions then gives what should be compared with experiments. However, what is the weight for each contribution? This can be inferred from the barriers shown in fig. 7.1. The highest barrier of the standard channel is lower than the highest barrier of the superlong or supershort channels. Hence we conclude that the standard channel is much more used than the superlong channel, and this is in fact what is observed. However, we must point out that our barrier heights and widths are not good enough for quantitative comparison. However, qualitatively the barrier criterion agrees well with the observations, see section 8.3. Moreover, experimental data can be analyzed so that the weights are eliminated, and the numbers thus extracted, for example, the mean fragment masses, can be compared with the computed ones, see section 7.2, in particular table 7.1.

We stress the role of the bifurcation points. They divide the flux to the various prescission shapes, and hence they decide, in cooperation with the barriers, the distribution of the exit-channel observables. The *system of bifurcation points*, the *system of barriers* and the *system of prescission shapes* are the new items of low-energy fission theory. "Low energy" since they are manifestations of quantal shells, which are smeared out when excitation increases.

Without consideration of *at least three degrees of freedom*, l, r and z, there are but little prospects to predict anything relevant for experiments. We need r to see when the fragments appear, we need l for the average total kinetic energy and we need z to compute the average mass of the fragments. Moreover, as fig. 7.1 clearly shows, it is even impossible to disentangle the various fission channels in a two-dimensional space. For the quantitative comparisons to be presented in the next sections even five degrees of freedom, as introduced in eq. (2.1), were employed.

7.2. Evidence for superlong, standard and supershort

Figures 7.3 and 7.4 give surveys of the most important exit-channel observables as they vary with the compound-nucleus mass number A_{cn}. In fig. 7.3 the yield $Y(A)$ and the total kinetic energy $\overline{\mathrm{TKE}}(A)$ are plotted as functions of the fragment mass number A. In fig. 7.4 the neutron multiplicities $\bar{\nu}(A)$ are shown.

Let us start with a discussion of the experimental data, indicated in these figures by dots. The yield from the fission of astatine ($A_{cn} = 213$) is displayed in fig. 7.3 and is almost exactly what is called liquid-drop fission: one broad hump centered at mass symmetry $A = \frac{1}{2}A_{cn}$. The reason for liquid-drop fission is a high barrier that is overcome only when enough excitation energy is pumped into the system. This, on the other hand, destroys the quantum shells. Only recently [7.3] small shoulders at $A \approx 140$ and, of course, at the complement $A \approx 73$ were discovered. This means that some shell effects are still

Table 7.1

Comparison of calculated (t) and measured (e) values of total kinetic energy $\overline{\mathrm{TKE}}$, average mass $\bar{A}_{\mathrm{H}}$ of the heavy fragment and the standard deviations σ_A of the mass distribution for various fission channels and various nuclei. The total neutron multiplicities $\bar{\nu}^{\mathrm{t}}$ still do not have experimental counterparts, but there is evidence from some measurements that they cannot be completely wrong: see fig. 7 in [5.27] for ^{227}Ac and fig. 6 in [7.13] for the actinides with $A_{\mathrm{cn}} \approx 260$. The reactions by which the nuclei were fissioned can be looked up in the references quoted in the last column. Of course, the special features of these reactions such as their excitation energies were taken into account when the calculations were done. Typical theoretical errors are 5 MeV for the $\overline{\mathrm{TKE}}$, three nucleons for the $\bar{A}_{\mathrm{H}}$ and 25% for the σ_A. The only serious deviations between theory and experiment are thus σ_A for the superlong channel in ^{236}U and the superasymmetric channel in ^{252}Cf. But while the former obviously rests on a problem with the evaluation (see the caption of fig. 7.6), it is theoretical failure that we cannot cope with the superasymmetric channel. Two fermium isotopes were included to demonstrate that none of the observables displayed in this table changes much when only one nucleon is added. Hence there is no risk in taking the characteristics of nuclei such as ^{238}U, ^{238}Pu and ^{260}Md from this table. Important companion tables are 8.5, which contains the theoretical raw data needed for this presentation, and table 8.6 with comparisons between computed and measured TKE variances σ_E^2

Nucleus	Channel	$\overline{\mathrm{TKE}}^{\mathrm{t}}$ (MeV)	$\overline{\mathrm{TKE}}^{\mathrm{e}}$ (MeV)	$\bar{A}_{\mathrm{H}}^{\mathrm{t}}$	$\bar{A}_{\mathrm{H}}^{\mathrm{e}}$	σ_A^{t}	σ_A^{e}	$\bar{\nu}^{\mathrm{t}}$	References
^{213}At	standard	153	147	133	137	5.4	3.9	2.3	[7.4, 7.5]
	superlong	148	146	108	107	7.6	8.9	4.9	
^{227}Ac	standard	170	164	134	139	5.6	6.0	3.4	[5.27, 1.10]
	superlong	158	153	114	114	8.7	9.5	5.4	
^{232}Th	standard I	176	168	135	135	4.1	3.6	2.5	[7.6]
	standard II	168	158	139	143	5.7	4.3	3.1	
	superlong	155	153	116	116	9.2		5.7	
^{236}U	standard I	186	187	135	134	3.4	2.6	2.0	[1.8]
	standard II	176	167	141	141	5.9	5.0	2.9	
	superlong	150	157	118	118	12.9	4.1	7.3	
^{240}Pu	standard I	192	192	136	134	3.9	2.8	2.0	[7.7, 7.8]
	standard II	184	175	141	140	5.5	5.7	2.8	
	superlong	156		120		12.2		7.3	
^{252}Cf	supershort	226		126		1.8		0.1	[6.13]
	standard I	205	200	137	135	4.6	3.2	2.5	
	standard II	194	188	147	143	6.1	5.0	3.5	
	standard III		176		149		7.1		
	superasymm.	179	146	161	178	7.0	2.3	3.6	
	superlong	173	180	128	127	13.2	11.6	6.5	
^{255}Es	supershort	226		131		3.1		1.1	[5.8]
	standard	203		143		6.3		3.2	
^{258}Fm	supershort	230	230	132	130	3.1		1.1	[7.9, 1.11]
	standard	207	205	145		6.2		3.0	
^{259}Fm	supershort	231	235	130	130	2.6		1.2	[7.10]
	standard	204	200	145		6.3		3.5	
^{272}[108]	supershort	245		139		6.5		3.7	[7.16]
	standard	194		155		19.2		7.7	

alive when ^{213}At fissions. However, observation of such shoulders becomes increasingly difficult when A_{cn} decreases so that we may loosely say that ^{213}At is the lightest nucleus that fissions under the rule of quantal effects. When we go to examine the yield of actinium, we find that both components, that at symmetry and that at $A \approx 140$, still exist, but their weight has changed dramatically. The asymmetric component is now as important as the symmetric one, and the trend continues. At $A_{\mathrm{cn}} = 236$ the

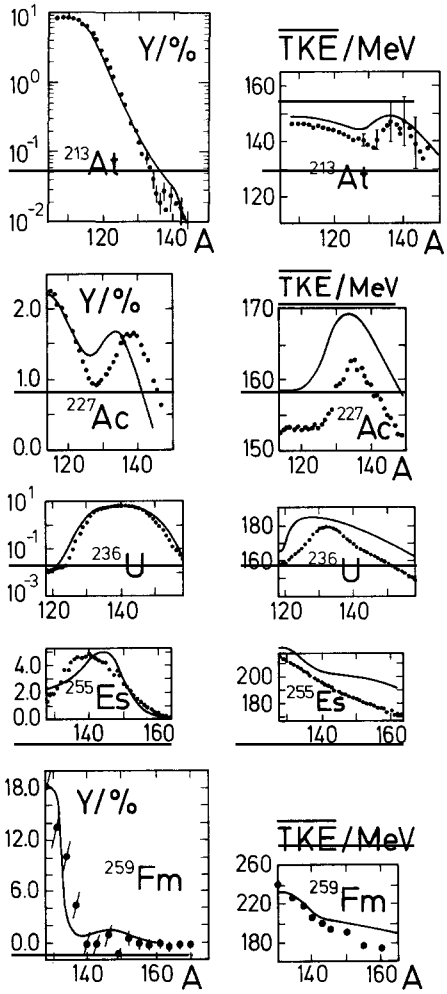

Fig. 7.3. The main examples for fission of preactinides and actinides. Shown are the yields Y (left-hand column) and total kinetic energies $\overline{\mathrm{TKE}}$ (right-hand column) as functions of the fragment mass number A. Mass symmetry is always located at the left edges of the viewports. Full dots, sometimes with error bars, represent the experimental results. The respective quotations can be found in table 7.1. The lines come from the theory, which is explained in the text. The numbers it takes to construct these lines are given in the tables 7.1 and 8.5.

symmetrical component has almost disappeared; we must use a logarithmic scale to make it visible. The asymmetric component alone determines the shape of the yield. However, at still larger A_{cn} the trend seems to reverse. In the fission of einsteinium, quite a few events at symmetry were observed, and for ^{259}Fm the central component is dominant again.

Figure 7.3 indeed contains the systematics of the yields. Everything in between can be obtained by smooth interpolation of neighboring systems. The yield of thorium, for example, is between the yield of actinium and uranium, and so forth. Similar statements hold for $\overline{\mathrm{TKE}}(A)$ and $\bar{\nu}(A)$ in fig. 7.4.

In the whole range of preactinides and actinides certain characteristics of the yield stay remarkably stable. There is a symmetrical component and one at asymmetry ($A \approx 140$). Only their predominance changes. Furthermore, there seem to be only two small sections of A_{cn} where dramatic variations occur: one at $A_{\mathrm{cn}} \approx 227$ and the other one at $A_{\mathrm{cn}} \approx 257$.

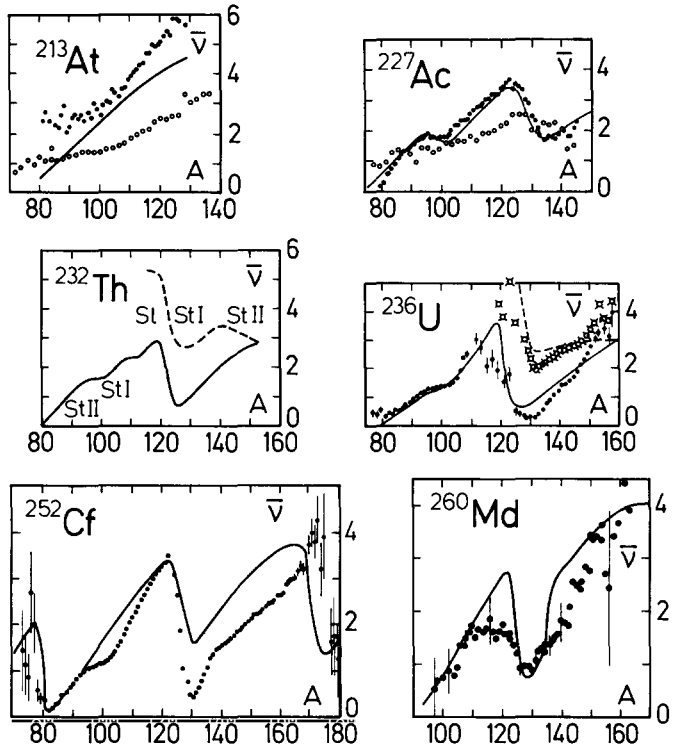

Fig. 7.4. Systematics of the neutron multiplicities as functions of the fragment mass number A. Dots are from experiments, lines from theory. The references to the experimental works are: for ^{213}At [5.24, 5.25], for ^{227}Ac [5.26, 5.7], for ^{236}U [7.12], for ^{252}Cf [6.14] and for ^{260}Md [7.13]. The major part of the theoretical results have been published previously; for the cases ^{213}At and ^{227}Ac see [3.12], for ^{252}Cf [3.1, 3.2], and for ^{260}Md [3.1] as well as [7.13]. The prediction for the neutron multiplicity of ^{232}Th will be discussed in section 8.4. Much in this figure is already history. For example, in the prediction for ^{252}Cf we could now achieve much better agreement with the experimental data by taking the standard splitting into account; three years ago this was still a too novel subject.

The central components that prevail in the preactinides and in the heaviest actinides do not have much in common [7.4]. This can already be recognized from the variances σ_A^2 of the central components: for astatine $Y(A)$ it is broad, whereas it is narrow for fermium. The difference becomes even more obvious when one studies the $\overline{\mathrm{TKE}}(A)$ functions on the right-hand side of fig. 7.3. For astatine the asymmetric events are elevated over the symmetrical ones. One appreciates the significance of this fact all the more when one remembers that normally asymmetric events must have depressed kinetic energies due to the well known factor $Z(Z_{\mathrm{cn}} - Z)$ in the Coulomb repulsion, cf. eq. (4.10). The energetic elevation becomes increasingly pronounced as A_{cn} increases. So we see for uranium the famous dip in $\overline{\mathrm{TKE}}(A)$ at symmetry, which was already alluded to in section 7.1. If the symmetric components for light and heavy actinides were of the same kind, we should also expect that the heavy actinides produce a dip in $\overline{\mathrm{TKE}}(A)$. However, the opposite is true: $\overline{\mathrm{TKE}}(A)$ has for einsteinium its maximum at symmetry, and for fermium we even find a peak. This erratic behavior of $\overline{\mathrm{TKE}}(A)$ cannot be explained by a single symmetrical fission channel. Instead, it is the superlong channel that is productive in the lighter actinides ($A_{\mathrm{cn}} \leq 252$). It produces events at small total kinetic energy and gives, in accordance with random neck rupture, broad mass distributions as discussed in section 5.5. And it is the supershort fission channel operative in the heavier actinides ($A_{\mathrm{cn}} \geq 252$) that generates

events with high $\overline{\mathrm{TKE}}$ and narrow mass distributions. We shall also see in section 9.4 that the microscopic structures of the superlong and supershort channels are different.

When the mass distribution $Y(A)$ and the total kinetic energy $\overline{\mathrm{TKE}}(A)$ are expanded over the full range of A, we see two Bactrian camels for ^{236}U and two dromedaries for ^{259}Fm. This correspondence is misleading since it suggests that $Y(A)$ and $\overline{\mathrm{TKE}}(A)$ contain similar information which is, of course, not true as can be seen from the other examples in fig. 7.3. $Y(A)$ of ^{236}U tells us that there are few fission events at mass symmetry. The value of $\overline{\mathrm{TKE}}(A)$ of ^{236}U, on the other hand, reveals that these few events come with a very low total kinetic energy. Therefore, one can derive the existence of the superlong channel from $\overline{\mathrm{TKE}}(A)$, while a similar conclusion based on $Y(A)$ is hard. Analogous arguments hold for ^{259}Fm: its yield shows only the supershort component; contributions from the standard channel are swamped by statistical noise. However, the sharp drop of $\overline{\mathrm{TKE}}(A)$ for increasing A proves the presence of the standard channel.

The lines of figs. 7.3 and 7.4 represent theoretical results from the joint efforts of random neck rupture and the quantum-mechanical potential-energy calculations which will be detailed in ch. 9. The potential-energy calculations give us the prescission shapes (collected in table 8.5). From the prescission shapes, individual yields $Y_c(A)$, total kinetic energies $\overline{\mathrm{TKE}}_c(A)$ and neutron multiplicities $\bar{\nu}_c(A)$ are obtained using the procedures compiled in ch. 4. The subscript c labels the various channels. When we wish to compare with measurements, we form the superpositions

$$Y(A) = \sum_c p_c Y_c(A)\,, \tag{7.1}$$

$$\overline{\mathrm{TKE}}(A) = \sum_c p_c \overline{\mathrm{TKE}}_c(A) Y_c(A)/Y(A)\,, \tag{7.2}$$

$$\bar{\nu}(A) = \sum_c p_c \bar{\nu}_c(A) Y_c(A)/Y(A)\,, \tag{7.3}$$

where the channel probabilities p_c indicate how much channel c is frequented. They are normalized as

$$\sum_c p_c = 1\,. \tag{7.4}$$

All functions $Y_c(A)$, $\overline{\mathrm{TKE}}_c(A)$ and $\bar{\nu}_c(A)$ are output of the procedures of random neck rupture. However, for information reduction one may write without loss of accuracy

$$Y_c(A) = \frac{1}{(2\pi\sigma_{A,c}^2)^{1/2}}\left[\exp\left(-\frac{(A-\bar{A}_c)^2}{2\sigma_{A,c}^2}\right) + \exp\left(-\frac{(A-A_{\mathrm{cn}}+\bar{A}_c)^2}{2\sigma_{A,c}^2}\right)\right] \tag{7.5}$$

and

$$\overline{\mathrm{TKE}}_c(A) = \frac{A(A_{\mathrm{cn}}-A)}{\bar{A}_c(A_{\mathrm{cn}}-\bar{A}_c)-\sigma_{A,c}^2}\,\overline{\mathrm{TKE}}_c \tag{7.6}$$

so that two functions are defined by three numbers: the average mass $\bar{A}_c$, the mass variance $\sigma_{A,c}^2$ and the average total kinetic energy $\overline{\mathrm{TKE}}_c$. Random neck rupture delivers these numbers as byproducts. They are quoted in table 7.1 and are equipped with a superscript t to indicate their theoretical origin.

The present theory of multichannel fission has a weakness: while it seems suitable to compute the prescission shapes, it cannot provide accurate values for the channel probabilities p_c. The graphs in fig.

7.3 were made by taking the computed functions $Y_c(A)$, putting them into (7.1) and adjusting the p_c until the best fit to the experimental yield was achieved. The thus obtained p_c are listed in table 8.5. They must be considered as experimental data.

The honest way of comparison between theoretical and experimental items is presented in table 7.1. The experimenters take their data and fit them with formulas essentially identical with (7.1) to (7.6). However, they keep all the parameters free for adaption. In this way they find experimental values for $\bar{A}_c$, $\sigma_{A,c}$ and $\overline{\mathrm{TKE}}_c$. The first state-of-the-art evaluation of this kind was made by Knitter et al. [7.11].

With a small modification we can now repeat the claim made at the beginning of section 3.1: the exit-channel observables are slaves of the prescission shapes. Now that we have understood this principle by means of the yield and the total kinetic energy, the neutron multiplicities $\bar{\nu}(A)$ cannot cause us any major surprises.

For ^{213}At the prominent contribution comes, as we see in fig. 7.3, from superlong, that is from a symmetric prescission shape. Consequently, according to rule (2) of random neck rupture (section 3.1), we expect a $\bar{\nu}(A)$ that looks like an ascending line; and this is what we see in fig. 7.4. The standard component is so weak that it was not seen in the classic multiplicity measurements.

However, in ^{227}Ac the standard prescission shape is as often made for as superlong. Since the standard shape is asymmetric, we expect from it a sawtooth-shaped neutron multiplicity; see again rule (2) in section 3.1. Moreover, as contributions from the superlong channel are still large, we should see the sawtooth superimposed on an ascending line. From an inspection of the superposition formula (7.3) we learn that the ascending line should show up at mass symmetry whereas the sawtooth should have its domain at the outskirts; and this is what we see in fig. 7.4.

In ^{236}U the standard prescission shape generates the aforementioned camel humps in the yield $Y(A)$. The humps are so close to each other that they almost swamp the small contributions from the superlong channel. $\bar{\nu}(A)$ looks like a single sawtooth. However, there is a means to detect the presence of the superlong channel even in such difficult cases: one plots the total multiplicity $\bar{\nu}(A) + \bar{\nu}(A_{\mathrm{cn}} - A)$. The total multiplicities are distinguished in fig. 7.4 by the crosses with open circles. The corresponding theoretical line is broken. Now if events from the superlong channel occur, we observe a steep rise in the total multiplicity for $A \approx A_{\mathrm{cn}}/2$. This is in accordance with the random neck rupture rule (1) in section 3.1. One can go one step further and compute the channel-averaged total neutron multiplicity

$$\bar{\nu}_c = \frac{1}{2} \sum_A [\bar{\nu}(A) + \bar{\nu}(A_{\mathrm{cn}} - A)] Y_c(A) \,. \tag{7.7}$$

The multiplicity $\bar{\nu}_{\mathrm{sl}}$ from the superlong channel is considerably larger than that from the standard channel $\bar{\nu}_{\mathrm{st}}$, see table 7.1.

In addition, the neutron multiplicity of ^{252}Cf is dominated by the standard channel's sawtooth curve. However, at very large asymmetries two new sawteeth appear. This feature is produced by the superasymmetrical prescission shape [cf. fig. 3.1d], which gives contributions to the yield at very large mass asymmetries and induces a multiplicity $\bar{\nu}_c(A)$ that exhibits an even more prominent sawtooth than standard. The properties of the superasymmetric fission channel will be discussed in section 8.5.

^{260}Md fissions mainly through the standard and supershort channels. Supershort is symmetrical; hence it generates a straight multiplicity curve. However, the total neutron multiplicity $\bar{\nu}_{\mathrm{ss}}$ is small (cf. table 7.1) since the supershort prescission shape is short. When we combine this with the sawtooth shape from the standard channel, we expect a rift at mass symmetry. Precisely this can be seen in fig. 7.4.

Neutron multiplicities $\bar{\nu}(A)$, therefore, do not seem to contain information that exceeds the information obtained from yield and total kinetic energy. This is quite a strong validation of random neck rupture. Furthermore, the functions $\bar{\nu}(A)$ are important for many practical purposes, but their measurement is difficult even today. Therefore it is useful that we have a theory to predict these functions, typically with an accuracy of one neutron. In fact, much of the calculated data in fig. 7.4 is a proper forecast. For example, the three sawteeth in ^{252}Cf were published first as computational results [3.1]. The rift in the neutron multiplicity of ^{260}Md was computed before it was measured [3.1, 7.13], and it seems that for such an important fissioning nucleus as ^{232}Th no measured $\bar{\nu}(A)$ is available. So we thought it would be apt to have at least a prediction.

One can increase the accuracy of the predictions by taking the characteristics of the prescission shape not from the potential-energy calculations but from the experimental yield. This corresponds to the first strategy discussed in section 4.2. Figure 7.4 was constructed in this way. Had we worked with theoretical data only, we would have obtained the same features as are shown now.

7.3. Channel-differentiated $\overline{TKE}$ and $\bar{A}_H$ systematics

The two most important characteristics of the mass and total kinetic energy distributions are the average mass number $\bar{A}_H$ of the heavy fragments and the average $\overline{TKE}$. The overall systematics of $\overline{TKE}$ is displayed in fig. 5.1. The overall systematics of $\bar{A}_H$ is so simple that it needs no graph: $\bar{A}_H$ stays almost constant at 140 for fission of nearly all the actinides. With the materials presented in fig. 7.3 and table 7.1 we can now establish *differentiated systematics*, that is $\overline{TKE}$ and $\bar{A}_H$ for every fission channel severed. The result can be seen in fig. 7.5. The features of the standard channel are shown by the full lines, the dashed lines are related to the superlong channel and the supershort channel is distinguished by the dots.

Let us start with fig. 7.5b. The standard channel, split into components I and II, stays quite close to the dash-dotted line. But the dash-dotted line represents the overall $\overline{TKE}$ systematics so that we have another reason for the naming of the standard channel. Anticipating section 8.4, we now state: the standard II is the most bountiful channel in most actinides. Therefore it is the proximity of standard II to the overall $\overline{TKE}$ systematics that counts. The supershort channel gives, naturally, much too high kinetic energies while the superlong channel's $\overline{TKE}$s are much too low. Notice the convergence of the superlong $\overline{TKE}$ to the overall systematics for light systems. Thus for astatine, where the superlong channel is prevalent, its characteristics do not deviate much from the liquid-drop behavior.

Figure 7.5c represents the differentiated systematics of the mean mass number $\bar{A}_H$ of the heavy fragments. We display it by plotting the light fragment mass number $\bar{A}_L$ as a function of $\bar{A}_H$. (Clearly, the system size A_{cn} is given by $\bar{A}_L + \bar{A}_H$.) As desired by nature, the standard channel, in particular standard II, remains nearly constant at $\bar{A}_H \approx 140$. The superlong and supershort channels enforce symmetrical fission. Their $\bar{A}_H$ appear thus on the diagonal.

What leaps into mind when one considers figs. 7.5b, c is the smooth behavior of these characteristics. From this it is inconceivable how the exit channel observables can change drastically as is shown in figs. 7.3 and 7.4. In addition, it strikes one that the lines for the various channels are drawn only for limited ranges of the system size.

Both questions can be answered with fig. 7.5a. There the channel probabilities p_c for the three main fission channels are depicted. This diagram tells us that for systems smaller than $A_{cn} \approx 250$ the supershort channel disappears and the respective probability p_{ss} is zero. For systems larger than $A_{cn} \approx 260$ the superlong channel breaks up. The standard channel, in contrast, exists everywhere. The

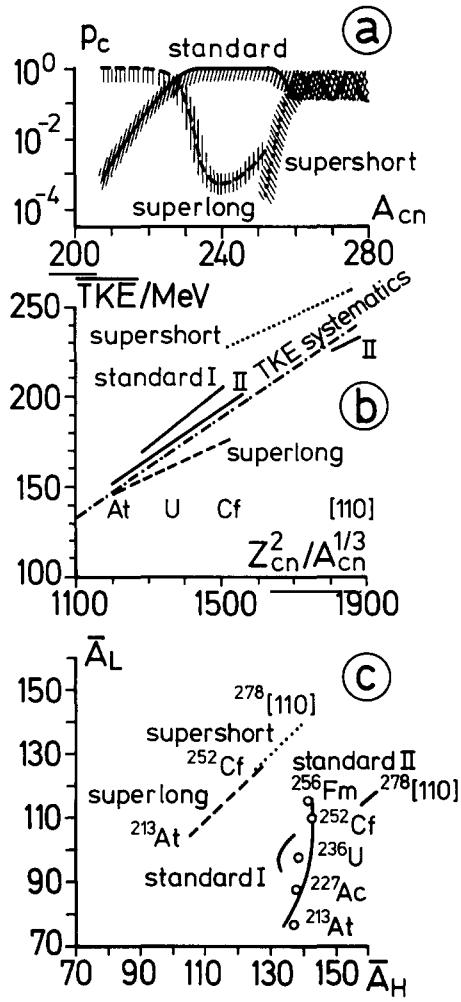

Fig. 7.5. Channel probabilities p_c, mean total kinetic energy $\overline{\mathrm{TKE}}$ and average mass number $\bar{A}_{\mathrm{H}}$ of the heavy fragments as they vary with the size of the fissioning system. The open dots are from measurements compiled by Flynn et al. [7.14], except for the systems ^{213}At and ^{227}Ac for which the relevant references are [7.3–7.5] and [5.27], respectively. Note that this is a schematic picture. We have no precise method to compute the channel weights p_c. They were estimated from the heights of the computed barriers collected in the tables 8.2 to 8.4 and from the fitted p_c listed in table 8.5. To indicate the lack of accuracy, the lines in part (a) are enclosed in different sorts of hatching. The other parts of the figure appeared first in [7.15]. They were computed using the "liquid-drop-energy minimization method" [variant (ii) in section 9.2] and are therefore less accurate than the values given in table 8.1. We decided to make the juxtaposition in order to show the reliability of our searching techniques.

drastic change of the observables is caused by the drastic variation of the population probabilities p_c. This variation can be related to the relative height of the barriers. We shall discuss the respective results in section 8.3.

Enticed by recent data from a heavy-ion reaction in which apparently the nucleus ^{272}[108] was produced [7.16], we calculated a channel graph like fig. 7.1 for this system and a few others in the same mass range. We saw no qualitative changes as compared to systems like ^{259}Fm. The standard and supershort channels still exist. But their properties are somewhat altered. The supershort channel is quite long so that the supershort $\overline{\mathrm{TKE}}$ systematics approaches the overall $\overline{\mathrm{TKE}}$ systematics, as shown in fig. 7.5b. The standard channel, for its part, becomes exceedingly long and so gives rise to events with

small $\overline{\text{TKE}}$. This is indicated by the detached piece in fig. 7.5b. Correlated with the large length of the prescission shape is a huge value of the standard deviation σ_A, see table 7.1. But the standard channel's asymmetry also grows. This causes a mean mass number $\bar{A}_H$ that deviates substantially from the 140 systematics, see in fig. 7.5c the piece of line at $\bar{A}_H \approx 160$. These theoretical results have nothing to do with the data from the heavy-ion reaction reported in [7.16]. The reason is probably that in the experiment something like a compound nucleus was never formed so that the observations reflect entrance channel effects.

7.4. The independence of fission channels

From the theoretical point of view the existence of several fission channels is proven by calculations as described in ch. 9. However, a sceptic who does not believe in theory might ask for direct experimental verification. After all, nature does not always comply with Gaussians, as in eq. (7.5), so that the whole multichannel business might not be more than a fitting device. Stocker, for example, showed that the somewhat angular shape of the yield from uranium (see fig. 7.3) can be described by a Pólya distribution [7.17]. Similarly, the yields calculated in the scission-point model usually do not have a Gaussian shape [1.4], and it makes no sense to claim that they are composed of Gaussians.

To make the point clear: we do not consider the Gaussian (7.5) to be more than an approximate representation of the yield from one fission channel, but *the independent existence* of the standard, superlong and supershort channels, and even the standard I/II splitting (section 8.4) is proven by experiments.

The most convincing evidence was obtained by Hambsch and co-workers [1.8]. They studied neutron-induced fission of ^{236}U at various impact energies E_n of the neutrons. It turned out that changes of E_n by a few eV could alter the overall $\overline{\text{TKE}}$ by half an MeV. Inspection of the data revealed that the production of fragments in certain mass ranges could be suppressed or enhanced by tiny changes of E_n. An example is shown in fig. 7.6. Conjectures that such variations were related to the spin of the compound nucleus turned out to be wrong. The scission-point model, on the other hand, is quite unable to explain such data: it must attribute a change in the yield to a change of temperature. But a change of E_n by a few eV does not alter the temperature of a fissioning nucleus. The only explanation of the experiment [1.8] is a bifurcation point: somewhere in the evolution to fission, the nucleus must have the choice to follow at least two different trails, and the decision must not cost energy. Exactly this point is described by channel graphs like fig. 7.1.

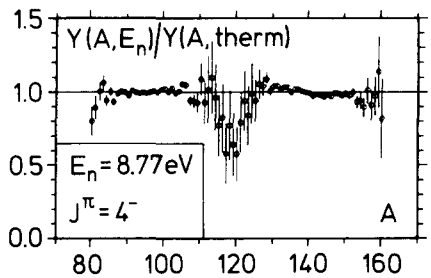

Fig. 7.6. Shown is the ratio $Y(A, E_n)/Y(A, \text{therm})$ of mass yields from ^{235}U(n, f) measured at the neutron impact energy E_n with total angular momentum J and parity π, and at thermal impact energies [1.8]. The dip at $A \approx 118$ indicates suppression of fission through the superlong channel by 50%. Due to the representation by a quotient, one cannot deduce the width of the superlong component from this figure. A more reliable width is displayed in fig. 1 of [7.29].

Similar evidence, but with very different methods, was obtained by Hulet and co-workers [1.11]. They showed that the addition of only one neutron to a spontaneously fissioning nucleus can drastically change its mass and TKE distributions, see fig. 5.3. Again, as in the experiment [1.8], the changes in the observables are much too large in comparison with their cause as to be covered by a scission-point model. Here as well, the only explanation is a bifurcation point. The addition of the single neutron lifts a certain barrier close to that bifurcation point by a fraction of an MeV. This is enough to make the respective fission channel less attractive. We shall discuss the mechanism in section 8.3.

The evidence presented in the figs. 5.3 and 7.6 refers to the existence of the supershort, superlong and, of course, the standard channels. The first evidence for the independence of the standard I and II channels was presented in [1.8]. Most beautiful in this respect is, however, the recent work by Wagemans and his colleagues [7.7, 7.8]. They studied the isotopes ^{236,238,240,242}Pu and demonstrated that the addition of only two neutrons affects very much the way in which fission drifts through the standard I and standard II channels. For this too we can propose a theoretical explanation, see section 8.4.

7.5. How can one steer nuclear fission?

Only when we can change things, are we sure that we understood something. So how can we use the knowledge on channels to modify fission?

The most straightforward way is to increase the excitation energy of the compound system. This increases the probability that the nucleus overrides not only the lowest but also the higher barriers. The most important application of this technique is everything concerning the superlong fission channel. As can be seen in fig. 7.1, the barrier of the superlong channel is higher than that of the standard channel, and this is typical for all actinides. Thus we are not surprised when we find in fig. 7.7 much more yield from the superlong channel at the higher excitation energy. A behavior as shown in fig. 7.7 was formerly interpreted as melting of quantal shells [7.18]. Although such an interpretation is correct at high excitation, it cannot be true for the first few MeV where the destruction of BCS pairs tends to reinforce the shells [1.7].

A more subtle way to reshuffle the frequentation of the channels has already been discussed in the previous section: the various resonances in neutron-induced fission give different yields. But it is not clear what it is in a fixed resonance that gives rise to the observed yield. It remains to find the true switch. Furman and Kliman [7.19, 7.20] demonstrated the effect of the *Bohr transition states* [7.21, 7.22, 1.7] on the decision at a certain bifurcation point. To understand the arguments of Furman and Kliman, it might be best to envisage fission in two stages: in the first one, the *entrance*, the neutron is captured, the compound nucleus formed and the top of the channel barrier climbed – only one barrier is considered. In the second stage, the *exit*, the nucleus descends and scissions. In other words, the entrance connects the resonance λ with the transition state $J^\pi K$, while the exit joins $J^\pi K$ with the prescission shape c. The total angular momentum J and the parity π are good quantum numbers. But none of the labels λ (resonance tag), K (projection of angular momentum on the body-fixed axis) or c (channel tag) expresses a conserved quantity. Hence the only relation we can expect is by probabilities. Let $p_{K,\lambda}$ denote the probability that the nucleus goes from the resonance λ to the transition state $J^\pi K$. Next take $p_{c,K}$ as the probability for the transition from $J^\pi K$ to c. Then according to probability theory plus a Markovian assumption we must have

$$p_{c,\lambda} = \sum_K p_{c,K}\, p_{K,\lambda} \,. \tag{7.8}$$

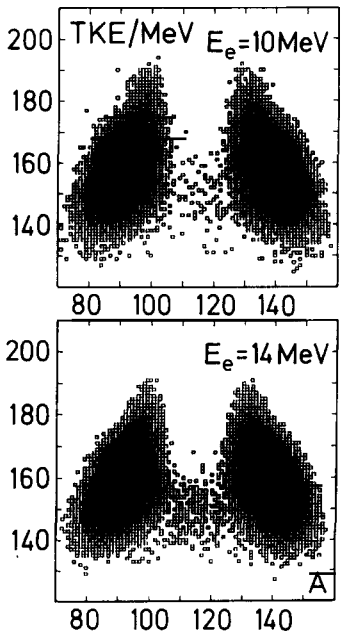

Fig. 7.7. Mass and total-kinetic-energy distribution $Y(A, \mathrm{TKE})$ from photofission of ^{232}Th. In contrast to the yields $Y(A)$ assembled in fig. 7.3 we have here a contour plot of the yield as a function of fragment mass number A and total kinetic energy TKE. Darker regions correspond to higher yield. The two heavy wings come from standard fission. The events at symmetry ($A \approx 116$, TKE ≈ 150 MeV) are products of the superlong channel. E_e denotes the energy of the electrons that generate the fission-inducing photons by bremsstrahlung. The difference between the average excitation energies is considerably smaller than 4 MeV, perhaps 1 MeV. The data is taken from [7.6].

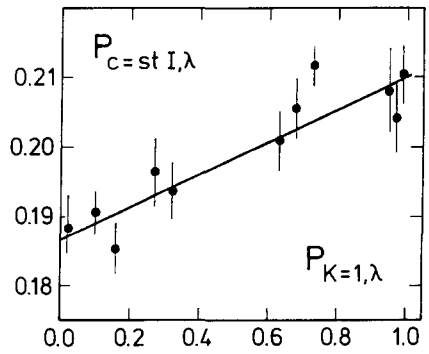

Fig. 7.8. The channel probability $p_{c=\mathrm{stI},\lambda}$ as a function of the entrance probability $p_{K=1,\lambda}$. The results for the various resonances λ appear as dots with error bars. The straight line displays the best linear fit [7.20]. All these resonances have $J^\pi = 4^-$. They can only reach the two states $K=1$ and $K=2$. This makes evaluation of (7.8) very simple because $p_{K=2,\lambda} = 1 - p_{K=1,\lambda}$. On the left-hand side of (7.8), only the probabilities for fission through the standard I and II channels have been considered (see section 8.4). This is legitimate since the contribution of the superlong channel is tiny in ^{235}U(n, f).

The $p_{c,\lambda}$ are the same channel probabilities as used in equations (7.1)–(7.4). They were only customized by λ.

The probabilities $p_{c,\lambda}$ and $p_{K,\lambda}$ are known for ^{235}U(n, f): the $p_{c,\lambda}$ can be obtained from fits of the yield, as described in section 7.2. Tables for ^{236}U are given in [1.8]. The $p_{K,\lambda}$ are derived from interference effects in the energy dependence of the spin-separated fission cross-section. Pertinent data are collected in refs. [7.23–7.25]. However, we do not know the $p_{c,K}$. Nevertheless, we can check eq. (7.8) since it postulates a linear relationship between the known probabilities. Such a check is shown in fig. 7.8. The figure shows first that the Markovian assumption seems to be right. Otherwise the $p_{c,K}$ would also depend on the resonance λ, and this would impair the linear dependence. Second, we see that the channel probabilities $p_{c,\lambda}$ can in fact be changed if the transition state is altered. For example, the probability $p_{c=stI,\lambda}$ is 0.21 when fission proceeds via the state 4^- 1. The same probability is only 0.19 when the state 4^- 2 is passed.

It deepens insight when one appreciates the difference between the two probabilities $p_{c,K}$ and $p_{K,\lambda}$. The randomness described by the entrance channel probabilities $p_{K,\lambda}$ is caused by the complex multiparticle interactions which form the compound states. Strong Coriolis forces then mix several

transition states J^{π} K into one compound state λ [7.26]. Therefore, we expect the $p_{K,\lambda}$ to depend irregularly on both indices. In contrast the exit-channel processes can be figured as the propagation of a wave packet in the low-dimensional space of deformations (think of our variables l, r, z, s, c, section 2.1). Thus only smooth changes of the $p_{c,K}$ with K should occur. In fact, one can infer this from fig. 7.8: with eq. (7.8) and the knowledge that only two intermediate states are involved we find $p_{c=\mathrm{stI},K=1} = 0.21$ and $p_{c=\mathrm{stI},K=2} = 0.19$, whereas $p_{K=1,\lambda}$ actually varies between 0 and 1.

One may even picture these results if one accepts a popular interpretation of the transition states [7.22, p. 42]: states with negative parity and odd K are said to suppress mass asymmetry while those with negative parity and even K do the opposite. The standard I channel is the more symmetric one (see section 8.4). Hence, it is plausible that it is more frequented when the symmetry-friendly state 4^- 1 is involved.

A fine discussion of the same topic with somewhat different emphases was presented by Moore and co-workers [7.27].

The Markovian assumption underlying eq. (7.8) amounts to the assertion that it does not matter *how* a certain K is reached. Hence fission by gamma rays and other particles should reveal similar regularities as those displayed in fig. 7.8. The first steps in this direction, involving a coincident measurement of mass and angular distributions, were undertaken by Wilke et al. [7.28].

The quantum number K describes properties of a solid body. It is not cogent to associate it with dynamic deformations. If one wishes to affect the *dynamics at the bifurcation points*, one should rather impose vibrations with definite symmetry on the nucleus. This was recently achieved by Weber et al. [7.29]. The tool was inelastic electron scattering with coincident registration of the fragments and the scattered electrons. In this way not only the energy but also the multipolarity of the excitation was controlled. A typical result is shown in fig. 7.9. For all multipolarities, the yield at symmetry grows with increasing excitation energy. This is the simple effect discussed in the context of fig. 7.7, namely that a higher excitation energy facilitates penetration of the superlong barrier. But the superior information is contained in the *enhanced increase of the superlong yield* when *even giant resonances* (E2 and E0) are excited. This again is plausible since the superlong channel is a symmetrical channel, whereas the standard channel is asymmetrical, see fig. 7.1.

In summary, we know nowadays of three ways to steer fission: by excitation energy, by making for transition states with chosen K and by giant resonances with definite multipolarity.

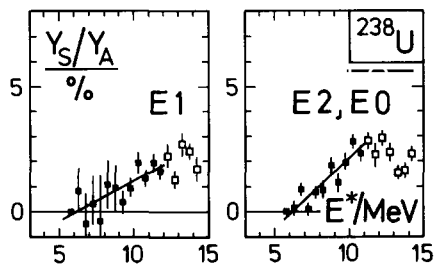

Fig. 7.9. Fission of ^{238}U by virtual photons exciting the giant monopole ($E0$), dipole ($E1$) and quadrupole ($E2$) resonances. The ratios Y_S/Y_A of yields at mass symmetry $A \approx 119$ and asymmetry $A \approx 140$ are shown as functions of the excitation energy E^*. Around $A \approx 119$ and $A \approx 140$ suitable mass windows were set up. Details can be found in [7.29] where the data is also taken from. The kink at $E^* \approx 12$ MeV is related to second-chance fission and has hence no meaning for the present subject. Therefore, for the straight-line fit, only the data distinguished by the full symbols were taken.

8. Peculiarities of fission channels

8.1. The tree of nuclear fission

Today it is not a real problem to compute the potential energies E_{def} of a deformed nucleus. It takes more skill to extract information from such a high-dimensional data set. Clearly, the function E_{def} has minima and saddle points, but how are they connected to each other? One way to see this could be by dynamics: one should start on one of the saddles, push the nucleus in some direction, and look to which minimum it moves. This would be feasible in calculations only, and even there it cannot be done at present since reliable enough inertial tensors are not available. One may, nevertheless, obtain information on the connectivity from the potential energy alone, namely by paths of steepest descent. This has been done in most of the work reviewed here, and the connecting paths are now called fission channels.

Usually at this point nuclear purists start to assert that such paths have no meaning at all. They argue that fission is a dynamical process so that one should build a metric from the inertial tensor, derive new coordinates based on that metric so that the inertial tensor becomes diagonal, and display the potential energy in these coordinates. In other words, the potential energy must undergo a topological transformation before it becomes useful for interpretation. As long as this transformation is not known, only those properties of the potential energy must be taken seriously that remain invariant under diffeomorphic transformations. The minima and saddle points are invariants, but the paths of steepest descent change. As an example one usually quotes a certain section from Wilet's booklet [3.3, section 3.3.1] where it is actually shown that an appropriate transform makes a valley into a ridge.

While all these arguments are correct, they do not apply to the proper problem. In fact, chemistry uses similar procedures as modern fission theory to compute the various reaction paths of a chemical system. The same discussion as in nuclear physics went on in chemistry, but was solved there at least 12 years ago, see the book by Mezey [8.1] and the references therein. The relevant line of argument is short enough. Nobody is really interested in valleys. What one needs are low-energy connections between the ground state (a minimum) and the isomeric state (the so-called second minimum), between the isomeric state and the barrier (a saddle point), and between the barrier and the prescission shape (a minimum at the boundary of the deformation space). The connecting paths between invariant points are known to be homotopically equivalent or, in the more general case, they belong to one of the homotopy classes [8.1]. In popular terms, all connections differ from the dynamical path just by some bulges. So it is quite fair to select one of the paths, for example, that computed by steepest descent, as a representative.

Of course, one must not draw conclusions from geometrical peculiarities as for example the big loop in fig. 7.1. On the other hand, it is not correct to claim that lack of topological invariance invalidates the paths computed from the potential energy alone. With these reaction paths, the questions that may be answered are like this: "Which barrier belongs to which prescission shape?" The answers are valuable enough since the height of the barrier affects the probability by which the specific prescission shape is reached. Another example: bifurcation points are generally not invariant. However, the position of a bifurcation is bracketed by two stationary points. Hence one can say whether two reaction paths have two barriers, each one for its own, or just a common one.

It might be beneficial to have a skeleton diagram without geometrical peculiarities. Find a Cayley tree in fig. 8.1. Just the minima appear (○), the barriers (×), the bifurcation points (●), the prescission shapes (+) and their connections (heavy lines).

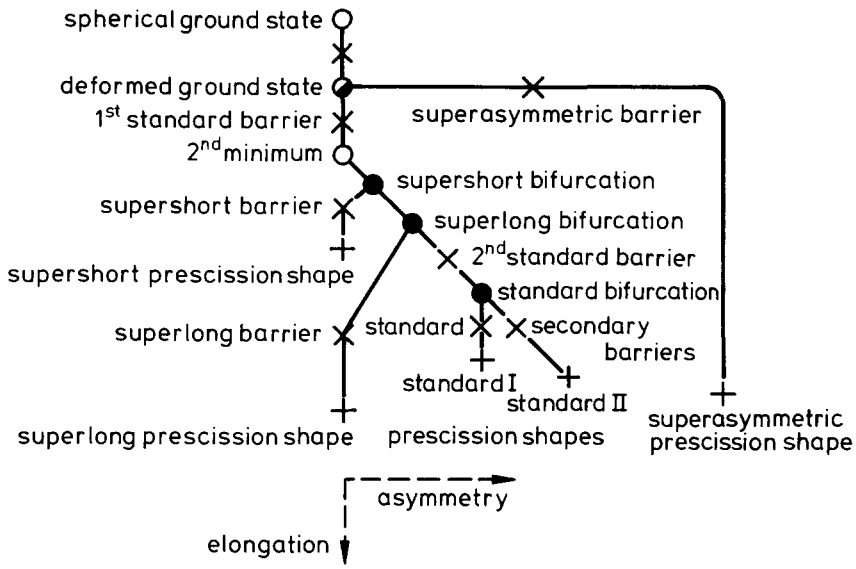

Fig. 8.1. Cayley tree of nuclear fission. Emphasized are distinguished points of the potential energy as minima ○, barriers ×, bifurcation points ● and prescission shapes +. An attempt was made to give to this picture, which is to display topological relations, also some quantitative correctness. For example, the standard II prescission shape is longer than that of the standard I shape. The biggest shortcoming is the position of the superlong barrier, which has much less elongation than this figure suggests.

Compare fig. 8.1 and fig. 7.1. Californium would start to fission from the deformed ground state (*gs*), surmount the first standard barrier, pass the second minimum (*2nd min*) and the bifurcation points, overcome the second standard barrier, and rupture at the standard II prescission shape. At the bifurcation points, and nucleus might decide to enter the supershort or superlong channels and to rupture rather at the supershort or the superlong prescission shapes. According to our calculations, a special role is played by the deformed ground state: it is at the same time the minimum and the bifurcation point to the superasymmetric channel.

Figure 8.1 has most similarity with the (z, l) projection in the bottom-left part of fig. 7.1. So downward motion in fig. 8.1 means an increase of semilength l, while motion to the right refers to the growth of asymmetry z.

Figure 8.1 is intended for general use in low-energy fission. It contains a few features that do not show up in fig. 7.1. There is, for example, no spherical ground state in californium. There is, however, a splitting of the standard channel into standard I, standard II and perhaps even standard III (ordered with respect to asymmetry). Furthermore, no standard secondary barriers can be seen in fig. 7.1. It seems that they matter only for nuclei lighter than californium. Finally in fig. 8.1, the second minimum, the supershort bifurcation, the superlong bifurcation and the second standard barrier are shown to be sequential. But in fig. 7.1 the superlong bifurcation point occurs only after the second standard barrier. The situation shown in fig. 8.1 is nevertheless more typical. In the heaviest actinides (e.g. fermium) the second minimum and the supershort bifurcation point coincide. By contrast, in the lighter actinides (e.g. uranium) the superlong bifurcation point coincides with the second minimum.

For different nuclei different branches of the Cayley tree thrive. For nuclei as light as polonium, the spherical ground state is relevant. The supershort and superasymmetrical channels do not exist. In heavy nuclei such as fermium, the spherical ground state is not available, while all the channels apart from superlong seem to be present.

Besides sheer nonexistence, a fission channel may become inaccessible when its barrier is too high. In californium, for example, the supershort channel does exist. But its barrier is so high that comparatively few events will fission through it. Likewise, the superasymmetric channel can produce only a very small yield.

The quantitative supplement of Cayley trees like fig. 8.1 are tables. In these tables, the distinguished shapes and their energies are recorded. The energies are all calculated using Strutinsky's well known procedure [1.2]. Computational details will be given in ch. 9.

See, for example, the computed ground states in table 8.1. For each nucleus, its coordinates in the five-dimensional space of deformations as introduced in section 2.1 are listed. In addition, the computed and measured binding energies E_{gs} are compared. The comparison reflects the accuracy of Strutinsky's method: around 1 MeV. Furthermore, it is noteworthy that the transition from the spherical to the deformed ground states (cf. fig. 8.1) occurs about where it is expected, namely not too far away from lead. One can localize the transition by the jump of the semilength values from $l \approx 7.3$ to $l \approx 9.0$ fm. The nuclei close to uranium have the celebrated diamond shape, perceptible by the large negative values of the curvature c; the diamonds round out in the heavier nuclei. In the region where the change from spherical to deformed ground states occurs, notably in the actinium isotopes, we find large octupole deformations, identifiable by the large values of the asymmetry coordinates z and s. This too is a known feature [8.2–8.4].

Tables like 8.1 are known for a long time [8.5, 8.6]. However, we need this one since several other tables are based on it. For example, barrier heights are written as excesses over E_{gs}.

The coordinates and heights B_{st} of the standard barrier are presented in table 8.2. Comparison with experimental values demonstrates again agreement within the limits of Strutinsky's method. Note the much worse barriers in fig. 7.1. The difference arises from the use of different shape representations. For fig. 7.1 we took the three-parametrization (2.14), whereas table 8.2 was established with the more flexible five-parametrization (2.1).

All nuclei listed in table 8.2 have a double-humped standard barrier, see figs. 7.1 and 8.1. Table 8.2 presents only the higher one. In the lighter nuclei, the second hump dominates. It is located at larger values of $l \approx 12.6, \ldots, 11.3$ fm. The first hump ($l \approx 10.1, \ldots, 10.7$ fm) excels in the heavier nuclei. That such an exchange occurs, is beyond doubt. However, the precise point in the periodic system is debatable. For comparison we contrast our results with those quoted in [8.7] (where 1st and 2nd are called A and B). It appears from table 8.2 that our exchange occurs at too large mass numbers. This is a weakness one has to face in all computations like this: the limited accuracy of the Strutinsky method is bad enough to shift the point where two energies are equal quite a distance through the periodic table.

Again, tables like 8.2 have been previously published, see, for example, [8.5], but we also need this one for reference.

Table 8.3 is new; a list of superlong barriers. Its best feature is probably the unique compilation of experimental superlong barriers that we owe to H. Nakahara [8.11]. The computed values do not seem to be bad either. Only around thorium do the theoretical and experimental values disagree. The shift of the superlong barrier to larger values of l with increasing mass number is striking. This is opposite to the behavior of the standard barrier. We give no superlong barrier for the heaviest nuclei, although even there rudiments of the superlong channel do exist. However, we found no low-energy connection between the barrier and the superlong prescission shape and therefore judged that in nuclei such as fermium no superlong channel exists [5.9]. We shall discuss data from table 8.3 in section 8.3.

Because of those rudiments it is fair to say that the superlong channel is "broken" in the heaviest nuclei. In contrast we do not see the slightest vestige of the supershort channel in nuclei much lighter

Table 8.1
Ground states, characterized by computed shape parameters l, r, z, c, s and energies E^{t}_{gs}. The shape parameters are introduced in eq. (2.1). They are turned into shapes according to equations (2.3) and (2.9–2.13). Experimental binding energies E^{e}_{gs} are taken from [4.6]. The table also lists all the nuclides for which we examined the fission channels. Details of the computation are explained in ch. 9

Nucleus	l (fm)	r (fm)	z (fm)	c (fm)	s (fm)	E^{t}_{gs} (MeV)	E^{e}_{gs} (MeV)
^{210}Po	7.3	7.3	0.0	−7.2	0.0	1644.4	1645.2
^{213}At	7.3	7.3	0.2	−7.2	0.1	1659.2	1659.3
^{225}Ra	7.4	7.5	0.1	−7.2	0.1	1724.4	1725.2
^{227}Ra	7.3	7.5	0.1	−7.2	0.1	1735.3	1736.2
^{226}Ac	8.8	7.2	1.1	−8.2	0.5	1728.8	1730.2
^{227}Ac	9.0	7.2	1.0	−8.1	0.3	1735.6	1736.7
^{228}Ac	9.0	7.1	0.5	−7.8	0.2	1740.9	1741.8
^{232}Th	9.1	7.1	0.3	−7.5	0.1	1765.9	1766.7
^{233}Pa	9.1	7.2	0.0	−8.0	0.0	1771.6	1772.0
^{236}U	9.1	7.1	0.6	−7.7	0.2	1789.6	1790.4
^{234}Np	9.1	7.1	0.7	−7.8	0.2	1775.0	1776.0
^{236}Np	9.1	7.1	0.6	−7.4	0.2	1787.6	1788.7
^{239}Np	9.2	7.1	0.5	−7.6	0.2	1806.5	1807.0
^{236}Pu	9.2	7.2	0.1	−7.9	0.1	1787.3	1788.4
^{238}Pu	9.1	7.1	0.2	−7.2	0.1	1800.3	1801.3
^{240}Pu	9.1	7.1	0.3	−7.2	0.1	1812.7	1813.5
^{242}Pu	9.0	7.1	0.0	−7.3	0.0	1824.5	1825.0
^{240}Am	9.0	7.1	0.2	−6.6	0.1	1810.2	1811.3
^{243}Am	9.0	7.1	0.0	−6.4	0.0	1829.5	1829.9
^{245}Am	9.0	7.1	0.3	−6.6	0.1	1841.0	1841.3
^{242}Cm	9.1	7.1	0.1	−6.4	0.0	1822.2	1823.4
^{244}Cm	9.1	7.1	0.0	−6.5	0.0	1835.1	1835.9
^{248}Cm	9.1	7.1	0.3	−6.4	0.1	1858.9	1859.2
^{252}Cf	8.9	7.1	0.1	−4.8	0.0	1881.3	1881.3
^{255}Es	8.8	7.1	0.1	−5.6	0.0	1898.0	1896.7
^{256}Fm	8.8	7.1	0.0	−5.6	0.0	1903.4	1902.6
^{258}Fm	8.8	7.2	0.1	−5.7	0.0	1914.8	
^{259}Fm	8.7	7.1	0.1	−5.2	0.0	1919.8	
^{259}Md	8.8	7.2	0.1	−5.5	0.0	1918.8	
^{260}Md	8.7	7.2	0.1	−4.7	0.0	1924.1	
^{258}No	8.8	7.2	0.1	−5.3	0.0	1911.9	1911.2
^{260}[104]	8.7	7.2	0.1	−5.3	0.0	1918.6	1918.2
~~^{272}[108]~~	~~8.6~~	~~7.3~~	~~0.2~~	~~−2.7~~	~~0.0~~	~~1982.8~~	

than californium. The characteristics of the supershort barrier are listed in table 8.4. The supershort barriers are lower than the highest standard barriers, except for californium, since in these heavy nuclei the first standard hump is dominant. The second hump, however, still exists. Its features are also collected in table 8.4. We shall take advantage from this juxtaposition in section 8.3.

Barrier tables can be novel when hitherto unknown barriers are produced. But table 8.5 of

Table 8.2
Standard barriers B_{st}, otherwise similar to table 8.1. Experimental values (e) stem from [8.7]

Nucleus	l (fm)	r (fm)	z (fm)	c (fm)	s (fm)	B^t_{st} (MeV)	B^e_{st} (MeV)
^{210}Po	12.4	4.2	3.1	4.7	−1.2	23.8 (2nd)	24.4
^{213}At	12.6	3.9	2.6	6.0	−1.5	20.8 (2nd)	19.8
^{225}Ra	11.2	5.2	3.1	1.4	−0.4	8.1 (2nd)	6.5 ± 0.5
^{227}Ra	11.2	5.4	2.9	0.9	−0.4	7.4 (2nd)	8.0
^{226}Ac	11.3	5.3	3.1	0.8	−0.4	7.8 (2nd)	8.0
^{227}Ac	11.3	5.3	2.9	1.0	−0.3	7.3 (2nd)	7.3
^{228}Ac	11.3	5.4	2.8	0.6	−0.4	7.5 (2nd)	7.2
^{232}Th	11.2	5.4	2.9	0.5	−0.4	7.2 (2nd)	6.2 ± 0.2 (2nd)
^{233}Pa	11.3	5.4	2.8	0.8	−0.4	7.6 (2nd)	6.1 (1st)
^{236}U	11.3	5.0	3.0	1.8	−0.9	6.7 (2nd)	5.6 ± 0.2 (1st)
^{234}Np	11.6	5.2	2.9	1.1	−0.6	6.5 (2nd)	5.5 ± 0.2 (1st)
^{236}Np	11.2	5.3	3.2	0.8	−0.5	6.6 (2nd)	5.8 ± 0.2 (1st)
^{239}Np	11.3	5.3	3.2	0.9	−0.6	7.3 (2nd)	5.9 ± 0.2 (1st)
^{238}Pu	11.6	5.3	2.8	1.0	−0.5	6.4 (2nd)	5.5 ± 0.2 (1st)
^{240}Pu	11.2	5.3	3.2	0.8	−0.6	7.0 (2nd)	5.6 ± 0.2 (1st)
^{240}Am	11.4	5.3	3.2	0.8	−0.5	7.2 (2nd)	6.5 ± 0.2 (1st)
^{243}Am	11.4	5.3	3.2	0.8	−0.5	7.4 (2nd)	5.9 ± 0.2 (1st)
^{245}Am	11.3	5.4	3.0	0.8	−0.5	6.8 (2nd)	5.9 ± 0.2 (1st)
^{242}Cm	10.5	6.5	0.3	−3.5	0.0	6.6 (1st)	5.8 ± 0.4 (1st)
^{244}Cm	10.4	6.5	0.5	−3.0	0.2	6.7 (1st)	5.8 ± 0.2 (1st)
^{248}Cm	10.2	6.5	0.3	−1.9	0.0	6.5 (1st)	5.7 ± 0.2 (1st)
^{252}Cf	10.1	6.6	0.0	−2.2	0.0	6.9 (1st)	5.3 (1st)
^{255}Es	10.4	6.5	0.5	−2.2	0.1	7.5 (1st)	
^{256}Fm	10.3	6.6	0.4	−2.8	0.1	7.4 (1st)	
^{258}Fm	10.4	6.5	0.5	−2.3	0.1	6.8 (1st)	
^{259}Fm	10.6	6.5	0.4	−1.8	0.1	7.3 (1st)	
^{259}Md	10.5	6.8	0.3	−3.9	0.1	6.9 (1st)	
^{260}Md	10.7	6.6	0.2	−2.2	0.0	7.2 (1st)	
^{258}No	10.6	6.8	0.4	−4.1	0.1	7.4 (1st)	
^{260}[104]	10.5	6.8	0.3	−4.2	0.1	7.2 (1st)	
^{272}[108]	10.6	6.8	0.3	−4.1	0.1	5.5 (1st)	

prescission shapes even introduces a new concept. Prescission shapes are extrema of the potential energy too, but in general they are not stationary points as they are located on the border of deformation space. We fix this border by the radius r of the neck: $r > 1.5$ fm is the condition for a shape to lie within the deformation space. As soon as the radius becomes smaller, we assume that rupture is finished and fragments are born. We do not need this condition for most superlong prescission shapes as we find them in minima (4th min in fig. 7.1). See section 9.3 for a justification.

Table 8.5 is the foundation of most of the results involving random neck rupture in low-energy fission. This table contains the raw data for the computation of yields and total kinetic energies as presented in the sections 7.2 and 7.3. They will once more prove their usefulness in section 8.2. Table 8.5 presents the geometrical data of the prescission shape (l, r, z, c, s) and the *energy of descent* E_{des}

Table 8.3
Superlong barriers B_{sl}, otherwise similar to table 8.1. Most experimental values are quite new. They are referenced in the last column. This table contains a few predictions concerning important nuclei. For example, no experimental value of the superlong barrier of uranium seems to be known. There is data by Straede et al. {eq. (3) in [8.12]}, but it is not sufficient

Nucleus	l (fm)	r (fm)	z (fm)	c (fm)	s (fm)	B^{t}_{sl} (MeV)	B^{e}_{sl} (MeV)	Reference
^{210}Po	11.4	5.1	0.0	1.9	0.0	21.6	21.3	[8.8]
^{213}At	11.4	5.1	0.1	1.3	0.0	18.8	17.2	[8.8]
^{225}Ra	12.2	5.2	0.4	−0.5	0.0	12.6	6.7 ± 0.5	[8.9]
^{227}Ra	11.8	5.2	0.1	−0.1	0.0	13.0	9.0	[8.9]
^{226}Ac	12.1	5.3	0.2	0.0	0.0	11.6	9.2	[8.9]
^{227}Ac	11.8	5.2	0.2	−0.1	0.0	11.2	8.4–8.5	[8.8, 8.9]
^{228}Ac	11.8	5.2	0.6	−0.3	0.0	12.2	9.2	[8.9]
^{232}Th	12.7	5.6	0.0	0.0	0.0	11.8	8.5–8.7	[7.6]
^{233}Pa	12.6	5.5	1.3	−1.7	0.0	11.6	9.0	[8.11]
^{236}U	12.4	5.5	0.7	−1.3	0.0	10.9		
^{234}Np	12.6	5.5	1.0	−1.8	0.0	9.7	6.8	[8.11]
^{236}Np	12.5	5.5	0.7	−1.8	0.0	10.4	7.4	[8.11]
^{239}Np	12.4	5.5	0.5	−0.9	0.1	10.2	8.2	[8.11]
^{238}Pu	12.5	5.5	1.0	−1.2	0.2	9.0	7.6 ± 0.2	[8.11]
^{240}Pu	12.5	5.5	0.6	−1.2	0.0	9.2		
^{240}Am	12.5	5.5	0.7	−1.4	0.0	9.0	8.7 ± 0.2	[8.11]
^{243}Am	12.5	5.5	1.0	−0.8	0.0	8.7	8.4 ± 0.2	[8.11]
^{245}Am	12.5	5.6	0.7	−0.7	0.0	8.7	8.5 ± 0.2	[8.11]
^{242}Cm	12.5	5.5	1.0	−1.3	0.0	7.5	8.0 ± 0.4	[8.11]
^{244}Cm	12.5	5.5	0.9	−0.9	0.1	8.0	8.1 ± 0.2	[8.11]
^{252}Cf	12.6	5.5	0.0	0.6	0.0	7.5		

defined as the difference between the potential energies of the ground state (table 8.1) and the prescission shape. Notice that it costs energy to put astatine into its prescission shapes, whereas in all other nuclei energy is gained. Table 8.5 is incomplete in so far as it lists the standard I and standard II prescission shapes only for nuclei around plutonium. Standard I/II splitting is in fact most prominent in the plutonium isotopes. Nevertheless, sample calculations suggest that the splitting also exists in astatine, actinium and einsteinium. The table is overcomplete as it contains channel probabilities p^{e}_{c}. We explained in section 7.2 how they were obtained. They will be helpful to judge the relative importance of the various prescission shapes.

8.2. Kinetic energy fluctuations

As a first application of the tables 8.1 to 8.5 we wish to compute TKE fluctuations in low-energy fission. The procedure rests on the formulas derived in section 6.3; see section 6.4 for a tutorial. Only the quantities that enter eqs. (6.34) have to be fixed with some care, as 10 MeV is now a large chunk of energy.

We obtain ΔU from (6.7). E_{des} can be read from table 8.5 and the relevant barrier B from tables 8.2–8.4. The semilength l at rupture can be taken directly from the prescission shape table 8.5. The length of descent Δl is simply the difference between the l which can be found in table 8.5 and the

Table 8.4
Supershort and second standard barriers. The table is organized as table 8.1

Nucleus	Barrier	l (fm)	r (fm)	z (fm)	c (fm)	s (fm)	B^t (MeV)
^{252}Cf	supershort	12.6	3.8	0.0	11.1	0.0	6.6
	standard (2nd)	12.0	5.5	2.8	0.6	−0.3	5.7
^{255}Es	supershort	12.4	4.4	0.1	10.8	0.0	5.2
	standard (2nd)	11.8	5.5	2.6	0.9	−0.3	5.4
^{256}Fm	supershort	11.7	5.2	0.1	6.5	0.0	3.8
	standard (2nd)	12.0	5.5	2.8	0.4	−0.3	4.4
^{258}Fm	supershort	11.7	5.2	0.0	6.5	0.0	3.2
	standard (2nd)	12.0	5.5	2.7	0.6	−0.4	4.0
^{259}Fm	supershort	11.7	5.3	0.1	5.8	0.0	2.9
	standard (2nd)	12.2	5.4	2.9	0.7	−0.5	4.1
^{259}Md	supershort	11.8	5.1	0.0	7.5	0.0	2.9
	standard (2nd)	12.3	5.4	2.9	0.7	−0.5	3.1
^{260}Md	supershort	11.7	5.2	0.0	6.5	0.0	2.4
	standard (2nd)	12.0	5.5	2.9	0.5	−0.4	3.2
^{258}No	supershort	11.8	5.1	0.0	7.3	0.0	2.9
	standard (2nd)	11.9	5.6	2.3	0.6	−0.3	2.7
^{260}[104]	supershort	11.5	5.5	0.1	4.5	0.0	1.4
	standard (2nd)	12.4	5.4	2.9	0.5	−0.5	1.2
^{272}[108]	supershort	12.5	5.4	0.2	4.3	0.0	−2.6
	standard (2nd)	12.9	5.5	2.3	0.8	−0.6	−2.0

respective barrier tables 8.2–8.4. For example, Δl for superlong is the prescission l of superlong minus the l of the superlong barrier. But be careful with the lengths of descent for the standard channels: first, both standards, I and II, have the same main barrier since they fork only after the second standard barrier (see fig. 8.1). The differences in Δl are caused only by the different lengths of the prescission shapes. Second, the "standard secondary barriers" (cf. fig. 8.1) are never prominent structures. In contrast, the second standard barrier is always high enough to withhold a nucleus for some time. Therefore, free sliding starts beyond the second standard barrier even if the first barrier is somewhat higher. You can find the second standard barrier data either in table 8.2 or table 8.4.

The Coulomb repulsions V_{Cou} come out as byproducts when the total kinetic energies $\overline{\mathrm{TKE}}^t$ of table 7.1 were computed: one just has to subtract the nuclear attraction (4.13) to obtain the pure V_{Cou}. This means that mass fluctuations were taken into account. See, however, section 6.4 for a simpler recipe to get V_{Cou}.

Inserting these values into (6.34) produces the TKE deviations σ_E^t in table 8.6 where they are compared with the experimental results σ_E^e.

Agreement is agreeable especially in the central region with nuclei ranging from thorium to einsteinium. Note, in particular, that the superlong σ_E do not differ much from the σ_E of the standard channel, both in experiment and theory. This is in marked contrast to the behavior of the mass deviations σ_A in table 7.1. Due to the simplicity of our theory, we can explain this fact: the dominating term in (6.33) is $\sigma_{E,c}^2$. It contains the factor $V_{\mathrm{Cou}}\,\Delta l/l$. Now V_{Cou}/l is relatively large in the standard channel, but its Δl is quite small. In superlong, however, Δl is large, but V_{Cou}/l is so small that it partly compensates for the size of Δl.

Serious discrepancies occur for the standard channel of fermium and for the lightest systems astatine

Table 8.5

Prescission shapes. E_{des} denotes the energy liberated on *descent from the ground state to scission*. For reasons discussed in section 9.1 we guess that the computed values E^{t}_{des} are too large, in particular for the heavy nuclei. The channel probabilities p^{e}_{c} were obtained either from the mass distributions shown in fig. 7.3 as described in section 7.2 or from the references quoted in the last column

Nucleus	Channel	l (fm)	r (fm)	z (fm)	c (fm)	s (fm)	E^{t}_{des} (MeV)	p^{e}_{c} (%)	References
^{213}At	standard	15.2	1.5	2.1	12.4	−1.7	−15.6	0.8	fig. 7.3
	superlong	17.5	1.5	0.5	12.5	0.1	−6.3	99.2	
^{227}Ac	standard	15.6	1.5	1.1	11.8	−1.5	5.8	46	fig. 7.3
	superlong	18.2	2.2	0.0	7.2	0.0	6.9	54	
^{232}Th	standard I	15.5	1.5	0.2	20.2	−1.6	9.6	29.2	[7.6]
	standard II	16.3	1.5	0.3	13.4	−1.6	8.8	69.6	
	superlong	19.4	2.1	0.0	5.4	0.0	7.2	1.2	
^{236}U	standard I	15.4	1.5	0.3	22.5	−1.3	12.7	16.9	[7.11]
	standard II	16.4	1.5	1.3	16.0	−1.4	14.8	83.0	
	superlong	21.2	1.8	0.0	5.2	0.0	15.2	0.1	
^{240}Pu	standard I	15.8	1.5	0.6	21.0	−1.1	16.8	26.2	[7.7]
	standard II	16.6	1.5	0.3	17.2	−1.7	18.7	73.8	
	superlong	21.4	1.9	0.0	4.4	0.0	23.1		
^{252}Cf	supershort	14.3	1.5	0.0	31.2	0.0	12.4		
	standard I	16.6	1.5	−0.4	18.5	−1.2	23.6	8.5	[6.13, 6.14]
	standard II	17.5	1.5	0.8	18.3	−1.4	29.1	62.0	
	standard III							27.7	
	superasymmetric	18.2	1.5	4.2	12.0	−1.7	18.3	0.5	
	superlong	21.0	2.6	0.3	2.5	−0.1	27.8	1.3	
^{255}Es	supershort	14.9	1.5	0.1	23.4	−0.2	19.0	13	fig. 7.3
	standard	17.2	1.5	0.3	12.3	−1.3	24.3	87	
^{258}Fm	supershort	15.0	1.5	0.2	22.4	−0.1	22.5	50	[8.13]
	standard	17.2	1.5	0.2	12.1	−1.3	26.6	50	
^{259}Fm	supershort	14.9	1.5	0.0	18.1	0.0	24.7	73	fig. 7.3
	standard	17.6	1.5	0.2	11.2	−1.4	28.5	27	
^{272}[108]	supershort	17.4	1.5	0.3	8.1	−0.2	61.7		
	standard	22.7	1.7	0.8	5.7	−1.7	67.9		

and actinium. The disagreement in the light systems, by the way, still reflects the reason for the two cases in eq. (6.14): had we fixed $E^{*}_{s} = K_{s} = 0.25\,\Delta U$ for all systems, similar differences would also show up in uranium. This exhibits the fact that a two-step function such as (6.14) is too primitive and that a continuous variation of $E^{*}_{s}/\Delta U$ and $K_{s}/\Delta U$ with mass number A_{cn} is desirable.

Lazarev established a systematics of TKE variances [8.15, 8.16]: at first they grow smoothly with system size, from $\sigma^{2}_{E} \approx 60$ for $A_{cn} \approx 230$ to $\sigma^{2}_{E} \approx 130$ for $A_{cn} \approx 250$. Then, suddenly, for some fermium isotopes, σ^{2}_{E} as large as 600 are reached. Especially those nuclei, about which we know that the standard and supershort channels contribute with about equal rates, give the largest values, namely ^{258}Fm and ^{259}Fm.

When writing his paper Lazarev had no idea on multichannel fission. Hence he gave only the total TKE variances. If they come from two contributors, say the standard channel with probability p_{st} and the supershort channel with p_{ss}, the superposition formula is

$$\sigma^{2}_{E} = p_{ss}\sigma^{2}_{E,ss} + p_{st}\sigma^{2}_{E,st} + p_{ss}p_{st}(\overline{\mathrm{TKE}}_{ss} - \overline{\mathrm{TKE}}_{st})^{2}\,. \tag{8.1}$$

Insertion of values taken from the tables 7.1, 8.5 and 8.6 typically delivers $\sigma_E^2 \approx 220$ for the heaviest actinides. This aims in the right direction, but it is still too small. However, it seems that Serdyuk and co-workers [6.10] have solved just this problem by a more realistic and thus more complex model.

8.3. *The superlong and the supershort barriers*

The next application of the tables 8.1 to 8.5 is to understand the behavior of the channel probabilities p_c as shown in fig. 7.5a. So why is superlong's p_{sl} dominant for light nuclei while it dwindles with increasing A_{cn}? And why is supershort never able to push standard into oblivion? These questions can be answered by the height of certain barriers.

However, first the relations between the bifurcation points and the barriers must be clear. Imagine, for simplicity, only two fission channels, one bifurcation point and several barriers which may be positioned before or behind the bifurcation, cf. fig. 8.1.

Table 8.6

Fluctuations of the total kinetic energy in low-energy fission. This table is organized as table 6.1: as input we need the excitation energy E_s^* at scission, the Coulomb energy V_{Cou} of repulsion between the nascent fragments, the potential-energy difference ΔU [its relation to E_{des} is given by eq. (6.7)], the distance of descent Δl and the semilength l of the prescission shape. Values of σ_E^e with a $\approx$ symbol were found by interpretation of measured $\sigma_E(A)$ functions, see that in fig. 8.7. For example, $\sigma_E(A \approx 140)$ was taken as the TKE deviation σ_E^e in the standard channel. The other values were determined by deconvolution of data (see sections 7.2 and 8.5). They are more accurate

Nucleus	Channel	E_s^* (MeV)	V_{Cou} (MeV)	ΔU (MeV)	Δl (fm)	l (fm)	σ_E^l (MeV)	σ_E^e (MeV)	References
^{213}At	standard	10.0	183	5.2	2.6	15.2	11	≈6	[7.4]
	superlong	14.7	172	12.5	6.1	17.5	15	≈7	
^{227}Ac	standard	15.8	201	13.1	4.3	15.6	13	≈7	[5.27]
	superlong	13.7	181	18.1	6.4	18.2	12	≈8	
^{232}Th	standard I	9.2	208	16.8	4.3	15.5	10.3	9.6	[7.6]
	standard II	8.9	197	16.0	5.1	16.3	11.3	7.7	
	superlong	6.5	175	17.2	6.7	19.4	9.8	9.4	
^{236}U	standard I	7.3	219	19.2	4.1	15.4	9.0	8.1	[7.11]
	standard II	8.1	205	21.3	5.1	16.4	9.5	7.6	
	superlong	8.2	168	21.7	8.8	21.2	10.5	8.1	
^{240}Pu	standard I	6.4	224	16.8	4.6	15.8	10.6	6.5	[8.13]
	standard II	7.1	213	18.7	5.4	16.6	11.0	9.7	
	superlong	8.7	174	23.1	8.9	21.4	10.6		
^{252}Cf	supershort	3.1	268	12.4	1.7	14.3	5.6		[6.13]
	standard I	5.8	236	23.6	4.6	16.6	9.8	7.4	
	standard II	7.2	221	29.1	5.5	17.5	9.8	8.3	
	standard III							9.5	
	superasymmetric							5.5	
	superlong	6.8	192	27.8	8.4	21.0	11.1	7.7	
^{255}Es	supershort	6.2	264	25.0	2.5	14.9	6.6	≈12	[5.8]
	standard	7.6	232	30.9	5.4	17.2	10.3	≈11	
^{258}Fm	supershort	5.6	268	22.7	3.3	15.0	8.8	11	[8.14]
	standard	6.5	236	26.6	5.2	17.2	10.3	19	
^{272}[108]	supershort	15.2	276	61.7	6.8	17.4	12		
	standard	16.7	212	67.9	12.1	22.7	12		

Two situations may occur:

(i) The highest barriers of the channels lie behind the bifurcation, and hence the channels have separate barriers.

(ii) There is only one highest barrier for both channels. It is located before the bifurcation. Behind the bifurcation lower secondary barriers may be met.

The first situation is shown in fig. 7.1. Pick the superlong and standard channels for example: the first standard barrier is quite low, bifurcation takes place close to the second minimum, and after that the huge second standard and superlong barriers rise. [Actually, situation (i) applies rather to nuclei somewhat lighter than californium, compare tables 8.2 and 8.3.]

Situation (ii) is typical for the relation between the supershort and the standard channels. In the heaviest actinides, where both channels exist, the first standard barrier is highest (see table 8.2), and the bifurcation takes place close to the second minimum, see fig. 8.1. Behind the bifurcation, lower barriers still have to be passed. All nuclei fissioning via the supershort channel must climb the supershort barrier, and the standard fissioners must surmount the second standard barrier. (The "secondary standard barriers", being in fact third barriers, can be neglected for this case.)

The two situations cause different dynamics. Let us first consider a single bifurcation point. It divides the flux of probability, and we expect that the division is about equal. Here "equal" means less than one order of magnitude difference. Inertia can drive, for example, 90% of the flux into one channel and leave only 10% for the other. Now, if there are high barriers behind the bifurcation, the probability bounces back. The nucleus returns to the second minimum and must undertake another attempt. If one of the barriers is higher, the nucleus must ride many more attacks against it before penetration succeeds. So we understand that *situation (i) allows for channel probabilities that are different by orders of magnitudes.*

Situation (ii) can produce only differences of one order of magnitude. After the nucleus has overridden the primary barrier, the smaller ones are like pebbles. We expect the largest effects in spontaneous fission.

As mentioned above, situation (i) is typical for the superlong–standard bifurcation, while situation (ii) applies to the supershort–standard branching. Hence we understand now why the superlong and standard channels can displace each other, whereas supershort and standard must coexist, as suggested in fig. 7.5a.

The battle for dominance between superlong and standard is decided, at least for the order of magnitude, by the changing heights B_{sl} and B_{st} documented in the tables 8.2 and 8.3. We have plotted the barrier-height differences in fig. 8.2. The potential-energy calculations show that B_{sl} is lower for lighter nuclei, but then with increasing mass the standard barrier B_{st} becomes smaller. This generates those large differences $B_{sl} - B_{st}$ shown in fig. 8.2 for $A_{cn} \approx 230$. The differences decrease again in the heavier nuclei. Comparison with experimental values shows that the theory is right but exaggerates. In particular, the point of equality is shifted from $A_{cn} \approx 224$ to $A_{cn} \approx 217$. But such shifts are unavoidable with the Strutinsky method, as we pointed out in section 8.1.

The way by which the experimental superlong barriers were found is illustrated in fig. 7.7. First some yields have to be measured at several excitation energies E^*. Then one collects, for every E^*, the yield at mass symmetry and at low total kinetic energies to determine, as indicated by eqs. (7.1) and (7.5), the probability $p_{sl}(E^*)$ of the superlong channel. These data are finally fitted by the function

$$p_{sl}(E^*) = \frac{W_{sl}}{1 + \exp[2\pi(B_{sl} - E^*)/\hbar\omega_{sl}]} \tag{8.2}$$

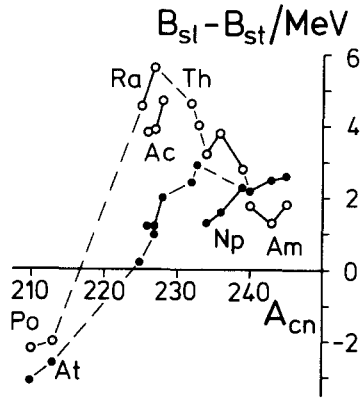

Fig. 8.2. Excess of the superlong barrier B_{sl} over the standard barrier B_{st} as a function of the mass number A_{cn} of the fissioning nucleus. Computational results are indicated by the hollow circles, measured ones by the full dots. Isotopes of an element are connected by massive lines. Symbols of some relevant elements are added. The dashed lines are there to indicate the major trends. For the sake of transparency not all the data, which can be obtained from the tables 8.2 and 8.3, are displayed.

with parameters W_{sl}, B_{sl} and $\hbar\omega_{sl}$. For photofission of ^{232}Th Piessens and co-workers obtained a W_{sl} of a few per cent, B_{sl} as 8.5–8.7 MeV (cf. table 8.3) and $\hbar\omega_{sl}$ as 0.33–0.39 MeV [7.6, 8.10].

A more advanced method to isolate the channel probabilities will be presented in section 8.5. Similar methods were developed by Nakahara and colleagues [8.11]. For photofission by bremsstrahlung a convolution has to be performed [7.6] before B_{sl} can be extracted.

The struggle between the supershort and standard channels seems to be influenced by the secondary barriers that are listed in table 8.4. To facilitate comparison with experimental materials, we computed again the differences $B_{sl}(2nd) - B_{ss}$ and used them to establish table 8.7. The table is arranged according to increasing differences. One recognizes that the experimental supershort probabilities p^e_{ss} increase as these differences grow, with ^{256}Fm as the only possible exception.

Both examples, that in fig. 8.2 and that in table 8.7, represent what is called "monotonicity": the Strutinsky method is not good enough to calculate potential energies with high accuracy, but one can follow certain systematic trends and compare them with measurements.

Table 8.7

The difference of the two small barriers behind a bifurcation point and the probability p^e_{ss} of fission via the supershort channel. The value quoted for ^{256}Fm results from a very crude estimate based on data presented by Unik et al. [5.8]. It should therefore be considered with caution. A similar remark applies to ^{259}Fm as this is data from a pioneering experiment

Nucleus	$[B_{st}(2nd) - B_{ss}]^t$ (MeV)	p^e_{ss} (%)	References
^{252}Cf	−0.9	0	[6.13]
^{260}[104]	−0.2	0	[7.9]
^{258}No	−0.2	5	[7.9]
^{259}Md	0.2	12	[7.9]
^{255}Es	0.2	13	[5.8]
^{256}Fm	0.6	≈10	[5.8]
^{258}Fm	0.8	50	[7.9]
^{260}Md	0.8	58	[7.9]
^{259}Fm	1.2	≈73	[7.10]

8.4. The standard splitting

The systematics of low-energy fission can be understood in terms of the standard, superlong and supershort channels. Also from the computational point of view, these three channels are easily found and discriminated. They are also surprisingly stable if important parameters in the microscopic calculations (see ch. 9) are varied or the representation of the surface (see ch. 2) is changed. Therefore, there is no doubt on the reality of these channels, and their computed characteristics such as barriers, bifurcations and prescission shapes should be valid, at least as approximations.

However, standard fission is almost always prevailing and hence experimenters have considered it favorably. The result of such an inspection can be seen in fig. 8.3. We perceive *two components*, one around mass number $A \approx 135$ and TKE ≈ 190 MeV (the right-hand side hill), the other close to $A \approx 142$ and TKE ≈ 175 MeV (left-hand side). The first, with the smaller asymmetry, is *standard I*. It is most prominent in ^{242}Pu. The second, *standard II*, appears best in ^{236}Pu.

The standard splitting is no speciality of the plutonium isotopes. First evidence for two standard channels in ^{236}U was published in [7.11]. It is nowadays also proven that two standards exist in ^{232}Th [7.6]. Taking suitable data for ^{213}At is more difficult, however the available material is perspicious enough [7.4, 7.5].

In all these recent experiments the standard component was decomposed as indicated by eq. (7.1). Moreover, it was demonstrated that the channel probabilities of the two standard channels vary a lot when the external parameters of the reaction are changed only a little [1.8]. However, a mere decomposition of the standard contribution has long been pursued. Data are available for many more nuclei, see [8.17] and [8.11]. One can discover both standard components also in the yield $Y(A)$ of einsteinium shown in fig. 7.3. Here the theorists (we) were too lazy to separate standard I from standard II. This is the cause of the poor description of the measured yield at $A \approx 135$. The neglect of the standard splitting can also be seen in the slight deepening of the theoretical $\overline{\mathrm{TKE}}(A)$ at the $A \approx 135$ line, as standard I gives rise to high kinetic energies.

The standard I prescission shapes are not only less asymmetric than those of standard II but generally also shorter (see table 8.5). Therefore, standard I prescission shapes make fragments with less deformation. This must show up in the neutron multiplicities. Refer to fig. 7.4. The effects of the standard splitting on the neutron multiplicities are outlined in the prediction for thorium: the reduction of emission is best seen in the total neutron multiplicity, displayed by the dashed line. However, the simple neutron multiplicity also (full line) exhibits the reduction by a kink at $A = 97$; this is in ^{232}Th the complement of $A = 135$. One may reject this as a speculation since no experimental data are at hand for thorium. However, for ^{236}U, measurements and calculations are available, and in both the effects of the standard splitting can be seen.

Hence the standard I and II channels occur in all preactinides and actinides. The standard splitting can be seen in the mass and kinetic-energy distributions and in the neutron multiplicities.

A phenomenon that has attracted much attention during the past ten years [6.16], "true cold fragmentation", is a side effect of the standard splitting. Loosely spoken, "cold fragmentation" at low excitation energies is nothing but the tail of the TKE fluctuations discussed in ch. 6: even in standard fission, prescission shapes may sometimes become very short. The newborn fragments are almost spherical and stay therefore *cold*. Due to the large Coulomb repulsion these fragments attain high kinetic energies. Note the difference to scission via the supershort channel where even on the average cold fragments are produced. Cold fragmentation via the standard channels, in contrast, is a feature of rare fluctuations. By *true* cold fragmentation one understands TKE fluctuations that exhaust the

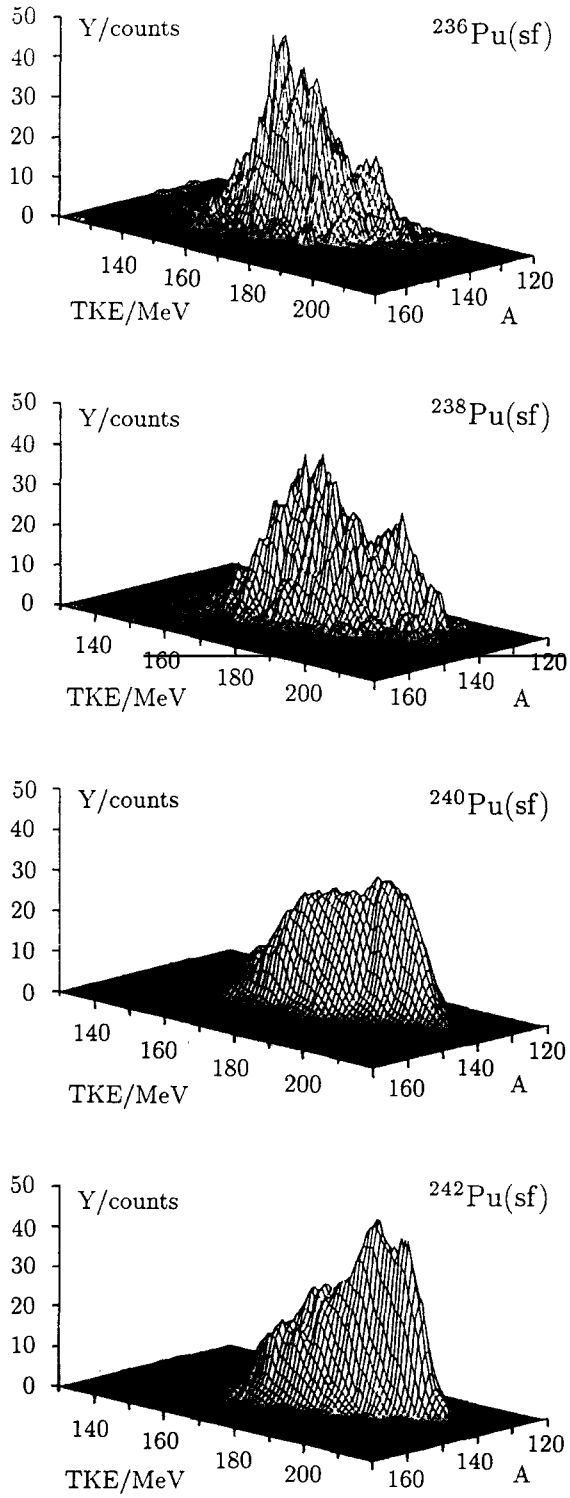

Fig. 8.3. Mountain plot of the fission yields from various plutonium isotopes over the plane of fragment mass number A and total kinetic energy TKE. The data is taken from [7.8].

Q-value of the partition. Most remarkably, true cold fragmentation only happens in a certain range of fragment mass numbers. For nuclei from thorium to californium this range was found invariably around $A \approx 130$ and, of course, around $A_{cn} - A$. An example is shown in fig. 8.4. The full, ragged line represents the limit set by the Q-value, and the dotted and dashed lines give the upper limits of the TKE fluctuations as measured in different experiments. One can see that these fluctuations touch the Q-value only at $A = 102 \pm 5$. This observation is explained by the standard I/II splitting: standard I produces even on the average the shorter prescission shapes. But its TKE fluctuations do not differ appreciably from those of standard II, see table 8.6. Therefore, it is almost trivial that the fluctuations of standard I press to the Q-values whereas those of standard II do not.

The display of the theoretical results in fig. 8.4 needs some explanation. We represented the contributions from the standard channels (st I and st II) and from the superlong channel (sl) by products of Gaussians

$$\exp\left(-\frac{(A-\bar{A})^2}{2\sigma_A^2}\right)\exp\left(-\frac{[\mathrm{TKE}-\overline{\mathrm{TKE}}(A)]^2}{2\sigma_E^2}\right). \tag{8.3}$$

The Coulomb effect is taken into account by

$$\overline{\mathrm{TKE}}(A) := \frac{A(A_{cn}-A)}{\bar{A}(A_{cn}-\bar{A})}\,\overline{\mathrm{TKE}}\,. \tag{8.4}$$

With these simplifications of (6.1), (7.5) and (7.6) we drew contours for every channel separately. The function (8.3) has the value 1 for $A = \bar{A}$ and $\mathrm{TKE} = \overline{\mathrm{TKE}}$. The averages $\bar{A}$ and $\overline{\mathrm{TKE}}$ were taken from table 7.1 and appear in fig. 8.4 as stars. On the ellipsoidal lines, the function (8.3) takes the value $\exp(-\frac{1}{2})^2$. Thus the ellipsoids display directly the deviations σ_A^t and σ_E^t presented in the tables 7.1 and 8.6.

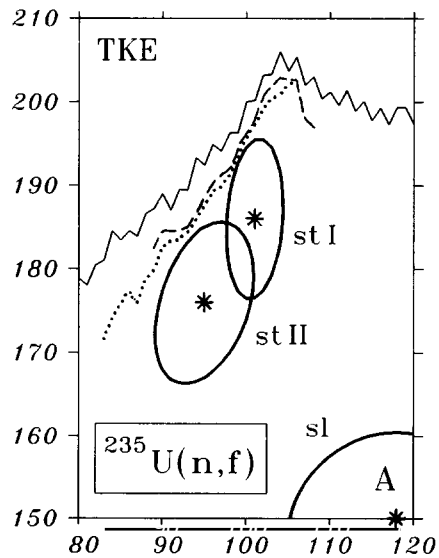

Fig. 8.4. Cold fragmentation. Q-values (full zigzag line) according to Wapstra and Audi [4.6] and the limits of the yield $Y(A, \mathrm{TKE})$ for high TKE as measured by Signarbieux et al. [8.19–8.20] (dashed line) and Clerk et al. [8.19, 8.21] (dotted line). The theoretical results are shown as the ellipsoidal contours around the stars and refer to the standard channels (st I, st II) and to superlong (sl), as explained in the text.

The evidence produced up to now shows only that two different standard prescission shapes exist. But can we also learn how these shapes are reached? Where, for example, is the bifurcation point at which the two standard channels separate and what is the situation of the barriers? The answers are contained in fig. 8.1: the *standard bifurcation* takes place behind the second *standard barrier*. Behind the bifurcation low *standard secondary barriers* are located. This is *situation* (*ii*) as introduced in section 8.3. Thus the standard splitting should behave as the standard–supershort bifurcation. Evidence for this exists, but before we can produce it, we must issue a disclaimer.

The computational separation of standard I and II is difficult. This is because both standard channels stay close to each other in deformation space. Our theoretical results concerning the standard splitting do not therefore have the same certainty as the discrimination between the standard, superlong and supershort channels. The sheer existence of standard I and II is beyond doubt, but details such as the "standard secondary barriers" (cf. fig. 8.1) are debatable. We stress, in particular, that fig. 8.5 is to be judged with reservations.

What we wish to explain is the increase of the standard I yield from ^{236}Pu to ^{242}Pu as shown in fig. 8.3. We want to derive it from the changing height of the standard secondary barriers.

See in the upper part of fig. 8.5 a detail of a channel graph of ^{240}Pu. The total graph would look like

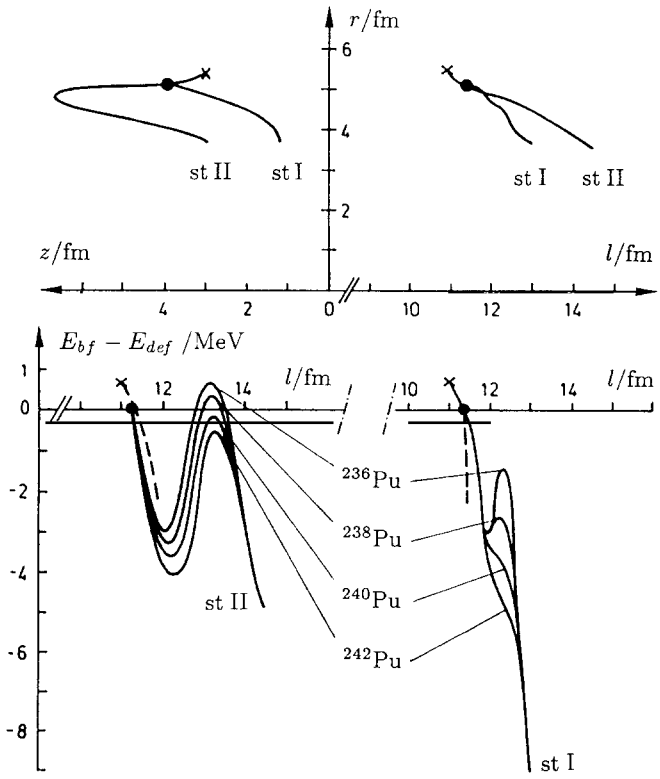

Fig. 8.5. Geometric (top) and energetic (bottom) characteristics of the standard I/II splitting in the plutonium isotopes. This figure is laid out like the channel graph 7.1, except that there is no (z, l) projection and that the graph of potential energy over l is duplicated. The missing standard counterparts in the lower parts are indicated by the dashed lines. Note that the potential energies are normalized here with respect to the bifurcation point. Thus $E_{bf} - E_{def}$ is shown instead of $E_{gs} - E_{def}$ as in fig. 7.1. The present graph was found using the three-subspace representation (2.14). This is the reason why we hesitate to claim that these curves are the definitive truth. Our standard secondary barriers have, incidentally, a similarity with the third hump of the standard barrier as discussed in [8.18].

the upper part of fig. 7.1 except that there is no supershort channel in plutonium. The present figure details the piece of the standard channel just behind the big loop. It starts at the × indicating the second standard barrier. What is not contained in fig. 7.1 but is shown here is the standard bifurcation point ● with the subsequent standard splitting. We learn from the top right-hand part of fig. 8.5 that standard I guides to rupture at a shorter semilength l. We find from the top left-hand part that standard I favors scission with small asymmetries.

It is in fig. 8.5 as in all channel graphs: the geometric characteristics of a channel do not differ much for a nucleus nearby in charge and mass. So the same upper part is valid for all plutonium isotopes, and also for uranium and thorium it looks much the same way.

However, the potential energies are different for, say, ^{236}Pu and ^{242}Pu. They are depicted in the lower parts of fig. 8.5. To maintain complete correspondence to fig. 7.1, both families of curves should appear in *one* graph. For better lucidity we disentangled the energy lines and drew the standard I and II lines, respectively, in separate graphs. Again, all the lines start at the second standard barrier. For reference a short piece of the displaced channel mate is attached, see the dashed lines.

The bumps in the potential energies are the "secondary standard barriers" declared in fig. 8.1. All these barriers *decrease* as we step from the light to the heavy isotopes. But the barriers along standard I even *disappear*. Hence we conclude that the standard I channel is partly plugged up in ^{236}Pu, whereas it is entirely open in ^{242}Pu. This fits well with fig. 8.3, which shows the larger count of standard I events in the spontaneous fission of ^{242}Pu.

Fortunately, we have independent evidence for the claim that the standard splitting is a situation-(ii) bifurcation. Namely with this kind of bifurcation order-of-magnitude differences between the channel probabilities p_{stI} and p_{stII} are impossible. In fact, $p_{\mathrm{stI}}/p_{\mathrm{stII}}$ varies by not more than from 0.2 to 0.5 [8.13].

This is especially impressive if the same nucleus at different excitation energies is considered. Schillebeeckx and co-workers [8.13] compared spontaneous fission of ^{240}Pu with the neutron-induced fission of ^{239}Pu. In the second case the nucleus receives 6.3 MeV extra excitation energy, namely the separation energy of the captured neutron. In a situation-(i) bifurcation that would produce a roaring effect. However, it was found that nothing dramatic happens with the channel probabilities [8.13]. The additional excitation energy just broadens the mass distributions as described in eq. (4.8) by the dependence on temperature T.

The comparison between measured (e) and computed (t) values is presented in table 8.8. Relative to the accuracy of the experimental and theoretical methods the agreement is as good as possible. Similar comparisons were made for the photon-induced fission of ^{232}Th, and similar conclusions with respect to the validity of eq. (4.8) could be drawn [7.6].

Accurate fits of the mass distributions of heavier actinides suggest the existence of a third standard

Table 8.8
Broadening of the mass distributions from the standard channels due to additional excitation energy. The experimental data is taken from [8.13]

Reaction	Channel	σ_A^t	σ_A^e
^{240}Pu(sf)	standard I	3.9	2.8
^{239}Pu(n, f)	standard I	4.2	3.6
^{240}Pu(sf)	standard II	5.5	5.7
^{239}Pu(n, f)	standard II	5.9	6.3

channel. It is even more asymmetric than the standard II channel and also longer. First hints of standard III can be seen in the fission of the plutonium isotopes [8.13]. It is distinct in ^{241}Am(n, f) [8.22] and powerful in ^{252}Cf(sf), see section 8.5. There is no experimental proof for its independent existence. In addition, our potential-energy calculations give indications for such a channel, but we do not have sufficiently reliable results.

Generally we expect that more and more splittings of all major channels will be discovered as soon as better analysis and instrumentation is at our disposal.

8.5. Californium has everything

Best fission, for the observer, is spontaneous fission since no inducing agent is needed. But the counting rates of spontaneous fission of natural nuclei are very small, and nuclei with higher fission rates must be created artifically. Breeding of ^{252}Cf is not too difficult, and its fission half-life is short enough to observe billions of events within a few weeks. Because of this, we have for ^{252}Cf(sf) data which are either unique or better than those measured with other nuclei. Among these we shall specify:

(i) a two-dimensional yield $Y(A, \mathrm{TKE})$ of excellent accuracy,
(ii) the superasymmetric fission events,
(iii) contraction gamma rays,
(iv) a two-dimensional neutron multiplicity $\bar{\nu}(A, \mathrm{TKE})$.

All these features are related to random neck rupture and multichannel fission. Moreover, some of them give insights that stimulate further research.

Californium is also peculiar because it has all the fission channels that we are acquainted with, see tables 7.1, 8.5 and 8.6. According to theory, ^{252}Cf has at the same time superlong and supershort channels. According to theory and experiment, a superasymmetric channel exists. And a standard III channel was found by measurements (table 8.5).

Let us start with topic (i). The dependence of the yield on the total kinetic energy is weird, as pointed out already in section 6.1. But now that we have that dependence from eqs. (6.1) and (6.2), we can establish a *representation of* $Y(A, \mathrm{TKE})$ *that is more accurate than the usual superposition of products of Gaussians* as, for example in eq. (8.3). Take the $Y(\mathrm{TKE})$ from eq. (6.1), rename it as $Y_c(\mathrm{TKE})$ to stress that the parameters (6.3) are different for each channel c. To incorporate the dependence on A, form

$$Y_c(A, \mathrm{TKE}) = Y_c(\mathrm{TKE})\left\{\frac{1}{(8\pi\sigma^2_{A,c})^{1/2}}\left[\exp\left(\frac{-(A-\bar{A}_c)^2}{2\sigma^2_{\bar{A},c}}\right)+\exp\left(\frac{-(A-A_{\mathrm{cn}}+\bar{A}_c)^2}{2\sigma^2_{A,c}}\right)\right]\right\}. \quad (8.5)$$

We have now six fitting parameters, two in addition to h_c, $l_{\mathrm{min},c}$, $l_{\mathrm{max},c}$ and $l_{\mathrm{dec},c}$, namely the average mass number $\bar{A}_c$ and the standard deviation $\sigma_{A,c}$ of the mass distribution. All these parameters reflect certain properties of a definite fission channel: h_c describes the relative frequency with which this channel is populated. It is just a numerically more convenient substitute for the channel probability p_c. $l_{\mathrm{max},c}$ is the semilength with the most favorable potential energy for scission. In fact, these values may be compared with the computed l of the prescission shape in table 8.5. $l_{\mathrm{min},c}$ is the semilength where the potential energy becomes too large to allow any scission at all. In other words, $l_{\mathrm{min},c}$ fixes an absolute upper bound of TKE, which exists due to Q-value limitations. $l_{\mathrm{dec},c}$ is related to the decrease of the potential energy ΔU with increasing semilength l [cf. (6.6)] since changes of ΔU modify the spread of

the prescission shapes and hence also the yield at low TKE. See eqs. (6.34) for illustration. All the l characterize the potential-energy surface (PES) in the direction of the elongation. $\bar{A}_c$ and $\sigma_{A,c}$, in contrast, are associated with the characteristics of the PES in the direction of asymmetry.

The complete formula for the fit can be written as

$$yield^{f}(A, \mathrm{TKE}) = \sum_{c} Y_c(A, \mathrm{TKE}) . \tag{8.6}$$

If there are five fission channels, 30 parameters have to be accommodated. In proportion to the thousands of data which are reproduced, this is a small number. Our results are given in table 8.9.

The mean mass numbers $\bar{A}$ can be compared with the $\bar{A}^{e}_{H}$ in table 7.1, and the l_{max} with the l in table 8.5. Good agreement is found for standard I and II, but also superlong comes out as desired since its large l_{dec} effects the same as a larger value of l_{max}: compare the good agreement of $\overline{\mathrm{TKE}}^{e}$ and $\overline{\mathrm{TKE}}^{t}$ in table 7.1. But the experimental supershort contribution, if it exists, is not represented by the fit. And last and worst, the calculations for the superasymmetric channel have slipped.

More insight can be obtained from fig. 8.6. Its upper part is a contour plot of the measured yield $yield^{e}$ [6.14]. Plotting beneath the fitted yield would not help much since the eye could barely see any difference. But from the errors we can learn something meaningful.

No significant errors occur in the bulk. Only at the edges, where the counting rates, and thus the $yield^{e}$, are small, do misfits occur. An insignificant misfit is, for example, the broad beard at low total kinetic energies as it is caused by unwanted scatterings in the detector.

However, the black patches at high TKE close to mass symmetry are significant. These are the long-sought-for fingerprints of the supershort channel, which was not taken into account when the fit was performed. One can even understand that the supershort contribution does not appear exactly at symmetry. For a long piece of the supershort channel passes, in californium, through asymmetry, as shown in fig. 7.1.

Likewise the dotted patches are significant. They demonstrate how difficult it is to represent the superasymmetric component adequately. In the present case, the superasymmetric component is swallowed by the fluctuations of standard III so that only in the region of transition from standard III to superasymmetric does a misfit remain, namely the dotted patches.

So we have arrived at topic (ii): the *superasymmetric component* seems to be special in every respect. This can be concluded from fig. 8.7: in the mass range above $A \approx 178$ and below 74 an almost discontinuous behavior in $\overline{\mathrm{TKE}}(A)$ and $\sigma_E(A)$ is observed. Such a jumpy style is incompatible with a broad fission channel and indicates that the superasymmetric events are rather produced by cluster

Table 8.9

Parameters for the representation of the yield $Y(A, \mathrm{TKE})$ from spontaneous fission of ^{252}Cf according to eqs. (6.1), (6.2), (8.5) and (8.6) based on the data from [6.14]. A representation of this kind was first published in [6.13]. The present values are slightly improved, but the values of the superasymmetric parameters are still not more than order-of-magnitude estimates

Channel	h	l_{min}	l_{max}	l_{dec}	$\bar{A}$	σ_A
standard I	$1.41\,10^5$	10.1	17.1	0.103	134.9	3.13
standard II	$8.71\,10^5$	13.7	17.9	0.270	142.5	5.00
standard III	$3.13\,10^5$	13.6	18.7	0.318	148.5	7.13
superasymmetric	$1.71\,10^4$	16.9	20.8	0.165	178.6	0.37
superlong	$2.85\,10^4$	14.1	18.2	0.405	127.5	12.6

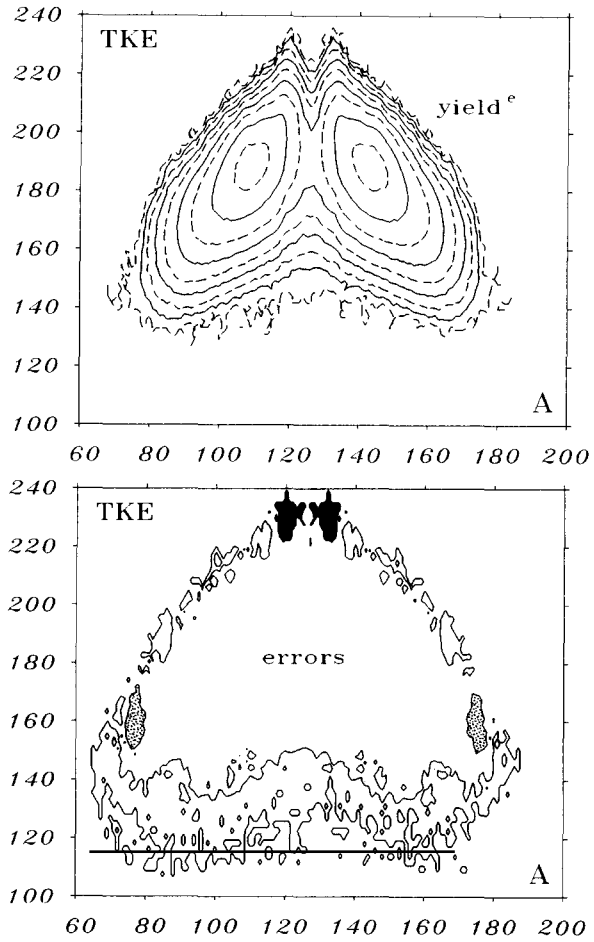

Fig. 8.6. Upper part: measured yield^e [6.14] from the spontaneous fission of ^{252}Cf as a contour plot over the plane of fragment mass number A and total kinetic energy TKE. The dashed contours are for 3, 30, 300, 3000 and 30000 counts, from outside inwards, while the full ones indicate 10, 100, 1000 and 10000 counts, respectively. Lower part: the errors of a fit with the representation (8.6). The contours are defined by $|yield^e - yield^f|/yield^e = 0.5$. $yield^f$ is computed with the parameters of table 8.9, except for the superasymmetric contribution, which was cancelled.

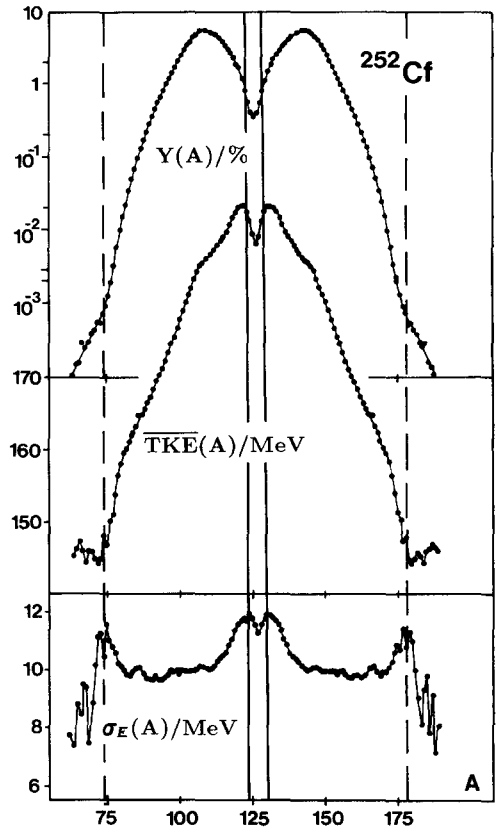

Fig. 8.7. Yield $Y(A)$, average total kinetic energy $\overline{TKE}(A)$ and standard deviation $\sigma_E(A)$ of the total kinetic energy for the spontaneous fission of californium. The figure is taken from [3.15]. The measurements were done by Budtz-Jørgensen and Knitter [6.14].

emission [8.23]. This might also be the reason for the poor agreement between our fission channel calculations and the experimental data, cf. table 7.1.

The superasymmetric events in the spontaneous fission of ^{252}Cf were discovered by Barreau and co-workers [8.24], but it seems that a similar phenomenon was observed earlier in the fission of ^{238}U with 2 MeV neutrons [8.25]. Furthermore, superasymmetric events also occur in ^{248}Cm(sf) [8.26]. We searched for the superasymmetric channel in all these nuclei. For ^{248}Cm we found a channel with similar characteristics as those given in table 7.1 for ^{252}Cf. In particular, we noticed no significant change in the superasymmetric barrier. We saw no indication of the superasymmetric channel in ^{238}U.

Figure 8.7 is still useful for another purpose: the standard deviations $\sigma_E(A)$ are the most straightfor-

ward separators between contributions from different fission channels. There are, for example, peaks in $\sigma_E(A)$ at $A \approx 123$ and $A \approx 129$. They limit the reign of the superlong channel. These limits have little to do with the actual width σ_A of table 7.1. They just indicate the points where two channels yield about equal abundance. The mechanism behind is simple superposition: two channels may produce contributions with similar $\sigma_{E,c}$, but the respective $\overline{\mathrm{TKE}}_c$ are usually somewhat different. This produces an overlap enhancement for the total σ_E, as represented, for example, by the third term in (8.1). Exactly this observation led Britt and colleagues [1.10] to postulate those two modes of fission that we now call the standard and the superlong.

Concerning topic (iii): the superlong channel must show up everywhere. We have seen this for the yield $Y(A)$, total kinetic energy $\overline{\mathrm{TKE}}(A)$ and neutron multiplicities $\bar{\nu}(A)$ in section 7.2. But the superlong channel also makes its mark on the *total gamma multiplicities*.

Refer to fig. 3.2. The deformed fragments shown in fig. 3.2b are charged. As they separate, they will relax to a nearly spherical shape. This requires a redistribution of charge. An unsteady motion of charge, however, creates electromagnetic radiation, gamma quanta, in other words. At present the velocity of relaxation is unknown, nor is it known if it is combined with an oscillation. But it is clear that, if high-energy *contraction gamma quanta* exist, they must be preferentially emitted from fragments created via the superlong channel. For the superlong channel generates the fragments with the largest deformations.

Usually gamma multiplicities ν_γ vary as functions of the gamma energy E_γ in a Boltzmannian fashion, proportional to $\exp(-E_\gamma/T)$. Recently for certain masses an enhancement at $E_\gamma > 1.5\,\mathrm{MeV}$ was observed [8.27–8.29]. The respective gamma quanta were separated and their multiplicity was displayed as a function of the fragment mass number, cf. fig. 8.8. We see that the high-energy gamma rays come in the mass region characteristic for the superlong contribution. The average value $\bar{A} \approx 126$ and the deviation $\sigma_A \approx 8$ read from fig. 8.8 agree reasonably with the values supplied by table 7.1, which for its part were obtained from the yield $Y(A, \mathrm{TKE})$. Three further properties fit into the picture. The first is the average gamma energy of about 4 MeV, which is larger but of the same order as the energies obtainable from the smaller giant quadrupole oscillations. Second, the share of the multiplicity that the high-energy gamma quanta contribute is well below 1%. This is compatible with a superlong probability $p_{\mathrm{sl}} = 1.3\%$ (cf. table 8.5) when one considers that a fragment emits about five gamma quanta. Third, the high-energy quanta appear as coincident pairs. And in fact, the superlong channel can produce only *two* strongly deformed fragments if not very asymmetrical rupture occurs.

Physically the contraction gamma quanta are different from the usual statistical gammas. The contraction gammas are emitted before the neutrons appear. Most statistical gamma quanta are puffed

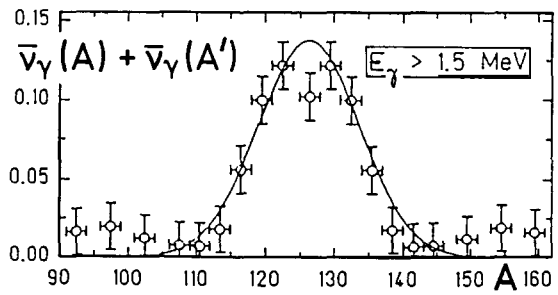

Fig. 8.8. Total gamma multiplicity $\bar{\nu}_\gamma(A) + \bar{\nu}_\gamma(A')$ ($A' = A_{\mathrm{cn}} - A$) as a function of the mass number A of one the fragments. It was thus not decided from which fragment the high-energy ($E_\gamma > 1.5\,\mathrm{MeV}$) gamma quanta came. The data were measured by Schmid-Fabian et al. [8.27, 8.28].

out only after the evaporation of neutrons. Therefore, the statistical gammas have to be content with what is left from the higher-priority processes, that is with approximately half of the separation energy of a neutron. The experimental proof of this fact is also quite new [8.27–8.29].

Finally topic (iv): the general procedure for the prediction of exit-channel observables consists of two parts: find the prescission shapes and derive the measurable quantities. The first part can be done, in low-energy fission, by an examination of the potential energy of the scissioning nucleus. This involves quantum shell effects. The second part is done relying only on continuum mechanics. Such an inconsistency becomes conspicious as soon as data of higher differentiation are considered. An example is the *neutron multiplicity* $\bar{\nu}(A, \mathrm{TKE})$ *as a function of the fragment mass number and the total kinetic energy*.

Experimentally it is found that the detailed multiplicity may be represented as

$$\bar{\nu}(A, \mathrm{TKE}) = \begin{cases} \partial_{\mathrm{TKE}} \bar{\nu}(A)\,[\mathrm{TKE} - \mathrm{TKE}_{\max}(A)] & \text{if } \mathrm{TKE} < \mathrm{TKE}_{\max}(A)\,, \\ 0 & \text{otherwise}\,. \end{cases} \tag{8.7}$$

Two one-variable functions $\mathrm{TKE}_{\max}(A)$ and $\partial_{\mathrm{TKE}} \bar{\nu}(A)$ are thus sufficient to describe the two-variable function $\bar{\nu}(A, \mathrm{TKE})$ [8.27, 6.14]. The linearity is, of course, an approximation. We expect negative corrections first because it costs more and more energy when several neutrons are emitted and second, in the domain of superlong, because of the contraction gammas.

Within the frame of linearity each of the three functions

$$\bar{\nu}(A)\,, \quad \partial_{\mathrm{TKE}} \bar{\nu}(A)\,, \quad \mathrm{TKE}_{\max}(A) \tag{8.8}$$

can be expressed by the others. To see this, one inserts eq. (8.7) into the trivial relation

$$\bar{\nu}(A) = \frac{\int_0^\infty \bar{\nu}(A, \mathrm{TKE})\, Y(A, \mathrm{TKE})\, \mathrm{d}\,\mathrm{TKE}}{\int_0^\infty Y(A, \mathrm{TKE})\, \mathrm{d}\,\mathrm{TKE}}\,. \tag{8.9}$$

An inessential neglect at the integration limits yields the announced relationship

$$\bar{\nu}(A) = \partial_{\mathrm{TKE}} \bar{\nu}(A)\,[\overline{\mathrm{TKE}}(A) - \mathrm{TKE}_{\max}(A)]\,. \tag{8.10}$$

The average kinetic energy $\overline{\mathrm{TKE}}(A)$ is so well established that it must be considered as given.

Equation (8.10) may be interpreted as follows: the "elastic energy" contained in the fragments just after scission depends on two factors. One of them is the "elasticity module" of that piece of the prescission nucleus from which the fragment is to be made. This module is expressed by the slope function $\partial_{\mathrm{TKE}} \bar{\nu}(A)$. In fact, one may identify the total kinetic energy as an inverse measure of the elongation and the multiplicity as a measure of the elastic energy. The second factor is the deviation from the average elongation, expressed by the function $\overline{\mathrm{TKE}}(A) - \mathrm{TKE}_{\max}(A)$. This factor is the more trivial one because it contains only the effects described by the plain random neck rupture model. It is therefore not surprising that it is again a sawtooth curve. But the sawtooth in the slope function, see fig. 8.9, was not expected. The paradox becomes understandable if one remembers that random neck rupture presumes homogeneous matter. If the prescission nucleus has a substructure, it must fail. Hence fig. 8.9 may be interpreted by a prescission shape that has a soft neck and two hard heads. Stretching the shape is facilitated just by the neck; the heads remain inert. The two minima in fig. 8.9 correspond to the masses of these heads. Amusingly enough we find the mass numbers $A \approx 28 + 50$ and $A \approx 50 + 82$.

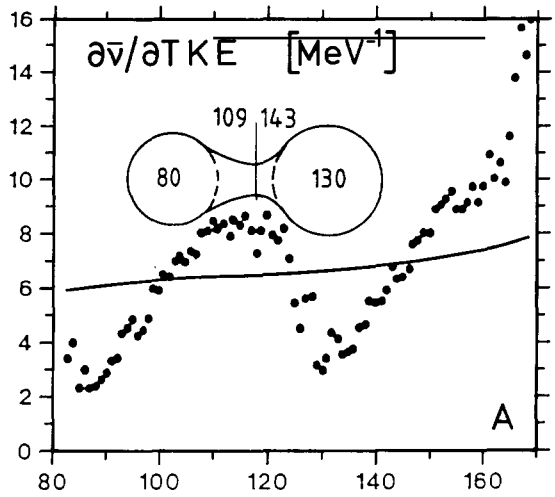

Fig. 8.9. The slope function $\partial\bar{\nu}/\partial$TKE defined in (8.7) as a function of fragment mass number A. The measurements, displayed by the dots, were performed by Budtz-Jørgensen and Knitter [6.14]. Schmid-Fabian et al. [8.27] were the first to publish data like these. The full line is the prediction from plain random neck rupture. The numbers on the prescission shape indicate the stiff heads (80, 130) and the most probable partition (109, 143), compare [8.28].

9. The theory of fission channels

9.1. Strutinsky's approach

To reveal the fission channels discussed in the previous two chapters, one must compute the potential energy of deformed nuclei E_{def} as a function of the shape coordinates. But even with this ability it remains to analyze the computed data in the multidimensional space of shape parameters. This is a tough job for which tools will be presented in the next two sections. Here we only detail our way to compute the E_{def}.

Strutinsky's approach [1.2] was taken in a textbook version [9.1]. The potential energy is composed of a liquid-drop and a shell part

$$E_{\mathrm{def}} = E_{\mathrm{ld}} + E_{\mathrm{shell}}\,, \tag{9.1}$$

both depending on deformation.

For the liquid drop part E_{ld} we took the Myers–Swiatecki model [9.2] with its improved set of parameters [9.3]. The computation of the Coulomb energy of a deformed shape was greatly accelerated by the use of the double-divergence formula [9.4, 9.5]. The integrals were done using numerical extrapolation methods [9.6] with careful treatment of the singularities.

More modern approaches than the Myers–Swiatecki model are available, for example, folding techniques [8.5] or semiclassical methods [9.7]. However, folding methods do not admit a *curvature correction*, which turned out to be important for the energy landscape close to scission [9.8, 9.9], and no generally accepted prescription for the usage of the semiclassical methods seems to exist.

The Myers–Swiatecki model admits a curvature correction, but the approved version [9.3] does not have one. Therefore, our energies $E^{\mathrm{t}}_{\mathrm{des}}$ of the prescission shapes (table 8.5) are probably too large, that is, the tails of the potential energy in fig. 7.1 decrease too much.

The computation of the shell part in (9.1) is broken down in three phases:

(i) Obtain the single-particle spectrum,

(ii) smear it out,

(iii) apply BCS pairing on both spectra.

The difference between the BCS total energies for sharp and smeared spectra is E_{shell}.

(i) For the single-particle spectrum it takes Hamiltonians for neutrons

$$H_{\text{n}} = \frac{\boldsymbol{p}^2}{2M_{\text{n}}} + V_{\text{n}}(\boldsymbol{r}) - \frac{\lambda}{2(M_{\text{n}}c)^2}\, \boldsymbol{s}\cdot[\nabla V_{\text{n}}(\boldsymbol{r}) \times \boldsymbol{p}] \tag{9.2}$$

and protons

$$H_{\text{z}} = \frac{\boldsymbol{p}^2}{2M_{\text{z}}} + V_{\text{z}}(\boldsymbol{r}) - \frac{\lambda}{2(M_{\text{z}}c)^2}\, \boldsymbol{s}\cdot[\nabla V_{\text{z}}(\boldsymbol{r}) \times \boldsymbol{p}] + V_{\text{Coul}}(\boldsymbol{r})\,. \tag{9.3}$$

Here $\boldsymbol{p}$ and $\boldsymbol{s}$ denote the vector operators of momentum and spin. M_{n} and M_{z} are the masses of the neutrons and the protons, respectively, and $V_{\text{n}}(\boldsymbol{r})$ and $V_{\text{z}}(\boldsymbol{r})$ are their respective single-particle potentials. We choose them to be of Woods–Saxon type

$$V_{\text{n,z}}(\rho, \zeta) = -\frac{V_{0,\text{n,z}}}{1 + \exp\{[L(\rho, \zeta) - R]/a\}}\,. \tag{9.4}$$

The spin–orbit strength, radius and diffuseness

$$\lambda = 23.8[1 + 2(N_{\text{cn}} - Z_{\text{cn}})]/A_{\text{cn}}\,, \qquad R = 1.24A_{\text{cn}}^{1/3}\ \text{fm}\,, \quad a = 0.65\ \text{fm} \tag{9.5}$$

are the same for neutrons and protons (N_{cn}, Z_{cn} and A_{cn} denoting the numbers of neutrons, protons and nucleons in the fissioning nucleus, respectively), but the depths of the potentials

$$V_{0,\text{z,n}} = 53.3[1 \pm 0.63(N_{\text{cn}} - Z_{\text{cn}})/A_{\text{cn}}]\ \text{MeV} \tag{9.6}$$

are different [9.10, 9.11]. Finally,

$$V_{\text{Coul}}(\boldsymbol{r}) = \frac{3Z_{\text{cn}}e^2}{4\pi R^3} \int\limits_{\text{(nucleus)}} \frac{\mathrm{d}^3\boldsymbol{r}'}{|\boldsymbol{r} - \boldsymbol{r}'|} \tag{9.7}$$

is the Coulomb potential felt by one proton.

Written in cylindrical coordinates ρ, ζ, φ, the function $L(\rho, \zeta)$ adapts the potentials (9.4) to the actual shape. We obtain L from the numerical solution of

$$\rho_{\text{shape}}(\zeta R/L; l, r, z, c, s) = \rho R/L\,. \tag{9.8}$$

This relation coerces the similarity of all equipotential contours [9.12, 9.13]. The description of the surface ρ_{shape} was introduced in eq. (2.2).

Eigenvalues of (9.2) and (9.3) are found by expanding the eigensolutions in terms of harmonic

oscillator functions for a spheroid

$$\langle \rho, \zeta, \varphi | n_\rho, n_\zeta, m, m_s \rangle = N\left[\alpha\left(\frac{M_{n,z}\omega_\rho}{\pi\hbar}\right)^3\right]^{1/4} P^m L_{n_\rho}^{(m)}(P^2) H_{n_\zeta}(Z) \exp\left(-\frac{P^2+Z^2}{2} + im\varphi\right) \tag{9.9}$$

with

$$N := \left(\frac{n_\rho!}{2^{n_\zeta} n_\zeta!(n_\rho+m)!}\right)^{1/2}, \qquad P := \left(\frac{M_{n,z}\omega_\rho}{\hbar}\right)^{1/2}\rho, \qquad Z := \left(\frac{M_{n,z}\alpha\omega_\rho}{\hbar}\right)^{1/2}\zeta .$$

The respective series were inserted into (9.2) or (9.3). The resulting equations were multiplied from the left with the complex conjugates of (9.9) and integrated over ρ, ζ and φ using Gauss–Laguerre and Gauss–Hermite procedures of order 25 and 20, respectively. The algebraic eigenvalue problem was solved, reducing the matrices to tridiagonal form and subsequent bisection of the characteristic polynomial [9.6].

Formulas like (9.9) with their quantum oscillator numbers n_ρ, n_ζ, three-projections of angular momentum and spin m, m_s, generalized Laguerre $L_n^{(m)}(x)$and Hermite polynomials $H_n(x)$ are more than familiar. We have included them only to indicate the significance of two parameters: the frequency ω_ρ and the ratio α. Choosing these parameters conveniently can save much computational work as accurate representations of the eigensolutions are obtained with fewer harmonic oscillator functions. ω_ρ is determined by the overall size of the single-particle potential, while α is related to the relative elongation of the spheroid.

We fix α by the following prescription: define the surface of the spheroid as

$$\rho_{\text{spheroid}}(\zeta) = \begin{cases} \alpha[\beta^2 - (\zeta - s)^2]^{1/2} & \text{for } |\zeta - s| < \beta , \\ 0 & \text{elsewhere} . \end{cases} \tag{9.10}$$

Then minimize

$$\int_{-\infty}^{\infty} \mathrm{d}\zeta \, [\rho_{\text{shape}}(\zeta) - \rho_{\text{spheroid}}(\zeta)]^2 . \tag{9.11}$$

This gives you, since the position of the centroid s is known from the true surface description ρ_{shape}, values for α and β. We dispense with β.

The frequency ω_ρ is determined by minimization of

$$\int_0^{r_c} \frac{\mathrm{d}r}{r_c} \left(\frac{M_{n,z}\Omega^2 r^2}{2} - \Xi - \frac{V_{0,n,z}}{1+\exp([r-R]/a)}\right)^2 \tag{9.12}$$

with parameters for the Woods–Saxon potential as defined in (9.5) and (9.6). The cut-off radius $r_c := [2\Xi/M_{n,z}\Omega^2]^{1/2}$ is the zero of the oscillator potential in (9.12). Dispense with Ξ and keep Ω. Then, as the volume of the spheroid must not depend on the deformation, we obtain

$$\omega_{\rho,n,z} = \Omega/\alpha^{1/3} . \tag{9.13}$$

The indices n and z were affixed to clarify that this frequency is different for neutrons and protons. Further computational tricks concerning this subject can be found in [9.14].

Normally we took the functions (9.9) from the first 13 main oscillator shells. Checks were performed with functions from the first 18 shells, in particular for shapes with large deformations. We sometimes observed changes in the sequence of the levels, but the final result E_{shell} was never significantly altered.

(ii) Let $\{\varepsilon_\nu\}$ denote the single-particle energies computed as described in the previous phase and $\{n_\nu\}$ their multiplicities, for neutrons and protons separately. We obtain from them the *sharp* level density as

$$\hat{g}(\varepsilon) = \sum_\nu n_\nu \delta(\varepsilon - \varepsilon_\nu) \,. \tag{9.14}$$

In contrast, the *smeared* level density is

$$\tilde{g}(\varepsilon) = \frac{1}{\sqrt{\pi}\gamma} \sum_\nu n_\nu P_6([\varepsilon - \varepsilon_\nu]/\gamma) \exp\{-[(\varepsilon - \varepsilon_\nu)/\gamma]^2\} \,. \tag{9.15}$$

The polynomial

$$P_6(x) = -\tfrac{1}{6}x^6 + \tfrac{7}{4}x^4 - \tfrac{35}{8}x^2 + \tfrac{35}{16} \tag{9.16}$$

is derived from Hermite polynomials along standard lines [9.1]. For the smearing parameter γ we fixed 8 MeV.

One has the problem that $\tilde{g}(\varepsilon)$ suddenly falls as soon as ε approaches the edge of the Woods–Saxon potential if only the bound states are included in eq. (9.15). We use the first 250 states to keep the smeared density rising. When we plotted E_{shell} as a function of γ, we always found a broad plateau for small and moderate deformations, normally extending from $\gamma = 6$ MeV to $\gamma = 10$ MeV. Close to the prescission shapes, the quality of the plateau deteriorated, but a shoulder near 8 MeV was still seen, similar to that reported in [9.15]. These features persisted when the number of the pseudofree states included was varied. However, it emerges from such checks that the *absolute accuracy* of Strutinsky's method is not better than 1 MeV.

(iii) For BCS pairing at temperature T one first introduces the quasiparticle energies

$$\varepsilon_{\text{qp}} := \begin{cases} [(\varepsilon - \lambda_{\text{F}})^2 + \Delta^2]^{1/2} & \text{if } \varepsilon_{\min} < \varepsilon < \varepsilon_{\max} \,, \\ |\varepsilon - \lambda_{\text{F}}| & \text{else} \,, \end{cases} \tag{9.17}$$

and computes the gap Δ and the Fermi level λ_{F} from the gap equation

$$\frac{2}{G} = \int_{-\infty}^{\infty} \mathrm{d}\varepsilon \; g(\varepsilon) \frac{1}{\varepsilon_{\text{qp}}} \tanh \frac{\varepsilon_{\text{qp}}}{2T} \,, \tag{9.18}$$

and from the conservation of the average particle number

$$N = \int_{-\infty}^{\infty} \mathrm{d}\varepsilon \; g(\varepsilon) \left(1 - \frac{\varepsilon - \lambda_{\text{F}}}{\varepsilon_{\text{qp}}}\right) \tanh \frac{\varepsilon_{\text{qp}}}{2T} \tag{9.19}$$

via a Newton–Raphson procedure [9.6] for given pairing strength G and range of pairing forces $(\varepsilon_{\min}, \varepsilon_{\max})$. For N we must substitute the total number of neutrons N_{cn} or protons Z_{cn} and correspondingly for $g(\varepsilon)$ the level density of neutrons or protons. The total energy is

$$E(g, G, N) = \int_{-\infty}^{\infty} d\varepsilon\, g(\varepsilon)\varepsilon\left(1 - \frac{\varepsilon - \lambda_F}{\varepsilon_{qp}}\right)\tanh\frac{\varepsilon_{qp}}{2T} - \frac{\Delta^2}{G}\,. \tag{9.20}$$

We can use these equations with the sharp and the smeared level densities. If N is even, the shell correction is

$$E_{shell} = E(\hat{g}, G, N) - E(\tilde{g}, G, N)\,. \tag{9.21}$$

For the treatment of an unpaired nucleon we notice that one can compute the total energy without BCS by putting G, Δ and Δ^2/G to zero, and by omitting eq. (9.18). We consider the particle on the highest energy level as unpaired and calculate for it the Strutinsky corrections without pairing:

$$\begin{aligned} E_{shell} = {} & E(\hat{g}, G \neq 0, N-1) - E(\tilde{g}, G \neq 0, N-1) + E(\hat{g}, G = 0, N) - E(\tilde{g}, G = 0, N) \\ & - [E(\hat{g}, G = 0, N-1) - E(\tilde{g}, G = 0, N-1)]\,. \end{aligned} \tag{9.22}$$

For the range of the pairing forces $(\varepsilon_{\min}, \varepsilon_{\max})$ we selected the $\sqrt{3N}$ single-particle energies below and above the Fermi level. Such a small range was chosen since at large deformations it happens that the Fermi level comes close to the edge of the potential, and we did not wish to include pseudofree states in the pairing corrections. For compensation we had to insert a rather large pairing strength $G = 34/A_{cn}$ MeV into eq. (9.18).

All multichannel calculations presented in this review refer to zero temperature T. Quite a few data [5.20, 7.3–7.5, 8.9, 8.12] at higher temperatures are available so that a theoretical exploration at $T \neq 0$ is certainly worthwhile.

9.2. Channel searching

Now that we know how to compute the potential energies E_{def} for arbitrary deformations, what can we do with this? They are a six-dimensional data set when the shape parameters (2.1) are employed, and with the subspaces (2.14) or (2.16) they are still a four-dimensional one. The classical procedure is to remove all but two parameters by minimization of E_{def} and to plot the result as a contour plot as in ref. [9.16]. But this may lead to ambiguous interpretations as discussed at the end of section 7.1.

We need at least three shape parameters. To visualize E_{def} in a three-dimensional space, we can fix one of them and plot E_{def} as a function of the two remaining parameters. Such a plot is shown in fig. 9.1a. Next we assign a somewhat different value to the fixed parameter, plot E_{def} again as a function of the two others and so forth. In this way we obtain a stack of contour plots containing four-dimensional information. This was in fact our technique when we started our investigation, and it is still a valuable means to study bewildering geometrical features.

However, the method is limited to four-dimensional data, and even there it costs a great amount of computational time. As already pointed out in section 8.1, one is rarely interested in the geometrical survey displayed by a contour plot. Rather, one wishes to find certain distinguished points such as

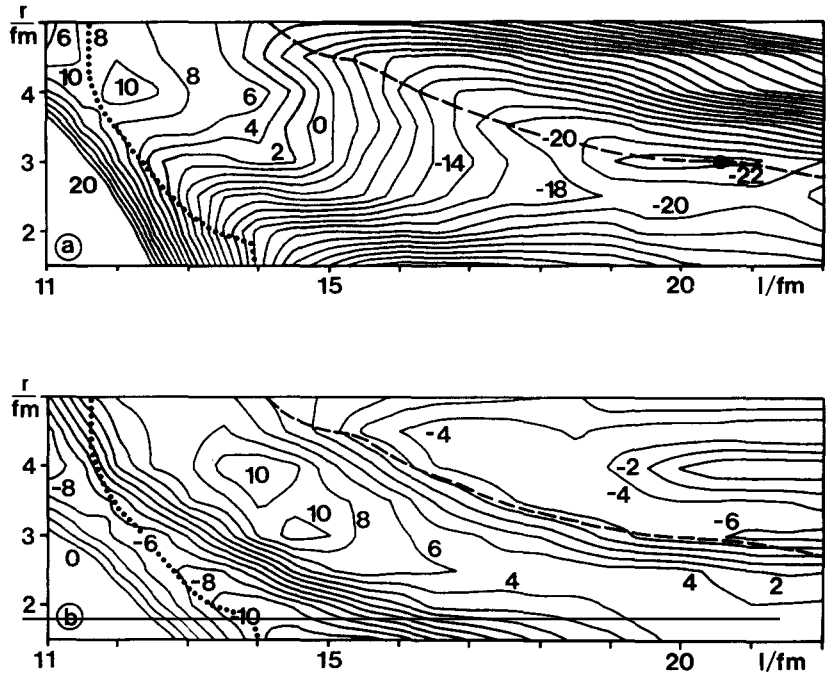

Fig. 9.1. Contour plots of the potential energy $E_{gs} - E_{def}$ (a) and of the shell correction E_{shell} (b) in the plane of the semilength l and neck radius r for ^{252}Cf. The asymmetry z is zero everywhere. The shape representation (2.14) was employed. The numbers at the contours give energies in MeV so that negative values mean there is a gain. This figure refers immediately to fig. 7.1: the dotted line traces the supershort channel while the dashed one indicates superlong. The standard and superasymmetric channels cannot be seen because of their asymmetry. The full circle marks the minimum on the superlong channel defining its prescission shape. Supershort and superlong were found with $(q_l, q_r, q_z) = (1, 0, 0)$, cf. eq. (9.23), which is not exactly the normal vector needed for steepest descent. However, one can read from this figure how small the change is. Note the large size of the shell corrections in (b). Strutinsky renormalization with its accuracy of about 1 MeV is therefore likely to give meaningful results.

minima, saddle points, prescission shapes and the low-energy connections between them [8.1]. One can do this by a search for paths of *steepest descent* which we call *channel searching*. Our way to implement it can be conveniently illustrated in a three-dimensional space (l, r, z) describing elongation, constriction and asymmetry [3.15]. In this space we define a plane

$$(l - l_0)q_l + (r - r_0)q_r + (z - z_0)q_z = 0 \tag{9.23}$$

by the normal vector (q_l, q_r, q_z) and a starting point (l_0, r_0, z_0) in the three-dimensional space. We ask the computer to slide on this plane, checking for the minimum value of E_{def} compatible with the constraint (9.23). The computer finally reports the minimal E_{def} at the point $(l_{min}, r_{min}, z_{min})$, so that we have data to enter the dots (l_{min}, r_{min}), (r_{min}, z_{min}) and (z_{min}, l_{min}) into the various projections of a channel graph like fig. 7.1. Next we shift the starting point so that it is about 0.5 fm apart from the first one and repeat the sliding. This gives a new minimal E_{def} at a different $(l_{min}, r_{min}, z_{min})$, and once more we enter its data into fig. 7.1. Doing all this over and over again produces the series of dots in fig. 7.1, which may be joined to form a line. At this stage we check if the direction of the normal vector was everywhere at least approximately parallel to the constructed line. When this is not the case, we adjust the normal vector and repeat the calculation until convergence takes place.

This procedure has the advantage of computing only in the relevant parts of the space. All the more

important, it is readily generalized to problems with more than four dimensions. Altogether we worked with three variants:

(i) channel searching in the space (l, r, z), cf. eqs. (2.14, 2.15).

(ii) working in the space (l, r, z, c, s), see eqs. (2.1–2.13), but eliminating z and c for every given l, r, s by minimization of the liquid-drop energy E_{ld}.

(iii) channel searching in the space (l, r, z, c, s), see eqs. (2.1–2.13).

The quantitative comparisons with experiments, as presented in the tables 7.1 and 8.1–8.8 and in the figs. 7.3, 7.4, 8.2 and 8.4, were achieved with variant (iii).

We played the variants off against each other to check reliability. In addition, we rotated the normal vectors by angles of 45° around the channels discovered and varied the pairing strength G from 0 to $34/A_{\mathrm{cn}}$ MeV. The standard, superlong and supershort channels satisfied all these tests. In addition, the standard splitting was confirmed, but with significant changes of the bifurcation point and the secondary barriers. Our results concerning the superasymmetric channel turned out to be variable.

A renormalization procedure like Strutinsky's involves a great loss of significant digits, see the minus signs in eqs. (9.21, 9.22). The *relative accuracy* of E_{shell} within a small volume of deformation space is at best 0.1 MeV. Because of this, one should use an algorithm for the minimization that does not depend on derivative-like information. We applied the Nelder–Mead routine [9.6].

Due to the limited precision of E_{shell}, locations in the fission channels cannot be more accurate than 0.5 fm. This typically causes errors in $\overline{\mathrm{TKE}}^{\mathrm{t}}$ by 5 MeV, by three mass units in $\bar{A}^{\mathrm{t}}_{\mathrm{H}}$, by 25% in σ^{t}_{A}, and by somewhat less than 1 neutron in $\bar{\nu}^{\mathrm{t}}$, cf. table 7.1.

9.3. Distinguished points

Since the fission channels are nothing more than favorable connections between distinguished points, these points have to be defined with particular care.

The minima are the simplest. Just minimize E_{def} as a function of all available shape parameters.

For saddles take the method of steepest descent as described in the previous section and seek the maximum along one of the fission channels.

Bifurcation points are found by following two channels and looking where they join.

For the prescission shapes fix the neck radius r and minimize E_{def} as a function of the remaining parameters. More precisely, we worked with two variants:

(i) We fixed the normal vector as $(q_l, q_r, q_z) = (0.7, -0.7, 0)$, cf. eq. (9.23), and shifted the initial point (l_0, r_0, z_0) until the minimum was obtained at $r_{\mathrm{min}} = 1.5$ fm.

(ii) We fixed the normal vector as $(q_l, q_r, q_z) = (1, 0, 0)$ and shifted the initial point (l_0, r_0, z_0) until the minimum was found at $r_{\mathrm{min}} = 1.2$ fm,

In shape representations that contained more than the three parameters l, r and z we also executed minimization with respect to the other parameters. Selecting 1.2 fm or 1.5 fm as values for r_{min} was inspired by the observation that a neck is certainly broken when its radius becomes less than the radius of a nucleon.

Except for the preactinides, the prescission shape of the superlong channel could be defined as a minimum as indicated in fig. 7.1. The obstacle, which hinders such a prescission shape from crashing, is never higher than 2 MeV, cf. fig. 9.1a. Since the nucleus gains more than 10 MeV on the descent from the superlong barrier, see again fig. 7.1 as well as tables 8.3 and 8.5, the obstacle is easily overridden.

For all quantitative comparisons as in tables 7.1, 8.5, 8.6 and in figs. 7.3, 7.4, variant (i) with the full set (2.1) of shape parameters was applied. Variant (ii) was used to check the accuracy. Normally the

differences are small since the capillarity instability enforces abrupt constrictions, that is the neck radius r changes much while the other parameters remain.

The shell effects, which produce such different prescission shapes as the standard, superlong and supershort, displace the onset of the capillarity instability. Consequently eq. (3.3) must be modified. We can write it as

$$2l = rayl \times r\,. \tag{9.24}$$

Under a pure liquid-drop regime *rayl* is 11. For the supershort channel, however, *rayl* must be smaller than that value and for the superlong channel larger. The liquid-drop prescission length is approximately given by (5.1). If we wish to retain the liquid-drop value as a special case, we must scale *rayl* according to

$$rayl = 11l/2.4r_{\mathrm{cn}}\,, \tag{9.25}$$

where l is the semilength of the respective prescission shape, that is, values taken from table 8.5. In the case of ^{252}Cf one finds for the standard channel a *rayl* not far from 11, while *rayl* is less than 9 for the supershort channel and more than 12 for the superlong channel.

One can combine (9.24) and (9.25) to compute the radius r of the prescission shape, and end up with values of 3 fm. This is significantly larger than the 1.2 or 1.5 fm on which the variants (i) and (ii) are based. Moreover, when one compares the prescission shapes in fig. 7.2 with those in figs. 2.2 or 3.1, one recognizes that the prescission shapes found by the potential energy have a much too curved neck. This inconsistency is caused by the marriage of static potential-energy calculations with dynamic random neck rupture. Due to dynamics, the neck stays thick until rupture happens simply because the matter in the neck has no time to escape, see section 3.3 and especially fig. 3.4 for a discussion. In addition, a potential-energy calculation is unable to cover the overstretching. Overstretching, however, is important as was stressed in section 3.4.

We tried to compensate for all this by taking from table 8.5 only the semilength l and the average fragment mass number $\bar{A}_{\mathrm{H}}$ that can be computed by eq. (2.17) from the shape. Then we had to face the fact that random neck rupture works with a unit radius of 1.15 fm, as pointed out in (4.1). The Myers–Swiatecki model [9.3], on which our potential energy calculations rest, relies on 1.2249 fm. Consequently, we had to multiply all lengths from the potential-energy calculations by 1.15/1.2249 to make them meaningful for random neck rupture. We obtained the temperature T at scission from (6.11), (6.13, 6.14) and (6.7), inserting values from tables 8.1–8.5. We replaced eq. (3.3) by (9.24, 9.25), and then had a straightforward run of the procedures explained in ch. 4. All the results documented in tables 7.1 and 8.8 and in figs. 7.3, 7.4 and 8.4 were obtained in this way.

9.4. Magic numbers of fission

Powerful shell effects as observed in fig. 9.1b are fundamental for the formation of exit channels in nuclear fission. These shell effects must be caused by significant gaps in the single-particle spectrum, and if there are gaps, magic numbers must also exist. These numbers are properties of the *fissioning nuclei*. They are listed in table 9.1.

The neutron magic number of the supershort channel is easiest to discuss. Figure 9.2 displays the neutron single-particle spectrum ε_ν of the nucleus ^{258}Fm as a function of elongation. There is nothing

Table 9.1
Magic numbers of fission. A dash indicates a magic range, an arrow signals transition. In the case of the standard and superlong channels our evidence concerning neutron magic numbers or ranges is not sufficiently clear

Channel	Protons	Neutrons
supershort	100 – 108	166
standard	90 – 104	
superlong	88 → 94	

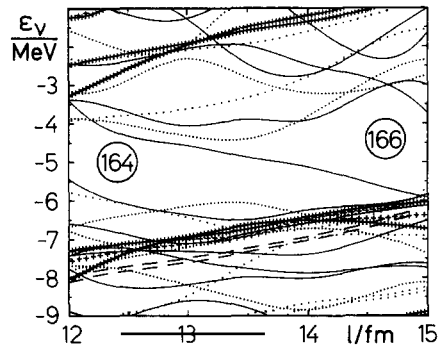

Fig. 9.2. Single-particle energies ε_ν of the neutrons along the supershort channel for ^{258}Fm. The neck radius varies with the semilength as $r/\mathrm{fm} = 1.5 - 0.67(l/\mathrm{fm} - 15)$. The asymmetry is nil. Variant (ii) of section 9.2 was used for the computation. The legend for the various types of lines can be found in fig. 9.4.

special with ^{258}Fm; all nuclei of similar size show almost the same features. You will notice two large gaps, one at moderate deformations with 82 levels below it so that 164 neutrons fit in, the other gap above the 83rd level at larger stretching. According to table 8.5 the supershort channel ruptures at $l \approx 15$ fm. At a semilength of $l \approx 13.5$ fm the liquid-drop energies are so adverse that even a very favorable shell cannot induce scission. 166 is therefore the correct magic neutron number for supershort fission [5.9, 9.15].

Things are slightly more complicated for supershort's magic proton number. When we look at fig. 9.3 we do not find a definite gap, but rather a broad zone of level thinning. Thus 100, 102, 104, 106 and 108, but also the odd intermediate values, appear as valid proton numbers. Therefore it might be appropriate to speak of a *magic range* 100–108, as entered in table 9.1.

Magic ranges can generate an exit channel in a broad spectrum of nuclei. Of course, even if a magic number is sharp, several nuclides can take advantage of its existence, but the supershort channel in a nucleus such as ^{278}[110] (fig. 7.5) is rendered possible only by a magic range.

This holds all the more for the standard channel. The limits within which its magic proton number can range are especially wide, see table 9.1, explaining the universality of the standard channel throughout many preactinides and all the actinides (section 7.3).

The situation is different with the superlong channel. We see in fig. 9.4 a major gap at 94 protons.

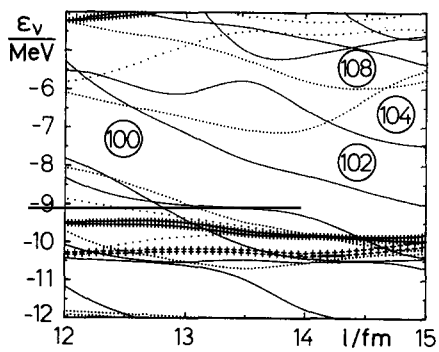

Fig. 9.3. The same as fig. 9.2, but for protons.

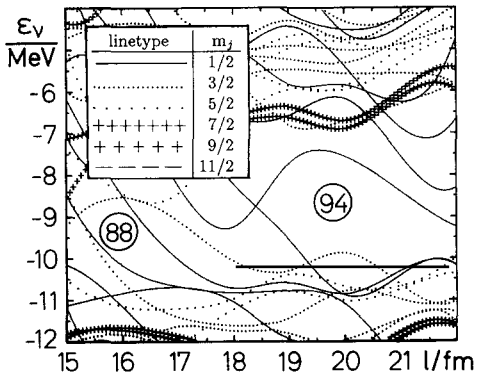

Fig. 9.4. Similar as fig. 9.2 but for protons along the superlong channel. The calculation was made for ^{236}U. The superlong channel was parametrized according to $r/\mathrm{fm} = 0.25\{[(l/\mathrm{fm} - 20)^2 + 0.25]^{1/2} - l/\mathrm{fm}\} + 6.88$. The energies ε_ν are distinguished with respect to the three-projection of the total angular momentum $m_j = m + m_s$, which is conserved in axisymmetrical shapes.

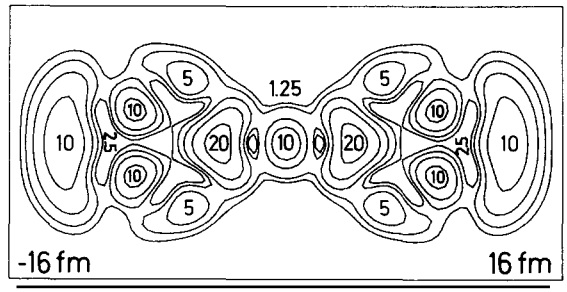

Fig. 9.5. Contour plot of the fifty first single-proton wavefunction. Shown is the squared modulus, and the numbers at the contours give densities times 10^4 fm^3. This is the wavefunction belonging to the energy below 102 in fig. 9.3. Note the concentration of probability in the central part.

From this we conclude that the plutonium isotopes should have the most impressive superlong prescission shapes. This seems to be true, cf. table 8.5. On the other hand, there is a gap below the proton number 88, but this occurs at smaller elongations. Liquid-drop energies are here not adverse to hindering the nucleus from breaking. We have therefore an explanation of why the superlong prescission shape is so much longer for plutonium than for astatine or actinium, cf. table 8.5, and need not resort to the argument that in those lighter nuclei shell effects disappear.

One can associate some magic numbers of the fissioning nucleus with the magic numbers of fragments. The supershort magic number 166 is almost the sum 82 + 82. In addition, the lower limit 90 of the standard channel's magic range can be construed as 40 + 50. A similar interpretation for the superlong channel is impossible as no symmetric decomposition of 88 or 94 exists. Nevertheless, one can say that the magic numbers of fission are sums of the magic numbers of the fragments plus some nucleons for the neck. For the supershort channel this is illustrated in fig. 9.5. However, for the superlong channel the number of nucleons to be added becomes so large that the argument loses credibility.

The idea that clusters are preformed in the fissioning nucleus so that magic fragments are preferentially produced was probably first developed by Wildermuth and coworkers. They reviewed their work in [9.17]. Based on cluster theory, the events, which we now call supershort, were predicted long before measurements were made [9.18]. Computations using the two-center shell model made these ideas more quantitative [9.19–9.21]. The two-center shell model is suited for such investigations as it favors the formation of clusters by its prepared centers. Studies based on Woods–Saxon [9.15, 9.16, 3.15] or Yukawa-folded potentials [9.22] are not preconditioned in this way and yield, therefore, the magic clusters only as an approximation. In this context we want to draw attention to a paper [9.23] that contains several improvements over [9.22], in particular for the shape dependences of the Wigner and A^0 terms and a more appropriate smoothing range.

The papers [9.15], [9.16] as well as [9.24], [3.15] and [5.9] present results that confirm each other. For example, the magic neutron number 166 was obtained in [5.9] and [9.15]. In addition, the standard, supershort and superlong prescission shapes were identified in [5.9] and [9.15], with similar semilengths. The bifurcation points between the standard and the supershort channels, published in [9.16], are situated as shown in fig. 8.1 of this report.

10. Homage

Much in this report is a confrontation with the scission-point model of nuclear fission. The differences can be condensed into two points:

(i) In the scission-point model, the exit channel observables are derived from an *equilibrium* state. Random neck rupture relies on a sequence of *instabilities*.

(ii) In the scission-point model, the shell effects of the, possibly deformed, *fragments* play the dominant role. Multichannel fission is based on the shell effects of the *fissioning nucleus* before decay. Despite these contrasts, a paper by Wilkins, Steinberg and Chasman (WSC) [1.4], which advocates the scission-point ideas, has served us as an example. This work has several attractive features:

WSC theory keeps things as simple as possible and rather goes at things. Its main goal is to order a gigantic body of data. Theoretical subtleties have been put aside.

WSC theory is based on pictures. Such an approach is flexible since advanced formal methods can be incorporated as soon as they become available. All the more important, the basic ideas are spread with much more ease when one can resort to representative pictures. Figures 1 and 2 in [1.4], for example, were the basis for thousands of discussions on nuclear fission.

WSC theory was systematically compared with experiments. The paper [1.4] contains a comprehensive discussion on the prominent trends of yields and total kinetic energies throughout the actinides. In addition, many special experimental findings are discussed to corroborate the theory. This differs much from the numerous models of nuclear reactions that were introduced to fit the needs of one fashionable experiment.

One can discover many analogies in the present work. Figures 3.1 and 7.1 are the basic pictures of random neck rupture and multichannel fission. In ch. 5, the experimental evidence for random neck rupture is compiled, including not only data from fission but also from deep-inelastic reactions. Ch. 7 contains a survey on the evidence for multichannel fission with yields, total kinetic energies and neutron multiplicities. Chapter 8 comprises many additional points that can be adduced for corroboration.

After all, the present work is in many respects a continuation of what was done with the scission-point model. The prescission shape is not entirely different from the scission-point configuration. The former contains the physics shortly before rupture, the latter briefly afterwards. And some of the magic numbers of fission (section 9.4) are nothing more than the sum of the magic numbers of the fragments plus some nucleons for the neck. These relations are the reason for the considerable success of the scission-point model. If one thinks in such terms of continuation, one may say that the present work is just a tracing back of the scission-point configuration into the internals prior to scission.

But this tracing back is not complete. We still make the difference between entrance and exit channels (see the title of this review) and cannot compute from the initial settings all one needs for the exit-channel observables. Specifically, we cannot calculate the channel probabilities p_c, introduced in the eqs. (7.1) to (7.3). Hence *following fission from the onset till the formation of fragments* is the next problem fission research should solve. Some of the first steps in this direction were presented in section 7.5. Theoretically, lifetime calculations as in [10.1, 10.2] will prove to be valuable exercises.

Two fundamental concepts of scission dynamics, which will play a prominent role in future developments, were neglected in this report: inertia (see, however, sections 3.3 and 3.4) and friction (section 3.5). We now want to quote at least some papers that discuss the state of the art for inertia, namely [10.2], and for friction, namely [10.3, 10.4].

Acknowledgements

We received great enthusiasm on the physics of fission from C. Budtz-Jørgensen, F.-J. Hambsch, H.-H. Knitter and J.P. Theobald. Stimulating comments in the same direction were made by R.L. Hahn, E.K. Hulet, M. Schädel, K. Sümmerer and J.F. Wild, as well as remarks by M. Itkis, Yu. Ts. Oganesyan and R. Vandenbosch. We took advantage from the collaboration with A. Deruytter, P. Schillebeeckx and C. Wagemans, P. Glässel and R. Schmid-Fabian, with E. Jacobs and M. Piessens, H.-G. Clerk, U. Kneissl and, of course, with F. Gönnenwein. H. Nakahara supplied us with magnificent experimental material.

On the theoretical side we were supported by W.I. Furman and J. Kliman. A. Sobiczewski had a critical look at part of our work and helped to eliminate a distracting mistake. Discussions with G.D. Adeev and I.I. Gonchar brought valuable insights. We also remember interesting suggestions by M. Pomorski and D.N. Poenaru.

Over ten years we had many interactions with H.J. Krappe, A. Gobbi, J.J. Griffin, W. Nörenberg, R.W. Hasse, M. Brack and M. Asghar, who all advised us well.

We appreciate the generosity of the GSI, Darmstadt, the CBNM, Geel, and W. Westmeier's Gesellschaft für Kernspektrometrie, Mölln.

References

[1.1] G.N. Flerov and S.M. Polikanov, Compt. Rend. Cong. Int. Phys. Nucl. 1 (1964) 407.
[1.2] M. Brack, J. Damgaard, A.S. Jensen, H.C. Pauli, V.M. Strutinsky and C.Y. Wong, Rev. Mod. Phys. 44 (1972) 320.
[1.3] R. Bock, ed., Heavy-Ion Collisions, 2 volumes (North-Holland, Amsterdam, 1980).
[1.4] B.D. Wilkins, E.P. Steinberg and R.R. Chasman, Phys. Rev. C 14 (1976) 1832.
[1.5] S. Grappa, J. Albinski, R. Bock, A. Gobbi, N. Herrmann, K.D. Hildenbrand, J. Kuźminski, W.F.J. Müller, M. Petrovici, H. Stelzer, J. Tōke, H.J. Wollersheim, A. Olmi, P.R. Maurenzig, and A.A. Stefanini, Phys. Rev. Lett. 54 (1985) 1898.
[1.6] S. Bjørnholm and J.E. Lynn, Rev. Mod. Phys. 52 (1980) 725.
[1.7] A. Bohr and B.R. Mottelson, Nuclear Structure, vol. II (Benjamin, Reading, MA, 1975).
[1.8] F.-J. Hambsch, H.-H. Knitter, C. Budtz-Jørgensen and J.P. Theobald, Nucl. Phys. A 491 (1989) 56.
[1.9] A. Turkevich and J.B. Niday, Phys. Rev. 84 (1951) 52.
[1.10] H.C. Britt, H.E. Wegner and J.C. Gursky, Phys. Rev. 129 (1963) 2239.
[1.11] E.K. Hulet, J.F. Wild, R.J. Dougan, R.W. Lougheed, J.H. Landrum, A.D. Dougan, M. Schädel, R.L. Hahn, P.A. Baisden, C.M. Henderson, R.J. Dupzyk, K. Sümmerer and G.R. Bethune, Phys. Rev. Lett. 56 (1986) 313.
[1.12] V.V. Pashkevich, Nucl. Phys. A 169 (1971) 275.
[1.13] S.L. Whetstone, Phys. Rev. 114 (1959) 581.
[1.14] S.A. Karamyan, Yu.Ts. Oganesyan and B.I. Pustylnik, Yad. Fiz. 11 (1969) 982 [Engl. Transl., Sov. J. Nucl. Phys. 11 (1970) 546].
[1.15] J.J. Griffin and K.-K. Kan, Rev. Mod. Phys. 48 (1976) 467.
[1.16] R.Y. Cusson, J.A. Maruhn and H. Stöcker, Z. Phys. A 294 (1980) 257.
[1.17] Proc. Int. Conf. Fifty Years Research in Nuclear Fission (Berlin, 1989) invited papers [Nucl. Phys. A 502 (1989)].
[1.18] Proc. Int. Conf. Fifty Years Research in Nuclear Fission (Berlin, 1989) contributed papers, HMI-B 464 (Hahn-Meitner-Institut, Berlin, 1989).

[2.1] R.W. Hasse, Ann. Phys., N.Y. 68 (1971) 377.
[2.2] V.M. Strutinskiĭ, JETP 42 (1962) 1571 [Engl. Transl., Sov. Phys. – JETP 15 (1962) 1091].
[2.3] J.R. Nix, Nucl. Phys. A 130 (1969) 241.
[2.4] J.N.P. Lawrence, Phys. Rev. 139 (1965) B1227.
[2.5] U. Brosa and E. Becker, Das zufällige Halsreissen/Random neck rupture, movie C1694 (German or English), (IWF, Göttingen, FRG) available on loan.
[2.6] U. Brosa and S. Grossmann, J. Phys. G: Nucl. Phys. 10 (1984) 327.
[2.7] U. Brosa and S. Grossmann, Phys. Lett. 126 B (1983) 425.

[3.1] U. Brosa, Phys. Rev. C 38 (1988) 1944.
[3.2] U. Brosa, Phys. Rev. C 32 (1985) 1438.
[3.3] L. Wilets, Theories of Nuclear Fission (Clarendon, Oxford, 1964).
[3.4] U. Brosa, J. Physique 45 (1984) C6-473.
[3.5] F. Savart, Ann. Chimie 53 (1833) 337.
[3.6] J. Plateau, Statique Expérimentale et Théoretique des Liquides Soumis aux Seules Forces Moléculaires (Gauthier-Villars, Paris, 1873).
[3.7] J.W. Rayleigh, Proc. London Math. Soc. 10 (1878) 4.
[3.8] U. Brosa and S. Grossmann, Phys. Lett. 126 B (1983) 425.
[3.9] V.M. Strutinsky, N.Y. Lyashchenko and N.A. Popov, Nucl. Phys. 46 (1963) 639.
[3.10] R.W. Hasse, R. Ebert and G. Süssmann, Nucl. Phys. A 106 (1968) 117.
[3.11] E. Becker, Fluctuations of asymmetry when a droplet scissions (in German), Diploma Thesis (University of Marburg, FRG, 1988).
[3.12] U. Brosa and S. Grossmann, Z. Phys. A 310 (1983) 177.
[3.13] U. Brosa and S. Grossmann, J. Phys. G Nuc. Phys. 10 (1984) 933.
[3.14] S. Grossmann and U. Brosa, Z. Phys. A 319 (1984) 327.
[3.15] U. Brosa, S. Grossmann and A. Müller, Z. Naturforsch. 41a (1986) 1341.
[3.16] M. Abramowitz and I.A. Stegun (eds), Handbook of Mathematical Functions (Dover Publications, New York, 1965) ch. 9.
[3.17] S. Grossmann and A. Müller, Z. Phys. B 57 (1984) 327.
[3.18] R.W. Hasse, Rep. Prog. Phys. 41 (1978) 1027.
[3.19] A. Müller and S. Grossmann, Z. Naturforsch. 40a (1985) 968.
[3.20] J.P. Blaizot, Phys. Rep. 64 (1980) 171.
[3.21] S. Grossmann and H.J. Krappe, Phys. Rev. C 34 (1986) 914.

[4.1] W.D. Myers and W.J. Swiatecki, Nucl. Phys. 81 (1966) 1.
[4.2] W.D. Myers and W.J. Swiatecki, Ark. Fys. 36 (1967) 343.
[4.3] S. Cohen and W.J. Swiatecki, Ann. Phys. (NY) 19 (1962) 67.
[4.4] Ph. Quentin, J. Physique 30 (1969) 497.
[4.5] J. Błocki, J. Randrup, W.J. Swiatecki and C.F. Tsang, Ann. Phys. (NY) 105 (1977) 427.
[4.6] A.H. Wapstra and G. Audi, Nucl. Phys. A 432 (1985) 1.

[5.1] V.E. Viola, Nucl. Data Tables A1 (1966) 391.
[5.2] V.E. Viola, K. Kwiatkowski and M. Walker, Phys. Rev. C 31 (1985) 1550.
[5.3] L.N. Andronenko, A.A. Kotov, M.M. Nesterov, V.F. Petrov, N.A. Tarasov, L.A. Vaishnene and W. Neubert, Z. Phys. A 318 (1984) 97.
[5.4] G. Andersson, M. Areskough, H.-Å. Gustafsson, G. Hyltén, B. Schrøder and E. Hagebø, Z. Phys. A 293 (1979) 241.
[5.5] F. Plasil, D.S. Burnett, H.C. Britt and S.G. Thompson, Phys. Rev. 142 (1966) 696.
[5.6] H. Rossner, D. Hilscher, D.J. Hinde, B. Gebauer, M. Lehmann, M. Wilpert and E. Mordhorst, Phys. Rev. C 40 (1989) 2629.
[5.7] J.G. Cuninghame, J.A.B. Goodall, J.E. Freeman, G.W.A. Newton, V.J. Robinson, J.L. Durell, G.S. Foote, I.S. Grant and J.D. Hemingway, Proc. IAEA Symp. Physics and Chemistry of Fission, vol. I (Jülich 1979) (IAEA, Vienna, 1980) p. 551.
[5.8] J.P. Unik, J.E. Gindler, L.E. Glendenin, K.F. Flynn, A. Gorski and R.K. Sjoblom, Proc. Third IAEA Symp. Physics and Chemistry of Fission (Rochester 1973), vol II (IAEA, Vienna, 1974) p. 19.
[5.9] U. Brosa, S. Grossmann and A. Müller, Z. Phys. A 325 (1986) 241.
[5.10] W. Bohne, P. Fröbrich, K. Grabisch, K. Hartmann, H. Lehr, H. Morgenstern and W. Stöffler, Z. Phys. A 313 (1983) 19.
[5.11] G. Rudolf, A. Gobbi, H. Stelzer, U. Lynen, A. Olmi, H. Sann, R.G. Stokstad and D. Pelte, Nucl. Phys. A 342 (1979) 243.
[5.12] A. Gobbi, private communication (1983).
[5.13] E.C. Wu, K.D. Hildenbrand, H. Freiesleben, A. Gobbi, A. Olmi, H. Sann and U. Lynen, Phys. Rev. Lett. 47 (1981) 1874.
[5.14] K.D. Hildenbrand, private communication (1981).
[5.15] H.J. Wollersheim, W.W. Wilcke, J.R. Birkelund, J.R. Huizenga, W.U. Schröder, H. Freiesleben and D. Hilscher, Phys. Rev. C 24 (1981) 2114.
[5.16] W.U. Schröder, J.R. Birkelund, J.R. Huizenga, K.L. Wolf and V.E. Viola Jr., Phys. Rep. 45 (1978) 301.
[5.17] W.W. Wilcke, J.R. Birkelund, A.D. Hoover, J.R. Huizenga, W.U. Schröder, V.E. Viola Jr., K.L. Wolf and A. Mignerey, Phys. Rev. C 22 (1980) 128.
[5.18] T. Tanabe, R. Bock, M. Dakowski, A. Gobbi, H. Sann, H. Stelzer, U. Lynen, A. Olmi and D. Pelte, Nucl. Phys. A 330 (1979) 243.
[5.19] H. Freiesleben, K.D. Hildenbrand, F. Pühlhofer, W.F.W. Schneider, R. Bock, D. von Harrach and H.J. Specht, Z. Phys. A 292 (1979) 171.
[5.20] E.N. Gruzintsev, M.G. Itkis, S.I. Mulgin, V.N. Okolovich, A.Ya. Rusanov, O.I. Serdyuk, G.N. Smirenkin and M.I. Subbotin, Yad. Fiz. 48 (1988) 312.
[5.21] P. Dyer, M.P. Webb, R.J. Puigh, R. Vandenbosch, T.D. Thomas and M.S. Zisman, Phys. Rev. C 22 (1980) 1509.
[5.22] A. Gobbi and W. Nörenberg, in Heavy Ion Collisions, vol. II, eds R. Bock (North-Holland, Amsterdam, 1980) p. 127.
[5.23] U. Brosa and S. Grossmann, in: Heavy Ions and Nuclear Structure, Proc. 14th Mikolajki Summer School of Nuclear Physics (Mikolajki, 1981), eds B. Sikora and Z. Wilhelmi (Harwood, New York, 1984), invited talks, p. 121.
[5.24] F. Plasil, R.L. Ferguson and H.W. Schmitt, Proc. IAEA Symp. on Physics and Chemistry of Fission (Vienna, 1969), (Vienna, IAEA, 1969) p. 505.

[5.25] E. Cheifetz, Z. Fraenkel, J. Galin, M. Lefort, J. Péter and X. Tarrago, Phys. Rev. C 2 (1970) 256.
[5.26] Z. Fraenkel, I. Mayk, J.P. Unik, A.J. Gorski and W.D. Loveland, Phys. Rev. C 12 (1975) 1809.
[5.27] E. Konecny and H.W. Schmitt, Phys. Rev. 172 (1968) 1213.
[5.28] D.R. Benton, H. Breuer, F. Khazaie, K. Kwiatkowski, V.E. Viola, S. Bradley, A.C. Mignerey, A.P. Weston-Dowkes and R.J. McDonald, Phys. Lett. 185 B (1987) 326.
[5.29] J. Tōke, W.U. Schröder and J.R. Huizenga, University of Rochester Preprint UR-NSRL-339 (1989).
[5.30] D.J. Hinde, J.R. Leigh, J.J.M. Bokhorst, J.O. Newton, R.L. Walsh and J.W. Boldeman, Nucl. Phys. A 472 (1987) 318.
[5.31] D. Hilscher, J.R. Birkelund, A.D. Hoover, W.U. Schröder, W.W. Wilcke, J.R. Huizenga, A.C. Mignerey, K.L. Wolf, H.F. Breuer and V.E. Viola, Jr, Phys. Rev. C 20 (1979) 576.
[5.32] Gy. Kluge and A. Lajtai, Phys. Lett. 30 B (1969) 311.

[6.1] P. Grangé, H.C. Pauli and H.A. Weidenmüller, Z. Phys. A 296 (1980) 107, see also Phys. Lett. 88 B (1979) 9.
[6.2] C. Grégoire and F. Scheuter, Z. Phys. A 303 (1981) 337.
[6.3] K. Pomorski and H. Hofmann, J. Physique 42 (1981) 381.
[6.4] S.K. Samaddar, D. Sperber, M. Zielinska-Pfabe and M.I. Sobel, Phys. Scr. 25 (1982) 517.
[6.5] F. Scheuter and H. Hofmann, Nucl. Phys. A 394 (1983) 477.
[6.6] G.D. Adeev and I.I. Gonchar, Yad. Fiz. 37 (1983) 1113 [Engl. Transl., Sov. J. Nucl. Phys. 37 (1983) 661].
[6.7] G.D. Adeev and I.I. Gonchar, Yad. Fiz. 40 (1984) 869 [Engl. Transl., Sov. J. Nucl. Phys. 40 (1983) 553].
[6.8] F. Scheuter, C. Grégoire, H. Hofmann and J.R. Nix, Phys. Lett. 149 B (1984) 303.
[6.9] G.D. Adeev and I.I. Gonchar, Z. Phys. 322 (1985) 479.
[6.10] O.I. Serdyuk, G.D. Adeev, I.I. Gonchar, V.V. Pashkevich and N.I. Pischasov, Yad. Fiz. 46 (1987) 710.
[6.11] S. Grossmann, U. Brosa and A. Müller, Nucl. Phys. A 481 (1988) 340.
[6.12] G.D. Adeev and I.I. Gonchar, Z. Phys. A 320 (1985) 451.
[6.13] U. Brosa and H.-H. Knitter, Proc. of the XVIIIth Int. Symp. on Nuclear Physics – Physics and Chemistry of Fission, eds H. Märten and D. Seeliger (Nova Science Publishers, New York, 1990) to appear.
[6.14] C. Budtz-Jørgensen and H.-H. Knitter, Nucl. Phys. A 490 (1988) 307.
[6.15] N. Nifenecker, G. Mariolopoulos, J.P. Bocquet, R. Brissot, Ch. Hamelin, J. Crançon and Ch. Ristori, Z. Phys. A 308 (1982) 39.
[6.16] F.J. Gönnenwein, Radiation Effects 94 (1986) 205.
[6.17] R. Becker, Theorie der Wärme (Springer, Berlin, 1961).
[6.18] R.L. Stratonovich, Topics in the Theory of Random Noise I (Gordon and Breach, New York, 1963).
[6.19] H. Risken, The Fokker–Planck equation (Springer, Berlin, 1984).
[6.20] S. Grossmann, Z. Naturforsch. 34a (1979) 1275; Z. Phys. A 296 (1980) 251.
[6.21] S. Grossmann and H.J. Krappe, Z. Phys. A 298 (1980) 41.
[6.22] J. Tōke, R. Bock, G.X. Dai, S. Grappa, A. Gobbi, K.D. Hildenbrand, J. Kuzminski, W.F.J. Müller, A. Olmi and H. Stelzer, Nucl. Phys. A 424 (1984) 157.
[6.23] A. Gobbi, private communication (1985).
[6.24] M. Petrovici, J. Albinski, R. Bock, R. Cusson, A. Gobbi, G. Guarino, S. Grappa, K.D. Hildenbrand, W.F.J. Müller, A. Olmi, H. Stelzer and J. Tōke, Nucl. Phys. A 477 (1988) 277.

[7.1] U. Brosa, S. Grossmann and A. Müller, Proc. XVIth Int. Symp. on Nucl. Phys. (Gaussig, GDR, 1986), eds R. Reif and R. Schmidt (Akademie der Wissenschaften der DDR, Rossendorf, 1986), p. 162.
[7.2] U. Brosa, S. Grossmann and A. Müller, GSI Nachrichten 8 (1987) 13.
[7.3] Ye.N. Gruzintsev, M.G. Itkis, V.N. Okolovich, A.Ya. Rusanov, V.N. Tolstikov and G.N. Smirenkin, Phys. Lett. 126 B (1983) 428.
[7.4] M.G. Itkis, V.N. Okolovich, A.Ya. Rusanov and G.N. Smirenkin, Fiz. Elem. Čast. i Atom. Yad. 19 (1988) 701.
[7.5] M.G. Itkis, V.N. Okolovich, A.Ya. Rusanov and G.N. Smirenkin, Z. Phys. A 320 (1985) 433.
[7.6] M. Piessens, E. Jacobs, D. De Frenne, S. Pommé and A. De Clercq, Mass and kinetic energy distributions for ^{232}Th(γ, f), 50 Years with Nuclear Fission (Gaithersburg, Maryland, 1989).
[7.7] C. Wagemans, Contemporary fission, Proc. 5th Int. Symp. on Nucleon Induced Reactions (Smolenice, Czechoslovakia, 1988).
[7.8] C. Wagemans, P. Schillebeeckx and A. Deruytter, Int. Conf. on Fifty Years Research in Nuclear Fission (Berlin, 1989) contributed papers (HMI, Berlin, 1989) HMI-B 464, p. 4.
[7.9] E.K. Hulet, J.F. Wild, R.J. Dougan, R.W. Lougheed, J.H. Landrum, A.D. Dougan, P.A. Baisden, C.M. Henderson, R.J. Dupzyk, R.L. Hahn, M. Schädel, K. Sümmerer and G.R. Bethune, Phys. Rev. C 40 (1989) 770.
[7.10] D. Hoffman, Proc. Int. Symp. Physics and Chemistry of Fission (Jülich, 1979), vol. II (IAEA, Vienna, 1980) p. 275.
[7.11] H.-H. Knitter, F.-J. Hambsch, C. Budtz-Jørgensen and J.P. Theobald, Z. Naturforsch. 42a (1987) 786.
[7.12] V.F. Apalin, Yu.N. Gritsyuk, I.E. Kutikov, V.I. Lebedev and L.A. Mikaelian, Nucl. Phys. 71 (1965) 553.
[7.13] J.F. Wild, J. van Aarle, W. Westmeier, R.W. Lougheed, E.K. Hulet, K.J. Moody, R.J. Dougan, E.-A. Koop, R.E. Glaser, R. Brandt and P. Patzelt, Phys. Rev. C 41 (1991) 640.
[7.14] K.F. Flynn, E.P. Horwitz, C.A. Bloomquist, R.F. Barnes, R.K. Sjoblom, P.R. Fields and L.E. Glendenin, Phys. Rev. C 5 (1972) 1725.
[7.15] A. Müller, S. Grossmann and U. Brosa, Mean values of the total kinetic energy and the fragment masses in the channel picture, GSI Scientific Report 1988 (GSI, Darmstadt, 1989), p. 92.

[7.16] P. Gippner, K.D. Schilling, W. Seidel, F. Stary, E. Will, H. Sodan, S.M. Lukyanov, V.S. Salamatin, Yu.E. Penionzhkevich, G.G. Chubarian and R. Schmidt, Z. Phys. A 325 (1986) 325.
[7.17] W. Stocker, Lett. Nuovo Cimento 12 (1975) 459.
[7.18] L.J. Colby Jr, M.L. Shoaf and J.W. Cobble, Phys. Rev. 121 (1961) 1415.
[7.19] W.I. Furman and J. Kliman, Proc. XVIIth Int. Symp. on Nucl. Phys. (Gaussig, GDR, 1987), ed. D. Seelinger (Akademie der Wissenschaften der DDR, Rossendorf, 1986), p. 86.
[7.20] J. Kliman, Study of the gamma yield from the single fragments in the fission of ^{235}U by resonance neutrons (in Russian), PhD Thesis (JINR, Dubna, USSR, 1988).
[7.21] A. Bohr, Proc. Int. Conf. on Peaceful Uses of Atomic Energy (Geneva, 1955) vol. II (United Nations, New York, 1956) p. 151.
[7.22] R. Vandenbosch and J.R. Huizenga, Nuclear Fission (Academic Press, New York, 1973).
[7.23] N.J. Pattenden and H. Postma, Nucl. Phys. A 167 (1971) 225.
[7.24] M.S. Moore, J.D. Moses, G.A. Keyworth, J.W.T. Dabbs and N.W. Hill, Phys. Rev. C 18 (1978) 1328.
[7.25] M.S. Moore, G. de Saussure and J.R. Smith, Proc. IAEA Consult. Meeting (Vienna, 1981) (INDC(NDS)-129/GJ) p. 74.
[7.26] S.G. Kadmensky, V.P. Markushev and W.I. Furman, Yad. Fiz. 35 (1982) 300.
[7.27] M.S. Moore, L.C. Leal, G. de Saussure, R.B. Perez and N.M. Larson, Nucl. Phys. A 502 (1989) 443c.
[7.28] W. Wilke, R.D. Heil, U. Kneissl, U. Seemann, F. Steiper, H. Ströher and T. Weber, Phys. Lett. B 207 (1988) 385.
[7.29] Th. Weber, R.D. Heil, U. Kneissl, W. Wilke, H.J. Emrich, Th. Kihm and K.T. Knöpfle, Phys. Rev. Lett. 62 (1989) 129.

[8.1] P.G. Mezey, Potential Energy Hypersurfaces (Elsevier, Amsterdam, 1987), ch. VI.
[8.2] R.R. Chasman, Phys. Lett. 69 B (1980) 7.
[8.3] G.A. Leander, R.M. Sheline, P. Möller, P. Olanders, I. Ragnarsson and A.J. Sierk, Nucl. Phys. A 388 (1982) 452.
[8.4] R.R. Chasman, Phys. Lett. 175 B (1986) 254.
[8.5] P. Möller and J.R. Nix, Nucl. Phys. A 361 (1981) 1217.
[8.6] P. Möller and J.R. Nix, At. Data Nucl. Data Tables 26 (1981) 165.
[8.7] M. Dahlinger, D. Vermeulen and K.-H. Schmidt, Nucl. Phys. A 376 (1982) 94.
[8.8] M.G. Itkis, Yu.V. Kotlov, S.I. Mulgin, V.N. Okolovich, A.Ya. Rusanov and G.N. Smirenkin, Yad. Fiz. 46 (1987) 1380.
[8.9] E. Konecny, H.J. Specht and J. Weber, Proc. Third IAEA Symp. Physics and Chemistry of Fission (Rochester, 1973) vol. II (Vienna, IAEA, 1974) p. 3.
[8.10] M. Piessens, Mass and kinetic-energy distributions of the fragments from photofission of ^{232}Th with 7–14 MeV X-rays (in Dutch), PhD Thesis (University of Gent, Belgium 1989).
[8.11] H. Nakahara, T. Ohtsuki, Z. Hamajima and K. Sueki, Radiochimica Acta 43 (1988) 77 and H. Nakahara, pivate communication.
[8.12] Ch. Straede, C. Budtz-Jørgensen and H.-H. Knitter, Nucl. Phys. A 462 (1987) 85.
[8.13] P. Schillebeeckx, Study of the fission process by the fragments for ^{238,240,242}Pu(s.f.) and ^{239,241}Pu(n_{th}, f) (in Dutch), PhD Thesis (University of Gent, Belgium, 1989).
[8.14] E.K. Hulet, J.F. Wild, R.J. Dougan, R.W. Lougheed, J.H. Landrum, A.D. Dougan, P.A. Baisden, C.M. Henderson, F.J. Dupzyk, M. Schädel, K. Sümmerer, R.L. Hahn and B. Bethune, GSI Scientific Report 1985 (GSI, Darmstadt, 1986), p. 32.
[8.15] Yu.A. Lazarev, Atomic Energy Review 15 (1977) 75.
[8.16] Yu.A. Lazarev, Proc. EPS Topical Conf. on Large Amplitude Collective Nuclear Motions (Keszthely, Hungary, 1979) vol. 1, p. 244.
[8.17] J.L. Cook, E.K. Rose and G.D. Trimble, Austral. J. Phys. 29 (1976) 125.
[8.18] P. Möller and J.R. Nix, Proc. Third IAEA Symp. Physics and Chemistry of Fission (Rochester, 1973) vol. I (IAEA, Vienna, 1974) p. 103.
[8.19] F.J. Gönnenwein, private communication.
[8.20] C. Signarbieux, M. Montoya, M. Ribrag, C. Mazur, C. Guet, P. Perrin and M.J. Mauel, J. Physique 42 (1981) L437.
[8.21] H.-G. Clerc, W. Lang, M. Mutterer, C. Schmitt, J.P. Theobald, U. Quade, K. Rudolph, P. Armbruster, F. Gönnenwein, H. Schrader and D. Engelhardt, Nucl. Phys. A 452 (1986) 277.
[8.22] M. Asghar, F. Caïtucoli, P. Perrin, G. Barreau, C.R. Guet, B. Leroux and C. Signarbieux, Proc. Int. Symp. Physics and Chemistry of Fission (Jülich, 1979) vol. II (IAEA, Vienna, 1980) p. 81.
[8.23] D.N. Poenaru, M.S. Ivaşcu and W. Greiner, in Particle Emission from Nuclei, vol. III, eds D.N. Poenaru and M.S. Ivaşcu (CRC Press, Boca Raton, 1989) p. 203.
[8.24] G. Barreau, W. Sicre, F. Caïtucoli, M. Asghar, T.P. Doan, B. Leroux, G. Martinez and T. Benfougal, Nucl. Phys. A 432 (1985) 411.
[8.25] R.H. Iyer, V.K. Bhargava, V.K. Rao, S.G. Marathe and S.M. Sahakundu, Proc. IAEA Symp. Physics and Chemistry of Fission, vol. II (Jülich, 1979) (IAEA, Vienna, 1980) p. 311.
[8.26] M. Asghar, private communication.
[8.27] R. Schmid-Fabian, P. Glässel, D. Habs, H.U. von Helmholt and D. Schwalm, Insights in ^{252}Cf spontaneous fission, GSI Scientific Report 1987 (GSI, Darmstadt, 1988), p. 20.
[8.28] R. Schmid-Fabian, Measurement of spontaneous fission of ^{252}Cf using the Darmstadt–Heidelberg crystal-ball spectrometer (in German), PhD Thesis, (University of Heidelberg, FRG, 1988).
[8.29] P. Glässel, R. Schmid-Fabian, D. Schwalm, D. Habs and H.U. von Helmolt, Nucl. Phys. A 502 (1989) 315c.

[9.1] M.A. Preston and R.K. Bhaduri, Structure of the Nucleus (Addison-Wesley, Reading, 1975).

[9.2] W.D. Myers and W.J. Swiatecki, Nucl. Phys. 81 (1966) 1.
[9.3] W.D. Myers and W.J. Swiatecki, Ark. Fys. 36 (1967) 343.
[9.4] H.J. Krappe and J.R. Nix, Proc. Third IAEA Symp. Physics and Chemistry of Fission (Rochester, 1973) vol. I (IAEA, Vienna, 1974) p. 159.
[9.5] K.T.R. Davies and A.J. Sierk, J. Comp. Phys. 18 (1975) 311.
[9.6] W.H. Press, B.P. Flannery, S.A. Teukolsky and W.T. Vetterling, Numerical Recipes (Cambridge University Press, Cambridge, 1988).
[9.7] M. Brack, C. Guet and H.-B. Håkansson, Phys. Rep. 123 (1985) 275.
[9.8] J.F. Berger, M. Girod and D. Gogny, Nucl. Phys. A 428 (1984) 23c.
[9.9] J. Treiner, R.W. Hasse and P. Schuck, J. Physique Lett. 44 (1985) L733.
[9.10] V.A. Chepurnov, Yad. Fiz. 6 (1967) 955.
[9.11] A. Sobiczewski, T. Krogulski, J. Błocki and Z. Szymanski, Nucl. Phys. A 168 (1971) 519.
[9.12] J. Damgaard, H.C. Pauli, V.V. Pashkevich and V.M. Strutinsky, Nucl. Phys. A 135 (1969) 432.
[9.13] T. Ledergerber and H.C. Pauli, Nucl. Phys. A 207 (1973) 1.
[9.14] A. Müller, Studies on the fission of some transeinsteinium isotopes and of ^{236}U (in German), PhD Thesis (University of Marburg, FRG, 1987).
[9.15] V.V. Pashkevich, Nucl. Phys. A 477 (1988) 1.
[9.16] S. Ćwiok, P. Rozmej, A. Sobiczewski and Z. Patyk, Nucl. Phys. A 491 (1989) 281.
[9.17] F. Gönnenwein, H. Schultheis, R. Schultheis and K. Wildermuth, Z. Phys. A 278 (1976) 15.
[9.18] H. Faissner and K. Wildermuth, Nucl. Phys. 58 (1964) 177.
[9.19] U. Mosel and H.W. Schmitt, Phys. Rev. C 4 (1971) 2185.
[9.20] M.G. Mustafa, Phys. Rev. C 11 (1975) 1059.
[9.21] H.J. Lustig, J.A. Maruhn and W. Greiner, J. Phys. G: Nucl. Phys. 6 (1980) L25.
[9.22] P. Möller, J.R. Nix and W.J. Swiatecki, Nucl. Phys. A 469 (1987) 1.
[9.23] P. Möller, J.R. Nix and W.J. Swiatecki, Nucl. Phys. A 492 (1989) 349.
[9.24] A. Müller, S. Grossmann and U. Brosa, GSI Scientific Report 1985 (GSI, Darmstadt, 1986) p. 153.

[10.1] K. Böning, Z. Patyk, A. Sobiczewski, S. Ćwiok, Z. Phys. A 325 (1986) 479.
[10.2] A. Staszczack, S. Pilat and K. Pomorski, Nucl. Phys. A 504 (1989) 589.
[10.3] G.D. Adeev and V.V. Pashkevich, Nucl. Phys. A 502 (1989) 405c.
[10.4] H.J. Krappe, Friction in heavy-ion collisions, Proc. Int. School–Seminar on Heavy Ion Physics (Dubna, 1989), (JINR, Dubna, 1989).